Titre: Title:	Dual Gate Black Phosphorous Photodetectors Using a Polymer Electrolyte for Integrated Photonics and Optoelectronics Applications
Auteur: Author:	Mohammed Zia Ullah Khan Mohammed Zia Ullah Khan
Date:	2019
Type:	Mémoire ou thèse / Dissertation or Thesis
Référence: Citation:	Mohammed Zia Ullah Khan, M. Z. U. K. (2019). Dual Gate Black Phosphorous Photodetectors Using a Polymer Electrolyte for Integrated Photonics and Optoelectronics Applications [Mémoire de maîtrise, Polytechnique Montréal]. PolyPublie. https://publications.polymtl.ca/4191/

POLYTECHNIQUE MONTRÉAL

affiliée à l'Université de Montréal

Dual gate black phosphorous photodetectors using a polymer electrolyte for integrated photonics and optoelectronics applications

MOHAMMED ZIA ULLAH KHAN MOHAMMED ZIA ULLAH KHAN

Département de génie physique

Mémoire présenté en vue de l'obtention du diplôme de *Maîtrise ès sciences appliquées*

Génie physique

Décembre 2019

POLYTECHNIQUE MONTRÉAL

affiliée à l'Université de Montréal

Ce mémoire intitulé :

Dual gate black phosphorous photodetectors using a polymer electrolyte for integrated photonics and optoelectronics applications

présenté par **Mohammed Zia Ullah Khan MOHAMMED ZIA ULLAH KHAN**

en vue de l'obtention du diplôme de *Maîtrise ès sciences appliquées*

a été dûment accepté par le jury d'examen constitué de :

Sébastien FRANCOEUR, président
Stéphane KÉNA-COHEN, membre et directeur de recherche
Fabio CICOIRA, membre

DEDICATION

I dedicate this thesis to my beloved parents ***Mr. and Mrs. Mohammed Nusrath Ullah Khan****, my sister Sana Khanam, my brothers: Mohammed Aijaz Ullah Khan, Mohammed Immad Ullah Khan, Mohammed Sohaib Ullah Khan and last but not the least my adorable and beautiful nieces Sheza Khanam and Zaira Makhdoom. I am very glad as they have always been my inspiration to pursue higher studies.*

ACKNOWLEDGEMENTS

All praises glory and gratitude is to the Almighty Allah, the most Merciful and the most Beneficent.

I sincerely thank my research director Prof. Stéphane Kéna-Cohen for his immense guidance and encouragement during my study at Polytechnique Montreal. I am truly grateful for all his support throughout my thesis with his patience and knowledge. I am also thankful to him for all the valuable things that I have learned working with him and his group.

I would like to thank my thesis committee members Prof. Sébastien Francoeur and Prof. Fabio Cicoira for investing their precious time to serve as my thesis committee.

I thank the researcher Marie-Hélène Bernier, the department technicians Christophe Clément, Yves Drolet and Jean-Paul Lévesque for providing trainings on various lab equipment required for my fabrication and characterization experiments. I also thank Prof. Thomas Szkopek for their photomask that was used for photolithography experiments. I would also like to acknowledge CMC Microsystems for the MNT financial assistance.

I would also like to thank the postdoctoral fellows: Elad Eizner, Afshin Shahalizad, David Myers, Jian Mao, Junjia Wang, Mahmoud Atalla, Leonard Schue and my fellow graduate and undergraduate students: Fabio Barachati, Soroush Hafezian, Aravindhan Sridharan, Julien Brodeur, Ashutosh Patri, Louis Haeberle, Alex Malinge, Adrien Rousseau, Orlando Ortiz, Mei Yang, Pierre-Luc Theriault, Greogory Laflamme and Fabrice Simo Defo.

I am also grateful to all my friends and colleagues at Polytechnique Montreal. I also thank the Engineering Physics department for providing the world class infrastructure and facilities for performing this research work.

Finally, I owe my deepest gratitude to my parents for their immense love, support, encouragement and supplications, without which this thesis would not have been possible.

RÉSUMÉ

Les photodétecteurs occupent une place prépondérante dans un nombre important de dispositifs. Ceux-ci sont utilisés dans plusieurs pour les communications optiques, la détection d'images, la vision nocturne, l'inspection alimentaire, l'imagerie médicale, etc. La conception de détecteurs infrarouges requiert l'utilisation de matériaux autre que le silicium démontrant une haute efficacité, détectivité et un temps de réponse rapide. Ceux-ci sont typiquement couteux et difficiles à intégrés avec des substrats flexibles ou des circuits photoniques et optoélectroniques conventionnels.

Dans cette thèse, nous présentons un photodétecteur à base de phosphore noir avec une architecture à double grille basé sur sur un électrolyte polymère solide pour des applications en photonique intégrée et en optoélectronique. La combinaison de la grille électrolytique et du photodétecteur BP conventionnel permet un contrôle efficace du transport électrique et de la modulation de la densité de porteurs dans le canal BP. Les détecteurs à double grille fabriqués avec cette approche améliorent le rapport ON / OFF de 50 fois par rapport à l'architecture conventionnelle. Ceux-ci présentent également du courant de drain avec la configuration de contact source-drain orthogonale. Finalement, l'électrolyte polymère protège les flocons de BP de l'oxydation de surface et présentent des caractéristiques électriques stables dans les conditions ambiantes. Nous obtenons une modulation du photocourant par un facteur de 4 pour des puissances incidentes variant de 0.5 mW à 5 mW. Dans cette gamme de puissance, une modulation du photocourant par un facteur de 2 est obtenu en variant la tension de grille supérieure (variée de 3V à -3V) à une longueur d'onde de 808 nm. À plus faible puissance, le photodétecteur donne une modulation de photocourant largement supérieure à l'architecture conventionnelle: environ 16 fois avec une tension de grille d'électrolyte ajustée de -2 V à 2 V par rapport au dispositif à grille inférieure qui est d'environ 2.5 fois avec une tension de grille variant de -10 V 10 V dans le proche infrarouge. Des sensibilités de centaines de mA / W sont obtenues pour les photodétecteurs BP dans les régimes visible et proche-infrarouge.

ABSTRACT

Visible and infrared photodetectors have become important in a multitude of present-day devices that find emerging applications in several fields: optical communications, image sensing, night vision, food monitoring and medical imaging etc. However, photodetection beyond the visible region of spectrum requires investigating unconventional materials and designs that deliver superior performance in terms of photocurrent/responsivity, detectivity and response speed, that also allow ultra-low weight, low-cost, flexible and easy integration with the photonic and optoelectronic circuits.

In this thesis, we report on a dual-gate black phosphorous photodetector based on solid polymer electrolyte for integrated photonics and optoelectronic applications. The combination of polymer electrolyte gate with the conventional back-gate black phosphorous (BP) photodetector allows for efficient control of electrical transport and carrier-density modulation in the BP channel. Our dual-gate field effect transistors provide a 50-fold enhancement in the drain currents that lead to high ON/OFF ratio as compared to the conventional SiO_2 bottom gating. The BP FETs with polymer electrolyte film also protect BP flake from surface oxidation and show stable electrical characteristics under ambient conditions. The polymer electrolyte-based FETs also show an enhancement in the drain current with the orthogonal source-drain contact configuration. Photocurrent modulation by a factor of four by incident powers (varied from 0.5 to 5 mW) at a wavelength of 808 nm. At these modest powers, a factor of two modulation in the photocurrent is achieved by varying the top-gate voltage (from 3 V to -3 V). At lower powers, the dual-gate polymer electrolyte based BP photodetector shows a photocurrent a substantial enhancement of the photocurrent by ~16 when the electrolyte gate voltage tuned from -2 V to 2 V as compared to the bottom gate device which is ~2.5 times, when the gate voltage varied from -10 V to 10 V. Responsivities of the order of hundreds of mA/W are obtained for the BP photodetectors in both visible and NIR regimes.

TABLE OF CONTENTS

LIST OF TABLES

LIST OF FIGURES

LIST OF SYMBOLS AND ABBREVIATIONS

2D	Two Dimensional
AC	Armchair
BP	Black Phosphorous
CB	Conduction Band
CVD	Chemical Vapor Deposition
EBL	Electron Beam Lithography
FET	Field Effect Transistor
FTIR	Fourier Transform Infrared Spectroscopy
HBN	Hexagonal Boron Nitride
LED	Light emitting diode
LWIR	Long-wave Infrared
MWIR	Medium-wave Infrared
NIR	Near Infrared
SWIR	Short-wave Infrared
THZ	Terahertz
TMDCs	Transition metal dichalcogenides
UV	Ultraviolet
VB	Valence Band
ZZ	Zigzag

LIST OF APPENDICES

CHAPTER 1 INTRODUCTION

Broadband detectors for electromagnetic radiation have gained a great deal of attention for applications in optical communications, medical imaging, environmental monitoring, automotive industry and military surveillance [1]–[3]. Considerable research efforts have been made to determine the ideal materials for broadband photodetection in the visible, near-infrared (NIR) and mid-infrared (MIR) wavelengths. Commercial Si detectors are limited to applications at visible wavelengths because of their NIR bandgap. They are also incompatible for emerging applications in flexible and transparent electronics owing to their bulky and brittle properties [4]. Infrared photodetectors IRPDs (1-30 um) are classified into two categories: majority and minority carrier devices. Devices are classified as majority carrier-based if the photon generation rate per unit area is greater than the thermal generation rate per unit area and vice versa for minority carrier devices [5]. Minority carrier-based material systems include direct bandgap semiconductors such as binary (e.g. InSb and InAs), ternary (e.g. HgCdTe and InGaAs) alloys and type II, III superlattices (e.g. InAs/GaInSb, HgTe/CdTe). In contrast to this type of devices, the second type based on majority carrier use Type I superlattices (e.g. GaAs/AlGaAs quantum well IRPDs) and high temperature superconductors [2]. These materials can be fabricated by molecular beam epitaxy (MBE), liquid phase epitaxy (LPE) and chemical vapor deposition (CVD). However, their major limitations include extremely high dark currents, operation at liquid nitrogen temperatures, high manufacturing costs, unsuitability for integration into compact and flexible substrates and low detectivities at room temperatures. Therefore, there remains an important need high-performance optoelectronic materials and devices suitable for infrared photodetection.

Two dimensional materials (2D) have attracted considerable attention in optoelectronics for photodetection applications owing to their outstanding electrical, optical and mechanical properties and are becoming the promising candidates for the next generation photodetection technology. Intensive research efforts are being made to utilize the unique properties of 2D materials to realize and implement devices which are high performance and cost effective over the traditional semiconductors. These materials have also attracted tremendous attention since the devices made from these atomically thin 2D materials can be easily fabricated on photonic structures and thus pave the way for easy integration with silicon photonics. Graphene has been proposed both

theoretically and experimentally to be a good candidate for ultra broadband photodetection because of its wide absorption spectrum from ultraviolet (UV) to far infra-red (FIR) and zero bandgap nature [6]. The major limitation with graphene is its low optical absorption (~2.3%) and ultrashort lifetime of photogenerated carriers that results in low responsivities of the order of tens of mAW^{-1} [6], [7]. Graphene-metal junctions or graphene p-n junctions are commonly used for separating charge carriers and to extract photocurrent, however they are still limited to low responsivities stemming from the small active area of the junction that contributes photocurrent.

A plethora of other 2D materials such as transition metal dichalcogenides (TMDCs) , hexagonal boron nitride (hBN) and black phosphorous (BP) are emerging as excellent candidates for photodetection for a wide wavelength range as shown in Figure 1.1. Compared to graphene, they have distinct electronic and optical properties. For instance, a typical 2D material such as Molybdenum disulphide (MoS_2) possess direct bandgap for monolayer and it also varies from 1.2 eV to 1.9 eV with thickness and has higher absorption coefficients in contrast to graphene. High photo responsivities up to 880 A/W at 561 nm have been demonstrated with monolayer intrinsic MoS_2 that was used a semiconducting material of the phototransistor channel [8]. The high photoresponsivity as compared to the previously reported MoS_2 photodetectors was attributed to its high photoconductive gain, improved mobility, quality of electrical contacts and improved surface treatments. MoS_2 photodetectors have also been combined with other 2D materials to realize high performance devices beyond visible wavelengths. However, the high operating gate voltage and low photoresponse at higher wavelengths limits the applications of MoS_2 photodetectors.

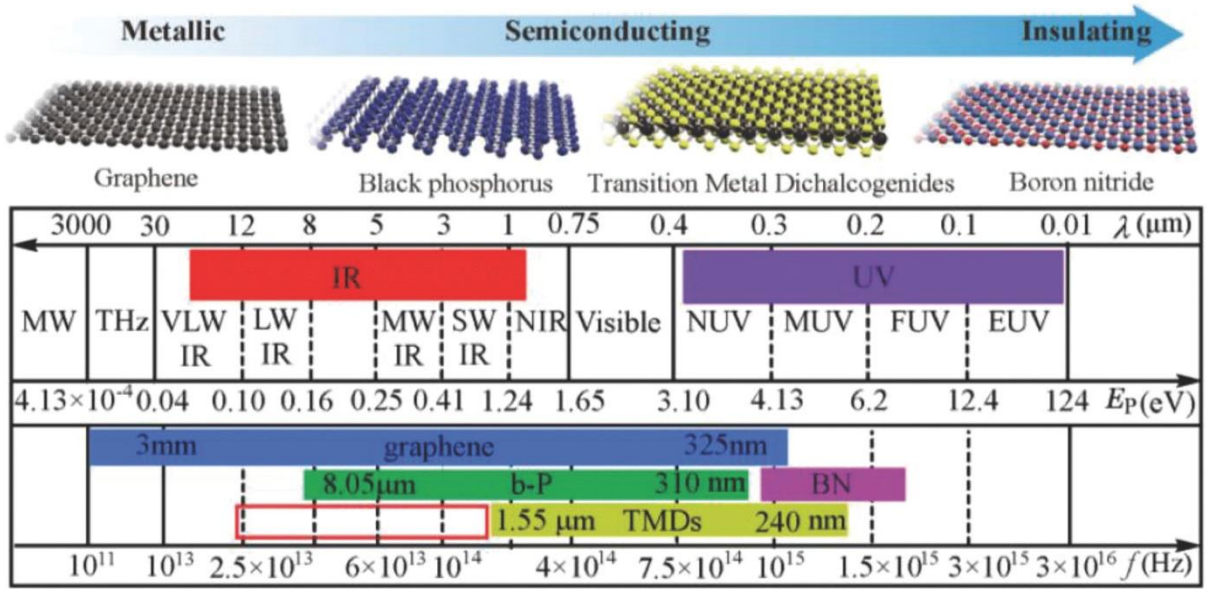

Figure 1.1 Electromagnetic spectrum showing the 2D material bandgaps over a broad range (Reprinted with permission from [9]. Copyright © 2018, John Wiley and Sons).

Recently, BP has emerged as a 2D material with remarkable electronic, optical and mechanical properties and has been tremendously used to realize NIR and MIR photodetectors. It has gained a lot of attention because of its thickness dependent direct bandgap that varies from 0.39 eV (bulk) to 2 eV (monolayer) [10], anisotropic electronic and optical properties [11], semiconductor to metal phase transitions and superconductor at high pressure [12]. In addition to the thickness, the bandgap can also be varied by applying electric field, chemical doping, strain, electrostatic gating and composition alloying [13]–[17]. The direct bandgap of 0.39 eV for bulk BP can be observed form the band diagram shown in Figure 1.2. The anisotropic electronic behaviour arises due to the asymmetric shape of the band dispersion around the Γ point [18].

These unique properties of BP resulting from its crystal structure shown in Figure 1.3 are also highlighted. The structure is composed of phosphorous atoms connected to three neighbouring atoms that result in two major orientations namely armchair (AC) and zigzag (ZZ) along x and y axis respectively. Such ordering leads to anisotropic optoelectronic properties in this material. These highly anisotropic electronic [19], optical [20], thermal [21], [22] and mechanical properties [23] along the AC and ZZ directions of BP shown in Figure 1.3 have been demonstrated in several studies. The observed spatially anisotropic electrical and thermal conductance in monolayer BP

show that the preferred electric and thermal conductance are orthogonal to each other [19]. Such anisotropy in electrical and thermal conductance significantly improves the thermoelectric performance of this material. Additionally, BP also exhibit unique excitonic effects that has not been seen in other 2D materials. The optical absorption spectra of few layer BP for the light incident along AC direction have shows enhanced excitonic effects. For instance, for the monolayer BP strongly bound excitonic state with an 800 meV e-h binding energy was observed with the first absorption peak located at 1.2 eV. On the other hand, the optical absorption spectrum is unaffected by the incorporation of e-h interactions. The anisotropic optical absorption in few layer BP have also shown that it is prominent for AC polarized light for energies between 1.1 eV and 2.8 eV, and is transparent to ZZ polarized light [20]. The anisotropy in mechanical properties along AC and ZZ directions is related to the existence of negative Poisson's ratio and has been attributed to the puckered atomic structure of few layer BP [23]. The electronic band structure of multilayer BP (MBP) have also been shown to tuned with the applied strain. The analytical studies based on the first-principle calculations for the electronic and structural response of MBP to in-layer strain have also demonstrated an intense anisotropy in the Poisson's ratio and strain energy with respect to uniaxial strain direction [24].

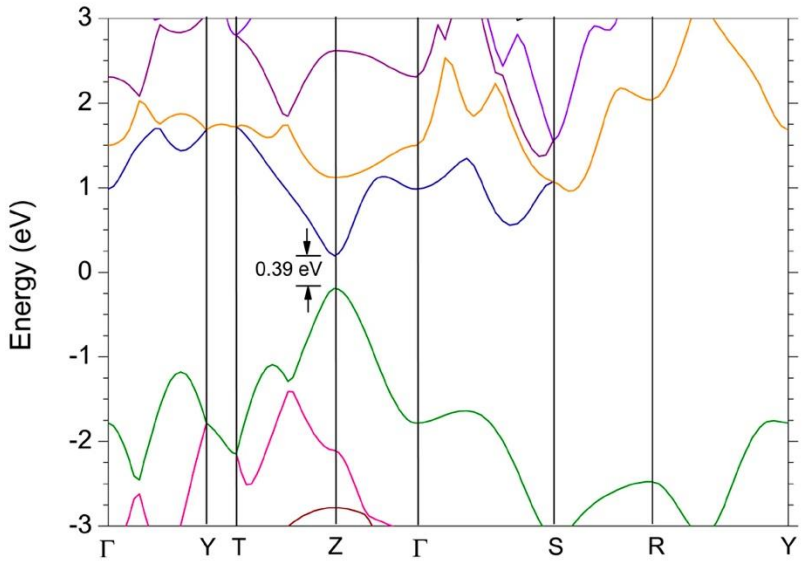

Figure 1.2 : Band diagram of the bulk BP (Reprinted with permission from [18]. Copyright © 2014, Springer Nature).

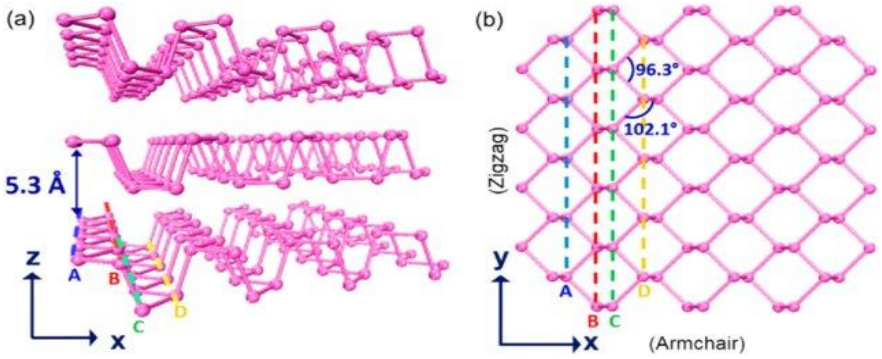

Figure 1.3 : a) Atomic crystal structure of BP a) side view (spacing between monolayers is 5.3 $\dot{A}$) b) top view where x and y correspond to AC and ZZ directions respectively (Reprinted with permission from [25]. Copyright © 2018, IOP Publishing, Ltd).

The BP flakes rapidly lose their electrical and optical properties in few days due to ambient degradation [26]–[28]. Several strategies have been used to enhance BP stability by encapsulating with HBN, graphene, MoS_2, Aluminium oxide (Al_2O_3), Titatanium oxides (TiO_x), surface modifications and doping with specific elements [29]. There is still need for the effective design strategies that can improve the device performance in terms of responsivity, response speed, sensitivity and noise parameters.

A dual-gate field effect transistor (FET) configuration can effectively control the trap carrier densities and also allows to efficiently separate photogenerated electrons and holes in BP layer. Such top gating helps to facilitate charge control in BP and can provide high photoconductive gain and reduce the dark current. The gate bias can be used to tune the transport properties of the channel. Combining polymer electrolyte gating with the BP dual-gate FET configuration can help to obtain low operating voltage and dark currents to improve photoresponsivity for the entire visible and infrared range which will be addressed in this thesis. The work done on 2D material based visible photodetectors with polymer gating are reviewed below to understand their advantages.

Visible photodetectors based on electrolyte gating have demonstrated higher photoresponsivity than that of conventional Si bottom gate photodetectors [30]. Photodetection with such technique was realized using monolayer tungsten diselenide (WSe_2) electric double layer transistor (EDLT)

based p-n photodiode and ion gel electrolyte consisting of the ionic liquid ([EMIM] [TFSI]) 1-ethyl-3-methylimidazolium bis (trifluoromethylsulfonyl) imide) and polymer PS-PMMA-PS (poly styrene-b- methylmethacrylate-b-styrene). These electrolyte-gated transistors using the CVD grown monolayer WSe_2 as the channel material have shown ambipolar transistor behaviour in these monolayer WSe_2 EDLTs. Ambipolar transistor behaviour was also observed in BP by ionic liquid gating using the ionic liquid N,N-diethyl-N-(2- methoxyethyl)-N-methylammonium bis(trifluoromethyl- sulfonyl)imide (DEME-TFSI) as the gate dielectric [31]. This method allows to widely tune the range of the Fermi energy from the valence to the conduction band. Additionally, the electric double layer formed at the liquid/solid interfaces allows to effectively accumulate or deplete charge carriers. Highly efficient gating with polymer electrolyte consisting of poly(ethylene oxide) (PEO) and lithium perchlorate ($LiClO_4$) have been shown for monolayer MoS_2 transistors [31]. The polymer electrolyte enhances the field-effect mobility by reducing the channel contact resistance and increasing the channel mobility. Top gating with ionic liquids has been widely used to facilitate charge control in the 2D materials. For example, electrostatic gating method was demonstrated using a solid polymer electrolyte consisting of poly(ethylene oxide) and cesium perchlorate ($CsClO_4$) on the exfoliated multilayer molybdenum ditelluride (2H-$MoTe_2$) 2D material [32]. Such solid polymer electrolytes have advantage over liquid electrolytes in such a way that the top gate can be evaporated onto the electrolyte surface and can further be patterned using electron beam lithography for metallization. The ON/OFF ratio of approximately 5 decades was reported for such solid polymer electrolyte-based FETs.

1.1 Problem Statement

Current BP photodetectors utilize high gate voltages to control the carrier transport in the BP channel and tune the detector response. This however limits the feasibility of integrating such devices with photonic or electronic circuits requiring low-voltage operation.

1.2 Thesis Objective

The objective of this thesis is to develop and characterize dual-gate BP photodetectors based on a solid polymer electrolyte top gate to reduce the photodetector operating voltage.

1.3 Review of recent progress on black phosphorous Photodetectors

Early in 2014, BP was proposed as an ideal material for near and mid-IR optoelectronics and electronic applications [33]. The current research in 2D layered photodetectors is centered on graphene [29], [33]–[36], insulating hBN [37]–[39] and TMDCs such as MoS_2 and WSe_2 [40]–[45]. The performance comparison of photodetectors with conventional and 2D semiconductor materials is illustrated in Figure 1.4. The major drawback as discussed in the previous section is that their applications are limited due to relatively low carrier mobilities of TMDCs and zero energy bandgap of graphene. The carrier mobility in TMDCs varies significantly from 10 to 200 $cm^2\ V^{-1}\ s^{-1}$ which is very low compared to mobilities of thin films of BP which is around 650 $cm^2\ V^{-1}\ s^{-1}$ to 1000 $cm^2\ V^{-1}\ s^{-1}$ at room temperature to 120 K [46]. Moreover, the anisotropic optoelectronic properties within the thin layers of BP also allow the development of novel infrared polarization sensors, phonon transport engineering and thin-film infrared polarizers.

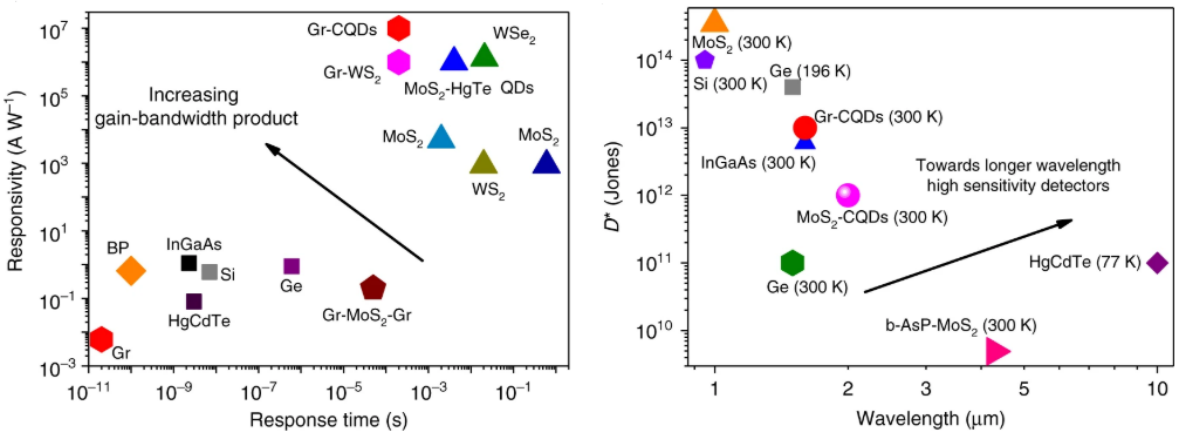

Figure 1.4 Figures of merit (Responsivities and Detectivities) of standard and 2D material based photodetection technologies (Reprinted with permission from [47]. Copyright © 2018, Springer Nature).

Photodetectors based on 2D layered materials have several advantages over their 3D counterparts. First, there is a strong absorbance despite the atomic thickness of these materials. There is also quantum confinement in the vertical direction that enables high light absorption efficiency which results from the sharp peaks in the density of states near the conduction and valence band edges [48]. These sharp peaks increase the likelihood of generating free electron-hole pairs when the incident photon energy is close to the bandgap. The light absorption efficiency is 2.3 % per atomic thin layer for graphene, 10 % for direct bandgap monolayer MoS_2 for 2 nm thickness, 95% for 300 nm thick MoS_2 films, 40% to 10 % for polarization sensitive BP with 70 nm thickness from armchair to zigzag polarization directions.

Graphene-Tungsten disulfide (WS_2)-graphene photodetectors based on heterostructures have shown high external quantum efficiency up to 30% [48]. Highly sensitive photodetection and gate tunable persistent photoconductivity with ultrahigh responsivity up to 10^{10} AW^{-1} have also been demonstrated for the graphene-MoS_2 heterostructure photodetectors [49]. The exceptional photo response in graphene-TMDC heterostructures is attributed to the strong optical absorption and visible range bandgap. Ultrahigh specific detectivity and photoresponsivity of 10^{15} Jones and 10^4 A W^{-1} and low dark currents have also been realized by sandwiching graphene in an atomically thin p-n junction i.e. MoS_2-graphene-WS_2 heterostructure [50]. The high photoresponse results

from the abundant photogenerated free carriers produced through efficient absorption by these three-layered materials MoS_2, graphene and WS_2.

High photoresponsivity photodetectors for MIR photodetection have been demonstrated by the narrow bandgap BP and black arsenic phosphorous (BAsP). Broadband photodetection from 532 nm to 3.39 μm was demonstrated by Xia et al based on BP transistor that exhibits high photoconductive gain, dynamic bandwidth in kHz range and capable of performing low power detection in picowatts range [51]. High photoresponsivity up to ~82 AW^{-1} at 3.39 μm have been shown using this BP photodetector. Extension of detection range to 7.7 μm have also been demonstrated using BP as its transport bandgap was observed to be effectively reduced by the application of vertical electric field. Peak responsivities of 518, 30 and 2.2 mA W^{-1} at 3.4, 5 and 7.7 μm respectively at 77 K have been shown for such widely tunable BP photodetector [52]. High performance long wavelength infrared photodetectors have also been reported using the narrow bandgap b-$As_{0.83}P_{0.17}$ phototransistor by Long et al for photodetection in the long wave infrared region (LWIR; up to ~8.05 μm) at room temperature for the first time [53]. Such photodetectors have also shown high specific detectivities up to 4.9×10^9 Jones for the 3-5 μm detection range with fast photoresponse and low dark noise. Although BP and BAsP have wide absorption spectrum, their responsivity and response time still needs to be improved for weak-signal and high-speed detection. To solve this, novel black phosphorus carbide (B-PC) that has a wide absorption spectrum up to 8000 nm was realized and a B-PC phototransistor with tunable responsivity and response time at 2004 nm wavelength was demonstrated [54]. Peak responsivity of 2163 AW^{-1}, shot noise equivalent power of 1.3 fW $Hz^{-1/2}$ at 2004 nm and fast response time of 0.7 ns was observed in this B-PC phototransistor that enables them for high-speed applications.

Table 1.1 summarizes the recently reported photodetectors based on 2D materials realized for high responsivities and ultrabroadband in the visible, near infrared and short-wave infrared regions. The higher mobilities of b-P and graphene provide high gain that helps to obtain high photoresponsivity. It can also be achieved through long photocarrier lifetime that can be obtained by incorporating defects in these 2D materials.

Table 1.1 Broadband Photodetectors based on 2D materials and their heterostructures [9].

Materials	**Wavelength range**	**Responsivity [A W $^{-1}$]**	**Bias [V]**	**EQE [%]**	**Response time**	**Reference**
b-AsP-MoS2	0.4-8.05 µm	0.22	0		0.54-0.52 ms	[53]
b-P/AsP	1-4.6 µm	17	0.5		8.6-12.4 µs	[55]
b-P	3.7-7.7 µm	0.518-0.0022	1.2			[52]
b-P	532 nm to 3.39 µm	1000-82	0.5	10^4	0.13 ms	[51]
b-PC	2.004 µm	2163	0.2	10^4	0.7 ns	[54]
b-P	640-940 nm	4.8×10^{-3}	0.2		1-4 ms	[56]
b-P	310-1240 nm	4.8×10^4	3	10^8	1 ms, 4 ms	[57]

The lattice structure in BP with built-in anisotropic electronic and optoelectronic properties produces interesting behaviour such as polarization sensitive photodetection. Anisotropic behaviour was observed in BP, $BAs_{0.83}P_{0.17}$ and their heterostructures. The photocurrent anisotropic ratio β that is defined as the ratio of maximum to minimum photocurrent (I_{pmax}/ I_{pmin}) was found to be ~10 and ~0.59 for BP/MoS_2 heterostructures [58] and $BAs_{0.83}$ $P_{0.17}$ based photodetectors [53]. Fast and high speed photodetection with bandwidth greater than 3 GHz have also been demonstrated based on BP that was integrated with the silicon waveguide [59]. The rapid photoresponse was shown for BP/Si heterostructure for 1550-1580 nm wavelength range with 0.2 MHz to 3 GHz frequency range and 3 G bit s^{-1} response speed. Photodetectors with high specific detectivity to obtain high sensitivity photodetection were also realized by obtaining high photoresponsivity and reducing the noise power. To obtain ultrahigh detectivity D*, the photodetectors must high light absorption induced photoresponsivity, the dark current and the noise power should be limited by the built-in electric field. Gate tunable detectivities were shown to

obtain ultrasensitive photodetection based on high gain of 2D materials. In such studies, D* were found to vary with gate voltages and incident intensities. High D* photodetectors based on BP were realized for wide wavelength range from 310-1240 nm with responsivity and detectivity equal to 9 $\times 10^4$ AW^{-1}, 3×10^{13} Jones respectively at 3 V bias voltage [57].

CHAPTER 2 DEVICE FUNDAMENTALS

This chapter elucidates the fundamental physical photodetection processes in BP photodetectors: photovoltaic and photoconductive detectors. It also explains the photocurrent generation mechanism in BP phototransistors based on these two effects. It also describes the concept of electrolyte gating and dual gating for FETs and photodetectors. Finally, it discusses the role of metal-semiconductor contacts for the device performance.

2.1 Photodetection mechanisms

Photodetectors based on 2D materials can be classified into two different categories. The first type of photodetector is based on the photovoltaic effect and photoconductive effect, where the optical transition excites free carriers. The second type of detector is based on thermal effect that includes the photo-thermoelectric effect. Photovoltaic and photoconductive detectors have been extensively exploited for 2D material-based semiconductors and thus the basic theory and operation of these types are discussed below:

2.1.1 Photovoltaic detectors

Photovoltaic effect results from the generation of electrical potential difference across the p-n or Schottky junctions under light illumination. Photovoltaic detectors are based include p-n junctions, heterojunctions, metal-insulator-semiconductor (MIS) photocapacitors, and Schottky barriers. A typical example of a photovoltaic detector is a p-n junction photodiode and its working principle is illustrated in Figure 2.1. Electron-hole pairs are created on both sides of the p-n junction as the photons with energy greater than the energy bandgap is incident on the front surface of the photodiode. The minority carriers diffuse on the opposite sides where they become majority carriers as the electron-hole pairs are separated by the strong electric field in the depletion region. This results in the generation of photocurrent that shifts the I-V curve of the diode in negative current direction as shown in Figure 2.1 (c).

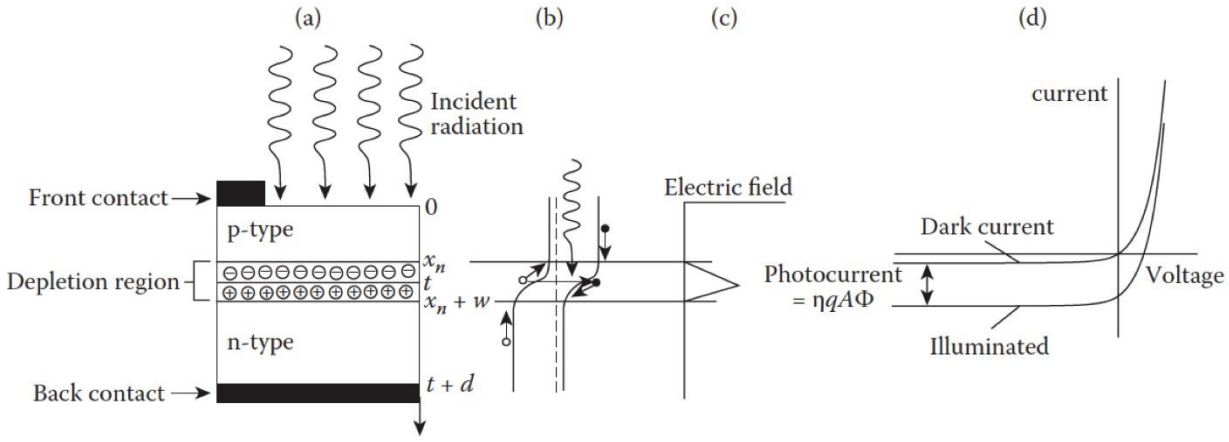

Figure 2.1 : An example of p-n junction photodiode a) schematic of p-n junction device b) Energy band diagram c) Electric field and d) I-V curves in dark and light (Reprinted with permission from [2]. Copyright © 2010, Taylor & Francis Group LLC).

However, in a real p-n junction photodiode, the dark current is limited by many other factors apart from diffusion. This includes generation-recombination current in the depletion region, tunneling through the depletion region, surface effects, ohmic leakage across the depletion region, impact ionization and space-charge limited current as depicted in Figure 2.2.

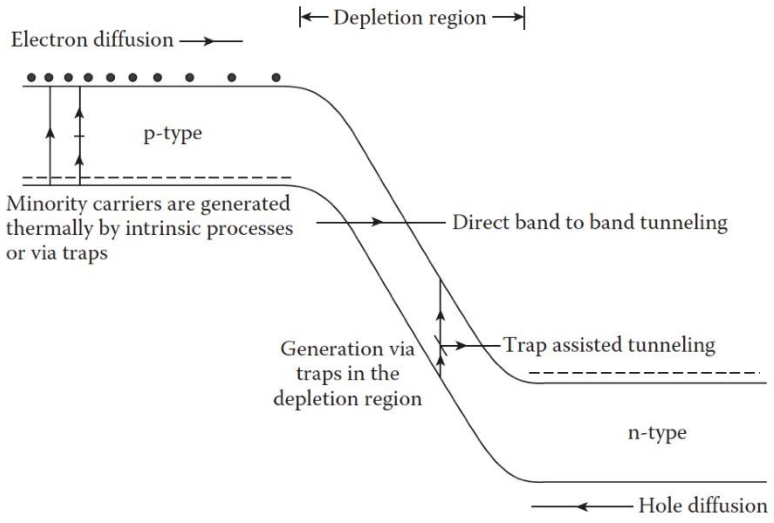

Figure 2.2 : Dark current generation mechanisms in a reverse biased p-n junction photodiode (Reprinted with permission from [2]. Copyright © 2010, Taylor & Francis Group LLC).

2.1.2 Photoconductive detectors

The photoconductive effect leads to change in the conductivity of the photosensitive material due to light-induced modification of carrier density. The two main parameters describing the performance of photoconductive detectors are photoconductive gain, which is related to the magnitude of photoconductance and the relaxation time that characterizes the response speed of photoconductance to the variation in the incident light intensity. The photoconductance gain (g) is defined as the ratio of the photo-generated carrier lifetime to the transit time as,

$$g = \frac{\tau}{t_t} = \frac{\tau \mu V_{DS}}{l^2} \tag{2.1}$$

where *l* is the source-drain separation distance, μ is the carrier mobility, τ is the free carrier lifetime and t_t is the transit time of electrons between ohmic contacts and V_{DS} is the source-drain bias voltage.

The structure of a basic photoconductive detector is shown in Figure 2.3 in which the electrical conductivity of the semiconductor material changes as the photons of energy higher than the bandgap is absorbed to produce electron-hole pairs. The optical absorption is higher in direct narrow bandgap materials than the extrinsic detectors. Changes in the conductivity are measured through the change in voltage across the material. The type of electrical circuit used for such measurement depends on the resistance of the material. For instance, a low resistance material, typically 100 Ω uses a constant current circuit shown in Figure 2.3, on the other hand a high resistance material utilizes constant voltage circuit where the signal change is determined through current changes in the circuit.

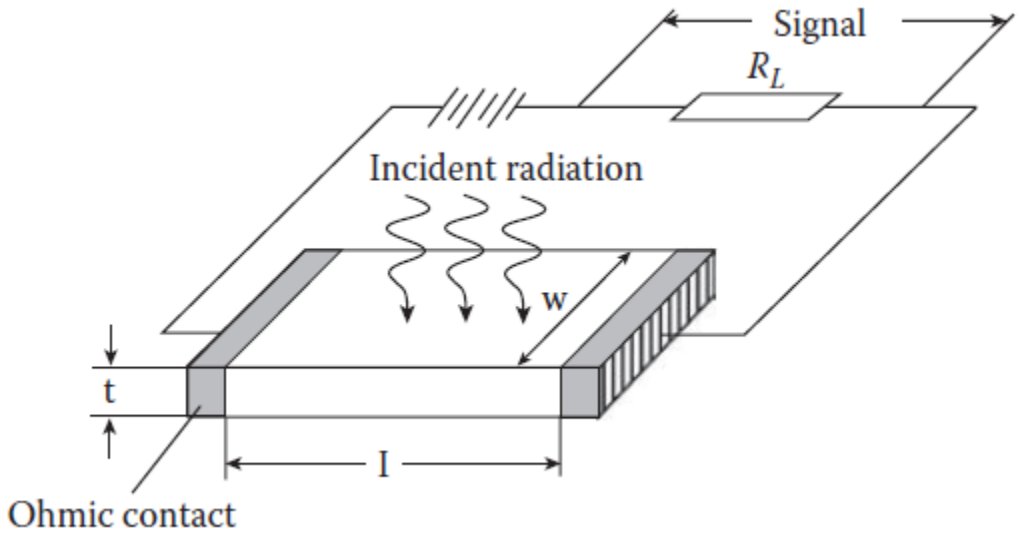

Figure 2.3 : Typical geometry of a photoconductive detector (Reprinted with permission from [2]. Copyright © 2010, Taylor & Francis Group LLC).

The photoconductive gain can be derived from the photocurrent, detection effect (photoconductive or photogating), the material and the configuration of detector as follows:

The expression to determine the photoconductivity under equilibrium excitation is given as

$$I_{ph} = q\eta A\phi_s g \tag{2.2}$$

where I_{ph} is the short circuit photocurrent (DC).

g is the photoconductive gain.

ϕ_s is the signal photon flux density.

A is the area of the photoconductor sample.

The total photocurrent arising from both the electrons and holes is given as

$$I_{ph} = \frac{qwt(\Delta n\mu_e + \Delta p\mu_h)V_b}{l} \tag{2.3}$$

The electron and hole carrier concentrations are given as

$$n = n_0 + \Delta n; p = p_0 + \Delta p \tag{2.4}$$

Where, n_0 and p_0 are the average thermal equilibrium carrier densities, Δn and Δp are the excess carrier concentrations.

μ_e and μ_h are electron and hole mobilities, V_b is the bias voltage.

In highly sensitive photoconductors, the net conductivity is majorly from electrons, and in addition to this uniform and full absorption of the incident light, the excess electron concentration given by the following rate equation

$$\frac{d\Delta n}{dt} = \frac{\phi_s \eta}{t} - \frac{\Delta n}{\tau} \tag{2.5}$$

The expression for excess carrier lifetime is therefore obtained as

$$\tau = \frac{\Delta n t}{\eta \phi_s} \tag{2.6}$$

Also, from equations (2.2) and (2.3), we have

$$g = \frac{t V_b \mu_e \Delta n}{l^2 \eta \phi_s} \tag{2.7}$$

Finally, the photoconductive gain can be simplified using equations (2.6) and (2.7) to give

$$g = \frac{\tau \mu_e V_b}{l^2} = \frac{\tau}{l^2/\mu_e V_b} \tag{2.8}$$

Thus, the photoconductive gain defined by equation (2.1) can be obtained as

$$g = \frac{\tau}{t_t}, t_t = l^2/\mu_e V_b, \tag{2.9}$$

The photoconductive gain depends on the drift length $L_d = v_d/\tau$ and interelectrode spacing l. For instance, in the case of $L_d > l$, the free charge carrier extracted at one electrode will immediately result in the injection of equivalent free charge carrier at the opposite electrode. This cycle of generation of free charge carrier continues until there is recombination.

Another mechanism related to the photoconductive effect is photogating effect which is generally observed in semiconductors with high dislocation or defect densities. In this case, trap states inside the defective semiconductor or at the surface capture either electrons or holes. For instance, in an n-type semiconductor with hole trap states, the holes get trapped by defects and only photogenerated electrons contribute to the photocurrent. An extra gate voltage is induced by the trapped holes. The photogating effect therefore generates an extra gate voltage on the conducting channel.

2.2 Photocurrent mechanism in BP Phototransistors

Photocurrent generation mechanism in BP phototransistors is based on the conventional photovoltaic effect and photoconductive (including photogating) effect discussed in the above sections. The photovoltaic effect is observed in the case of intrinsic regime where there is low channel carrier density and longer lifetimes of the photogenerated electrons and holes. However, photogating generates photocurrent which is directly proportional to the trans-conductance gain given as $I_{ph} = g_m \Delta V_{th}$, ΔV_{th} is the modulation in the transistor threshold voltage resulting from the localized trapped states from the photogenerated electrons or holes. A large photoconductive gain is observed as a result of longer recombination lifetime due to the localized tap states of either electrons or holes. The photoconductive gain decreases with the increase in the incident optical powers as the traps are filled. However, a high mobility channel, large source-drain voltages or shorter channel length can still provide photoconductive gain even if the localized trap states are limited.

The influence of photogating in structures of the type shown in Figure 2.4 (a) was through the photocurrent dependence on gate voltage and incident powers from Ref. [60] is depicted in Figure 2.4 (b) detailed in Ref. [60]. At low incident powers, the dominant mechanism for photocurrent generation is the photogating effect since the photocurrent-gate voltage curve follows the trans-conductance curve.

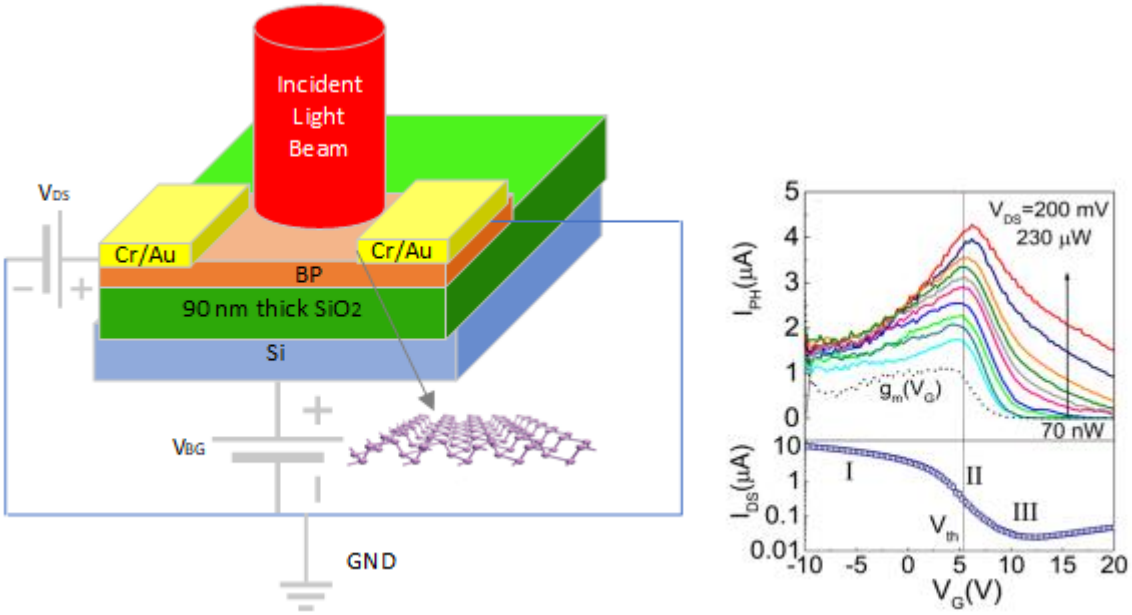

(a) (b)

Figure 2.4 : a) Schematic of BP photodetector in phototransistor mode b) Upper panel: Photocurrent vs Gate Voltage, Lower Panel: Transfer curve ((b) Reprinted with permission from [60]. Copyright © 2016, American Chemical Society).

The band energy diagrams of this BP device for different modes of operation is also shown in Figure 2.5. The dislocations and grain boundaries in BP, random distribution of trapped charges at the BP-metal contact interfaces and vacancies can result in inhomogeneous potential distribution. In general, the electron traps present for energies above fermi level E_F whereas the hole traps are present for energies below E_F. The photoconductive response studied through energy band diagrams for three regions: $V_G<V_{th}$, $V_G=V_{th}$ and $V_G>V_{th}$ to understand the photocurrent-gate voltage response at different incident powers. In region I of Figure 2.4 (b), the photocurrent increases with gate voltage and incident powers. This can be explained from the energy band diagram shown in Figure 2.5 (a). In this region, the hole trap states are close to E_F are mostly occupied but the electron traps are almost empty in the dark conditions. However, under light illumination, the electrons are trapped by these empty traps that increase the hole lifetimes and therefore photoconductive gain. As the gate voltage becomes more negative, the probability of electron-hole pair recombination increases that leads to reduced responsivity. As the gate voltage increases, and equals to V_{th} (region II), the fermi level moves to higher energy as shown in Figure

2.5 (b). In this regime, the electrons are trapped and the photogenerated hole lifetimes are still higher that gives photoconductive gain and maximum photocurrent. In contrast to the first two regimes, region III where $V_G > V_{th}$ has both electron and hole trap states that results in the trapping of both photocarriers. This results in reduced photocurrent as shown in region III of Figure 2.4 (b). Finally as the incident powers are increased the trap states are filled gradually and therefore more number of photogenerated electrons and hole are available even when the transistor is in OFF state as shown in Figure 2.4 (b). Thus, the responsivities increase with the incident powers.

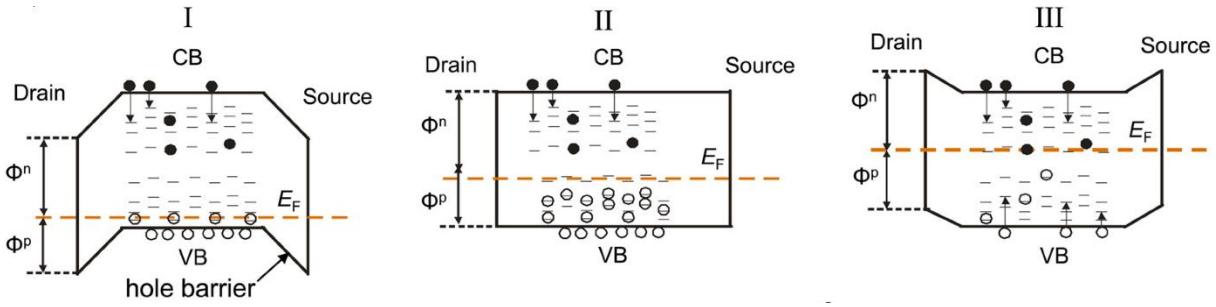

Figure 2.5 : a) Band energy diagrams of BP photodetector a) VG<Vth b) VG≈Vth and c) VG>Vth (Reprinted with permission from [60]. Copyright © 2016, American Chemical Society).

2.3 Electrolyte-gated BP photodetector

Electrolytes have been extensively studied as gate insulators for a wide range of applications including thin film transistors for flexible electronics and biosensing. The major advantage of employing these electrolytes in FETs is their large capacitance of the order of 1-10 μF/cm^2. The primary advantage of having high capacitances is that they provide low voltage operation of these devices, low source and drain contact resistances and low power consumption. Thus, the devices with electrolytic gating approach are suitable for integrated and flexible electronics/photonics circuits. The capacitance effect can be understood by considering the transistor drain current in the linear regime ($V_{DS} \ll V_{GS}$) as

$$I_{DS} = \frac{W}{L}\mu C(V_{GS} - V_T)V_{DS} \tag{2.10}$$

where W is the channel width, L is the channel length, V_{GS}, V_{DS} and V_T are the gate-source, drain-source and threshold voltages respectively.

Thus it can be observed from equation (2.6) that larger capacitance provides lower V_{GS} and V_{DS} values for fixed I_{DS} or it can enhance I_{DS} at fixed V_{GS} and V_{DS}. Electrolyte gating can also be applied for BP phototransistors to increase current since the charge carriers in BP can be effectively modulated by electrolyte gate voltage and this can enhance photoresponse of the devices.

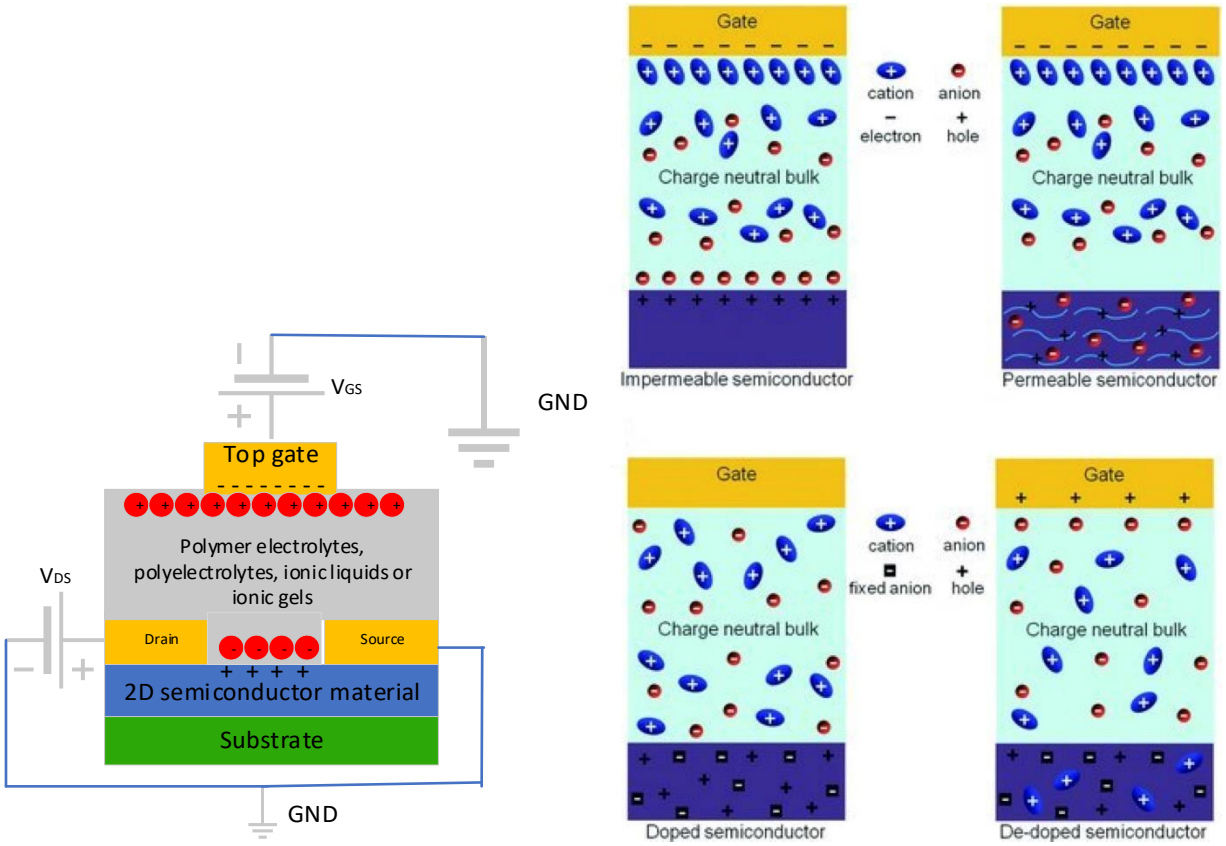

(a) (b)

Figure 2.6 : (a) Typical cross section of an electrolyte gated transistor (EGT) (b) Carrier transport modes in permeable and impermeable semiconductors (Reprinted with permission from [61]. Copyright © 2012, John Wiley and Sons).

2.3.1 Electric Double layer transistors (EDLTs)

A typical structure of EGTs is shown in Figure 2.6 (a). The basic mechanism of EGTs can be classified into two types: Electric double layer transistors (EDLTs) where the semiconductor is impermeable to the ions of the electrolyte and Electrochemical transistors (ECT) in which the semiconductor is impermeable to the ions of the electrolyte as shown in Figure 2.6 (b). In EDLTs, the electric double layers are formed at gate-electrolyte and electrolyte-semiconductor interfaces. These are formed when gate voltage is applied to gate electrode that leads to accumulation and migration of ions at the two interfaces. These EDLs that are equivalent to nanometer thick capacitors that allow high carrier densities in the semiconductor channel leading to high source-drain current as explained in the above section. The modes of operation for a p-type EDLTs are illustrated through the band energy diagrams shown in Figure 2.7 (a). The three basic modes of operation for both EDLTs and ECTs are accumulation ($V_{GS} < V_{FB}$), depletion ($V_{GS} > V_{FB}$) and flat-band ($V_{GS} = V_{FB}$). In the depletion mode, the injection of electrons at the source-semiconductor interface is prevented due to the large potential barrier at this interface, whereas in the accumulation mode, large number of holes from the source electrode can be injected into the valence band of the semiconductor. Thus, the EDLT configuration is appropriate for applications involving fundamental carrier transport modulation without ions penetrating inside the semiconductor material.

2.3.2 Electrochemical transistors (ECTs)

The second configuration which is the Electrochemical transistors (ECTs) utilize electrochemical doping that can be seen in ion permeable semiconductors (e.g. Polymer semiconductors). Although EDLs are formed at the two interfaces, the ions on the semiconductor side diffuse into the semiconductor layer and by inducing charge carriers that flow between source and drain contacts. The comparison of depletion and accumulation modes of an ECT with the EDLT is illustrated in Figure 2.7 (b). In the case of ECT, one the double layer moves to the semiconductor-source instead of electrolyte-semiconductor interface since the material used is a permeable semiconductor for ECTs. Thus, this creates a difference in the injected hole distributions into the semiconductor as compared to the EDLT accumulation mode as shown in bottom Figure 2.7 (a) and (b). Thus, the

ECTs are suitable for applications involving high current as drive currents can be huge due to the electrochemical doping.

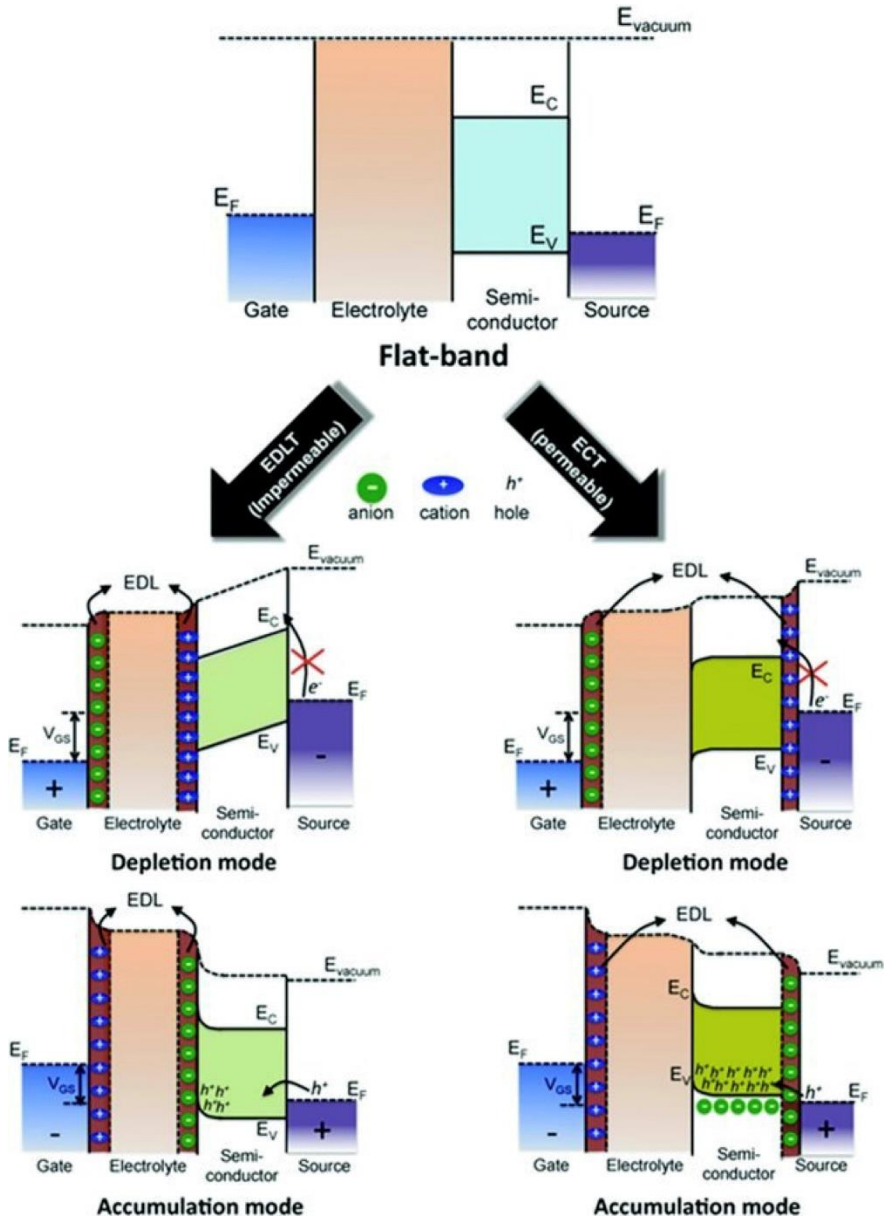

(a) (b)

Figure 2.7 : Carrier transport modes in permeable (ECT) and impermeable (EDLT) semiconductors (Reprinted with permission from [61]. Copyright © 2012, John Wiley and Sons).

2.4 Dual gate phototransistor operation

Dual gate design for FETs offers promising applications to enhance the performance of the device and in particular for photodetectors it can provide high sensitivity, wavelength tunability, high photoconductive gain, low electrical noise and low operating voltages [62]–[65]. An example of dual gate phototransistor based on ambipolar organic semiconductor that can operate in both n-type and p-type modes based on the applied gate voltage is shown in Figure 2.8. The conductive n-type and p-type channels are formed simultaneously when the two gates are of opposite polarity. The structures that are used to separate photogenerated electrons and holes, and band diagrams for different types of photodetectors: photodiode, phototransistor and dual-gate phototransistor are also illustrated in Figure 2.8.

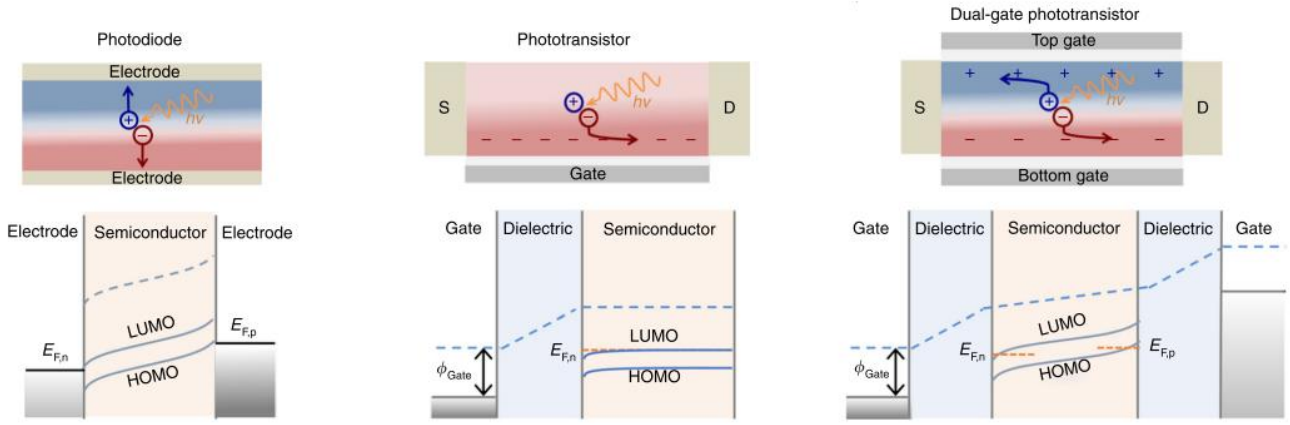

Figure 2.8 : Energy band diagrams for (a) photodiode (b) phototransistor and (c) dual-gate phototransistor (Reprinted with permission from [64]. Copyright © 2018, Springer Nature).

The basic mechanism in all three types of photodetectors is the formation of electron-hole pairs when light is absorbed in the semiconductor layer. These electron-hole pairs need to be separated using metal electrodes to collect photocurrent. Thus, a photodiode uses two metal electrodes on the either side of the p-n junction to collect photocurrent that can enhance charge separation by applying electric field between the two electrodes. In contrast, phototransistors collect only one type of charge carrier at the interface of dielectric-semiconductor (e.g. holes for p-type conductive channel) while the opposite charge carrier is trapped inside the semiconductor to provide high photoconductive gain. The interesting and emerging structure for FETs or photodetectors is a dual-

gate phototransistor similar to p-n junction as it uses top and bottom electrodes to extract the photogenerated electrons and holes. Thus, it can simultaneously form p-type and n-type accumulation channels that can simultaneously conduct opposite charges with the gate voltages of different polarity. Thus, the dual-gate phototransistor configuration is promising for semiconductors that can also show ambipolar transport behaviour like BP. The carrier transport and optical properties of FETs/photodetectors can be effectively tuned with the top and bottom gate voltages.

2.5 Role of Metal contacts in BP photodetector performance

The metal contacts are crucial for realizing good 2D semiconductor-based optoelectronic devices. The work function of the metal used as contacts to the BP flakes determine the type of carrier conduction at the metal-BP interface Schottky barriers (SB). For example, high work function metals can provide higher carrier densities and high source-drain currents due to reduced SB height for hole injection, whereas the low work function metals allow both p-type and n-type ambipolar conduction in the BP channel.

Two types of metal-semiconductor contacts can occur: ohmic and Schottky contacts. Ohmic contact follows a linear I-V relation. The carriers easily tunnel through the potential barrier at the junction since the depletion region is very narrow that usually is obtained for a highly doped semiconductor. Schottky contacts provide conduction with only one type of carrier either electrons or holes that is due to the wide depletion region barrier and thus it is referred to as rectifying contact. This barrier is formed due to difference in the metal and semiconductor work functions. For instance, for a Schottky contact with an n-type semiconductor, the metal work function ϕ_m should be greater than the semiconductor work function ϕ_s and vice-versa for p-type semiconductor. Figure 2.8 shows the energy band diagrams at equilibrium for these two types of Schottky junctions and the barrier heights for these two junctions can be given as

$$\phi_{bn} = \phi_m - \chi_s, \phi_{bp} = \chi_s + E_g - \phi_m \tag{2.11}$$

where E_g is the bandgap and χ_s is the electron affinity of the semiconductor. The electrostatic potential barrier ψ_s is given as

$$\psi_s = \phi_m - \phi_s \tag{2.12}$$

Also, for the same metal on n-type and p-type of the same semiconductor, ϕ_{bn} and ϕ_{bp} follow

$$\phi_{bn} + \phi_{bp} \cong E_g, \phi_{bn} > \frac{E_g}{2}, \phi_{bn} > \phi_{bp} \tag{2.13}$$

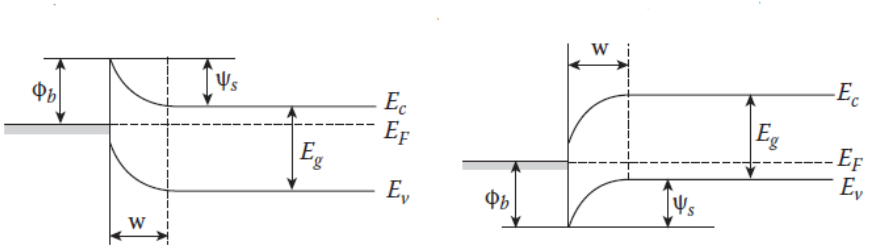

Figure 2.9 : Energy band diagrams at equilibrium for metal-semiconductor Schottky contacts (a) n-type (b) p-type (Reprinted with permission from [2]. Copyright © 2010, Taylor & Francis Group LLC).

The metals with larger work function (e.g. Pd: 5.1 eV) as contacts in BP FETs have shown to reduce the SB height for hole injection that provides high hole drain current. However, BP FETs with low work function metal contacts (e.g. Al: 4.1 eV) have shown ambipolar characteristics [66]. The SB heights play a crucial role to determine the ON/OFF ratio of these transistors. Thus, the ON/OFF ratio is higher for the high work function metals because of their low SB heights. Also, for low work function metal contacts, SB height increases for holes and decreases for electrons at the contact and this leads to ambipolar transport in such devices. The optimized metal contacts should therefore reduce the SB height that improves the collection of photo-generated carriers and the responsivities. Thus, a high work function metal can tune the responsivities with gate voltage due to changes in the SB height. For example, in a p-type BP phototransistor, the responsivity increases at negative back gate voltages since there is reduction in SB becomes narrower that allows holes to move from the barrier easily. However, as the gate voltage is increased and becomes positive, the responsivity decreases since the barrier width increases that limits the collection photo-generated carriers at the metal contacts. Thus, contact engineering is essentially required to develop a high-performance photodetector that can reduce the barrier height for the easy collection

of photogenerated electrons and holes, and help to obtain broadband photodetection with high responsivities.

CHAPTER 3 EXPERIMENTAL WORK

3.1 BP FET and Photodetector structures

This chapter discusses the experimental work performed in this thesis. The different configurations of BP based devices studied in this work is shown in Figure 3.1. First, the conventional Si bottom gate BP devices based on the configuration presented in Figure 3.1 (a) are fabricated and characterized to correlate with the physical understanding of basic photocurrent generation mechanism of BP FETs and photodetectors as discussed in the previous chapter. Next, the concept of polymer electrolyte gating with dual-gate phototransistor configuration is introduced through the devices fabricated using the configuration presented in Figure 3.1 (b). The devices are extensively studied to demonstrate and compare the working mechanism of traditional BP devices and the polymer electrolyte-based BP photodetection in both visible and NIR wavelengths.

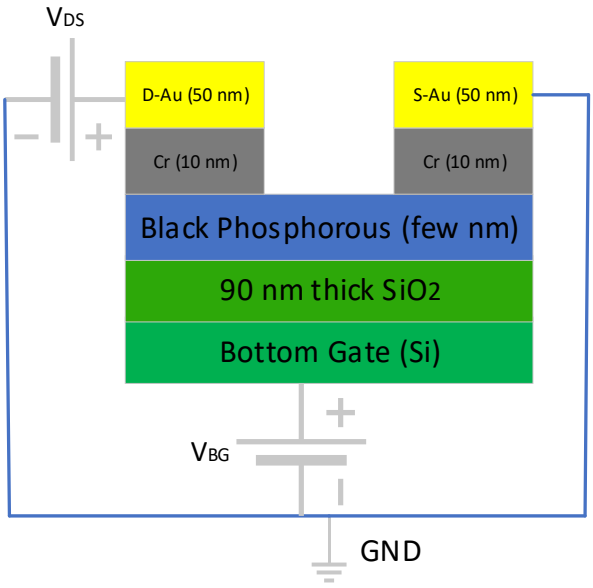

(a)

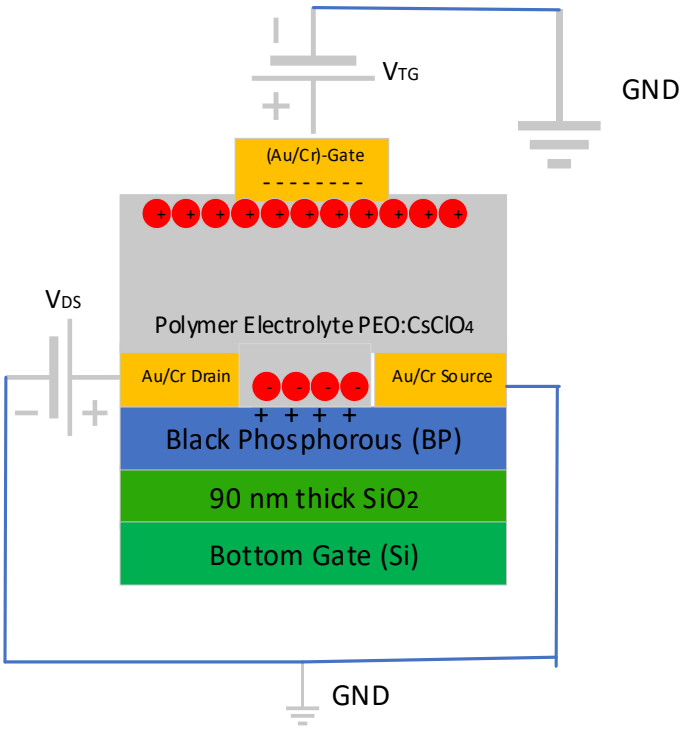

(b)

Figure 3.1 Schematic/Cross section of a) Traditional bottom gate BP FET and/or photodetector, b) Dual gate PEO:CsClO4 polymer electrolyte based BP photodetector.

3.2 Fabrication method

The fabrication of all the BP based devices involves a series of different steps that are presented in the following section

3.2.1 Patterned substrates with alignment markers

The fabrication of 2D semiconductor-based devices require substrates with optical alignment markers as they help to determine the flake positions that are required for designing and fabricating metal contacts using electron-beam lithography. Thus, the first step in the fabrication of BP devices requires silicon substrates with alignment or location markers which are fabricated by photolithography.

The silicon prime wafer (Graphene Supermarket) is cleaned with acetone and isopropanol (IPA), and then vacuum baked at 120 ºC for dehydration of silicon wafer to obtain clean and stable

surfaces for the subsequent processes. The Si substrate with markers is fabricated by standard lift-off with a negative photoresist. The substrate is spin coated with AZ5214 EIR photoresist at 4000 RPM for 30 seconds followed by softbake at 110 ºC for 50 seconds. It is then UV exposed through a predefined photomask for 6 seconds (typically exposure is 56 mJ/cm^2 for this photoresist) and post exposure bake at 104 ºC for 2 minutes. It is developed in AZ726 MIF developer solution for 1 minute and then rinsed with DI water. Next, the patterned substrate is cleaned with photoresist descum process in the plasma system for few seconds. This process removes the residual photoresist after development to improve the uniformity and sidewall of the photoresist mask. Finally, 5 nm Titanium (Ti) and 50 nm gold (Au) is deposited by electron beam evaporation. The substrate is then soaked in acetone solution at room temperature for around three hours for lift-off to obtain the gold markers.

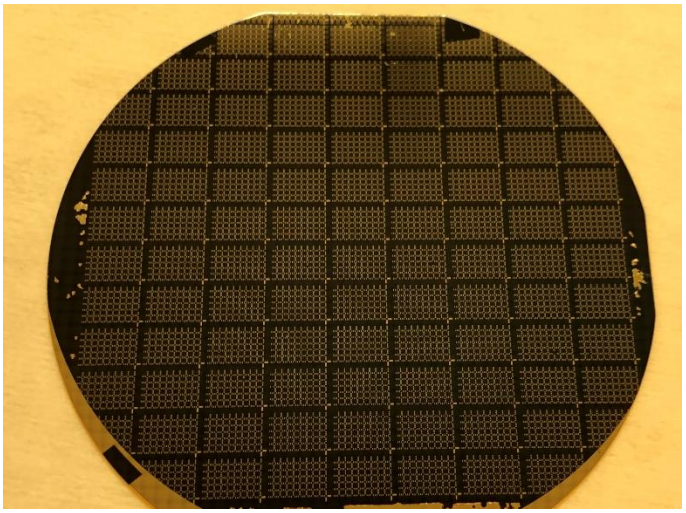

(a)

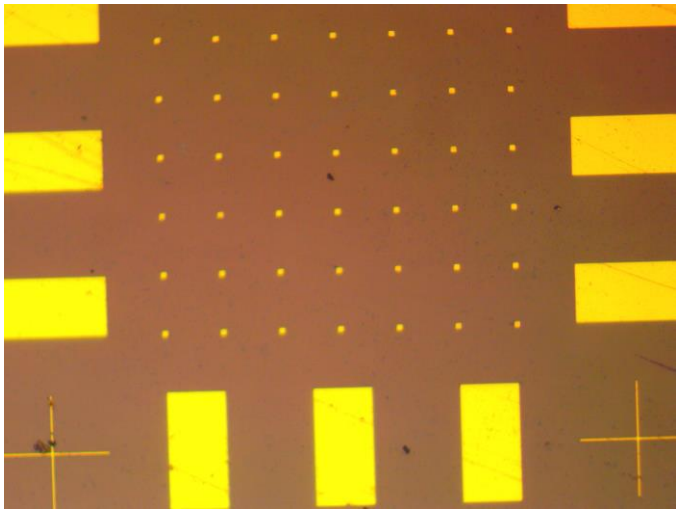

(b)

Figure 3.2 (a) Patterned Si wafer with Ti/Au markers (b) Optical Image of Si substrate with optical markers (diced from Si wafer in (a))

3.2.2 Substrate treatments and Exfoliation method

The p-type Si/SiO_2 substrate (Graphene Supermarket) with 90 nm oxide and gold alignment markers is first treated with oxygen plasma after regular cleaning with acetone and IPA. The oxygen plasma cleaning is performed in a plasma system (PVA Tepla, Model GIGAbatch 310) at 500 W power and for a duration of 30 minutes. This helps to remove the residual resist that was used as protective layer for the wafer dicing step. The substrate is then processed using an HMDS (hexamethyldisilizane) vapor priming recipe in the YES oven (Yield Engineering Systems, Model YES-310TA). It improves the surface adhesion properties besides dehydration that reduce the surface moisture. Thus, the advantages of combined dehydration and HMDS priming in the same chamber of YES oven offers necessary surface treatment for BP exfoliation.

The thin flakes of black phosphorous on the above Si/SiO_2 substrates are produced by hot mechanical exfoliation method using a PVC tape (SPV 224PR-M, Nitto Denko) inside glovebox. This method allows to obtain larger size high quality flakes with higher yield. First, the cleaved BP crystals (Smart Elements) are deposited on the nitto tape and then BP crystals are repeatedly pressed by folding the tape in half, sticking itself and pulling it apart, and this is repeated few times

to have thinner flakes distributed on the tape. Next, the tape with BP flakes is pressed on the substrate by applying firm pressure by gently pressing with the tweezers such that the substrate and BP flakes on the tape are in good contact. Then, the substrate with nitto tape is placed on a hotplate at 120 ºC for 2-3 minutes. Finally, the substrate is cooled at room temperature and then removed from the tape slowly. Additionally, the tape residues from the substrate are removed by soaking it in acetone for 20 minutes, followed with IPA rinse for 30 secs and drying. The substrate is also heated on hotplate for 1-2 hours at 200 ºC to remove all the solvent residues before depositing Poly(methyl methacrylate) (PMMA) e-beam resist for metallization.

3.2.3 Metallization

The metal contacts are deposited on the exfoliated BP flakes by using the standard electron beam lithography (EBL, Raith e-line). First, the location of the flakes is determined optically for the electron beam lithography (EBL) patterning of contacts on top of these flakes. The substrate with exfoliated BP flakes after undergoing the surface treatments before and after exfoliation is spin coated with PMMA A4 495 e-beam resist at 2000 RPM for 45 seconds to obtain ~180 nm thickness. It is annealed at 150 ºC for 3 minutes. Source, drain and top gate contacts are fabricated onto the flakes by EBL. The EBL patterned substrate is developed in glovebox in 1:3 Methyl isobutyl ketone (MIBK) and IPA for 1 minute and 5 seconds respectively. The development process is crucial in glovebox to protect BP from oxidation effects. Chromium 5 nm and gold 50 nm are deposited by vacuum thermal evaporation (Evovac, Angstrom Engineering) in glovebox at a deposition rate of 0.5 Å/s and 1 Å/s respectively. The sample is put in acetone beaker at room temperature in glovebox overnight for lift-off. Finally, the fabricated device with metal contacts is annealed at 200 º C for an hour on hot plate that improves the BP-metal contacts. The devices are also protected by using a thin layer of Al_2O_3. It is formed by depositing 3 nm Al by vacuum thermal evaporation at a deposition rate of 0.3 Å/s and when exposed to ambient conditions.

3.2.4 Polymer Electrolyte Deposition

The polymer electrolyte gate for the dual-gate BP device based on the electrochemical gating approach is prepared in glovebox by dissolving polyethylene oxide PEO (Sigma-Aldrich) and Cesium perchlorate $CsClO_4$ (ThermoFisher Scientific) in anhydrous acetonitrile (Sigma-Aldrich)

with 1 wt% solution concentration and molar ratio of 76:1. The electrolyte solution is drop casted using a 0.45 um PTFE membrane filter on the bottom gate BP photodetector that is then followed by thermal annealing at 90 ºC on hot plate for 10 minutes in glovebox. The electrolyte top gate contact is then obtained using Au/Cr pads which were fabricated by thermal evaporation prior to the polymer electrolyte deposition.

3.3 Characterization methodology

Exfoliated flakes BP and devices were characterized to study the structural, transport, optical and device characteristics through several methods. This involves optical characterization of BP flakes through atomic force microscopy (AFM), optical microscopy, polarized Raman spectroscopy measurements etc. Next, BP device characterization involves electrical I-V measurements to obtain the output and transfer curves of FETs and photodetectors using an electrical probe station and Keithley source meter. Finally, the optical device characterization includes measurements of the photocurrent and responsivity in the visible and infrared regions using the setup shown in APPENDIX A.

3.3.1 Optical Characterization of exfoliated BP flakes

The optical analysis of exfoliated BP flakes is performed by taking microscope images. The optical images are used to determine the flake distribution, yield, size, thickness and location on the substrate using the reference alignment markers. The flakes with suitable thickness and sizes greater than 10 µm are selected for further processing and fabrication of devices.

Polarized Raman spectroscopy measurements are performed on exfoliated BP flakes protected by PMMA layer at 500 µW incident power (integration time of 10 seconds and spot size of approx. 1 µm), 532 nm excitation wavelength and using an 100 x objective lens with a half wave plate that rotates the polarization of the excited beam.

The surface characterization is performed using an Atomic force microscopy setup (AFM D3100 Nanoscope) to determine the thickness of the BP flakes.

3.3.2 Electrical Characterization

The electrical output (I_{DS}-V_{DS}) and transfer characteristics (I_{DS}-V_{GS}) is performed using a two-channel source meter (Keithley 2614B) in the glovebox and ambient conditions. The electrical probe station (Everbeing International Corp.) consists of micro-positioner (EB-050-80), tip holder (TH-TU-C) and tungsten probing tips (T20-50).

3.3.3 Responsivity and Photocurrent Measurements

The photocurrent and responsivity spectra measurements are performed using swept monochromatic excitation and broadband Fourier transform infrared spectroscopy (FTIR) setup (shown in APPENDIX A). The visible and near-infrared measurements are performed using a high-power supercontinuum fiber laser (Fianium Whitelase). The light beam from this source is focused on the sample using a monochromator (SP-500i, Princeton Instruments) with a set of optical components (APPENDIX A) that provides single wavelength excitation tunable in the wavelength range from 350 nm to 1700 nm. The single wavelength measurements are performed using this setup by measuring the output and transfer characteristics in dark and illumination conditions to obtain photocurrent and responsivity. However, for a full spectral photocurrent and responsivity measurements, the signal is measured with lock-in detection. For such measurement, the light from the supercontinuum laser (repetition rate 40 MHz) and monochromator is passed through an optical chopper at a frequency of 500 Hz. The signal from the photodetector is then passed to a current preamplifier (SRS570, Stanford Research Systems) which is followed by a lock-in amplifier (MFLI, Zurich Instruments).

The Infrared measurements (above 1.7 um) are performed using a step-scan measurement program (OPUS software) with FTIR (Vertex 70) internal tungsten NIR broadband light source and with lock-in detection. In this case, the signal from the lock-in amplifier is passed to the FTIR interface. The power profiles of NIR and MIR sources are measured using a built-in DLaTGS pyroelectric detector. These intensities are varied by changing the internal aperture setting of the FTIR setup. The absolute responsivities in the visible and near-infrared ranges are computed by using the calibrated Si and InGaAs reference detectors.

3.4 Results and discussions

Polarized resolved Raman spectroscopy is performed on the exfoliated thicker and larger BP flakes in Figure 3.3 to determine the characteristic Raman peaks for BP. The laser spot is aligned in the center of the flake and in the region of uniform thickness. The Raman intensities are measured at different angles by using a half wave plate. The polarized Raman spectroscopy results for the two flakes are shown in Figure 3.4 and Figure 3.5. The three characteristic Raman peaks for BP flakes can be observed at 363.6 cm^{-1}, 440.1 cm^{-1} and 468.3 cm^{-1}, which is consistent with the previous reported values and these peaks correspond to A_g^1, B_{2g} and A_g^2 respectively. It can also be observed that the peaks are independent of the polarization angle, however their intensity is varied with this angle. Thus, high values of the A_g^2 peak is observed for the principle (AC) axis than in the ZZ direction.

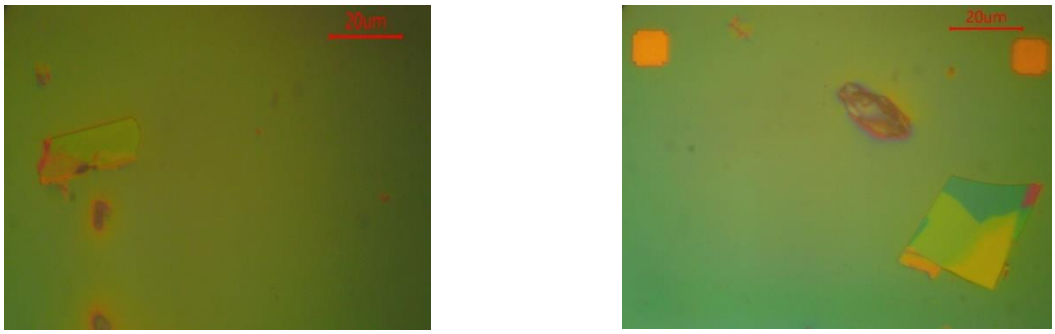

(a) (b)

Figure 3.3 BP flakes mechanically exfoliated p-type 90 nm SiO2 substrate (a) Flake-1 and (b) Flake-2.

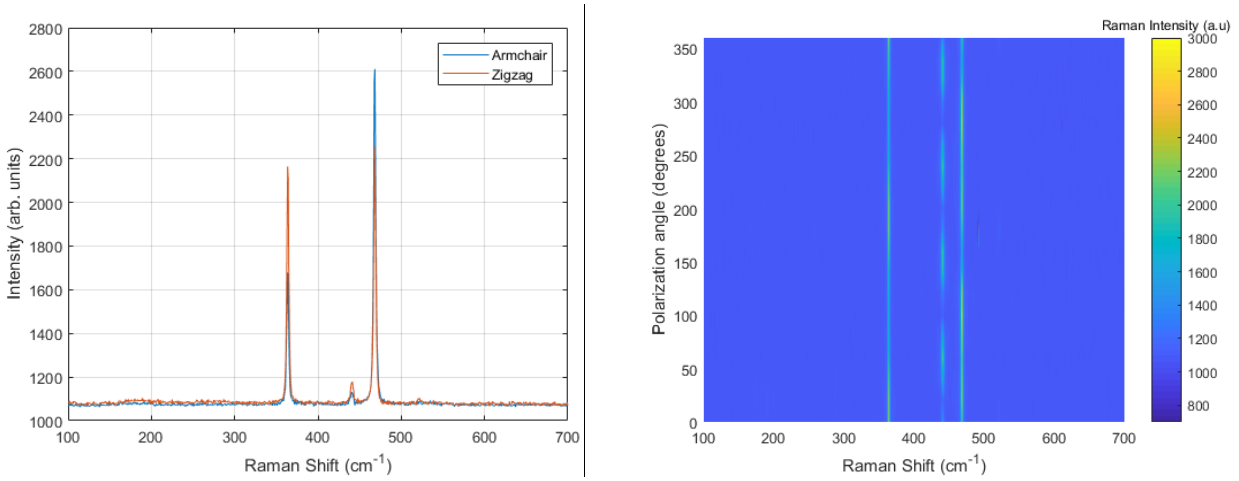

(b) (b)

Figure 3.4 Raman Spectroscopy results a) AC vs ZZ b) Polarized Spectra (Flake-1).

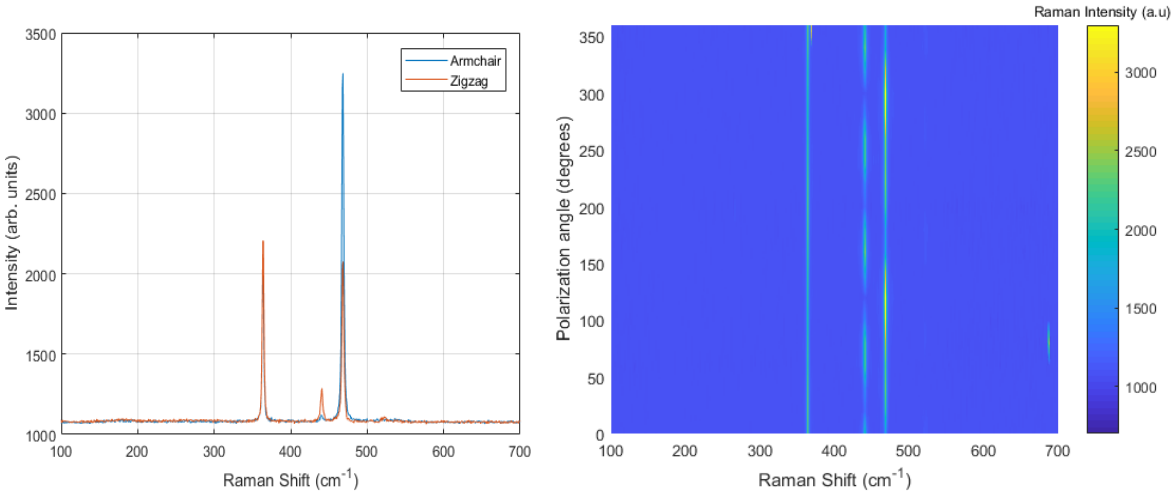

(a) (b)

Figure 3.5 Raman Spectroscopy results a) AC vs ZZ b) Polarized Spectra (Flake-2).

However, alloying BP with Arsenic can significantly change the position of these three peaks. This can be observed in Figure 3.5 where $B_{0.5}As_{0.5}P$ flakes are characterized by polarized Raman spectroscopy measurements. The polar peaks A_g^1, B_{2g} and A_g^2 are found at 227.8 cm^{-1}, 237.8 cm^{-1} and 253.5 cm^{-1} which are close to the previously reported values (224 cm^{-1}, 233 cm^{-1} and 256 cm^{-1}).

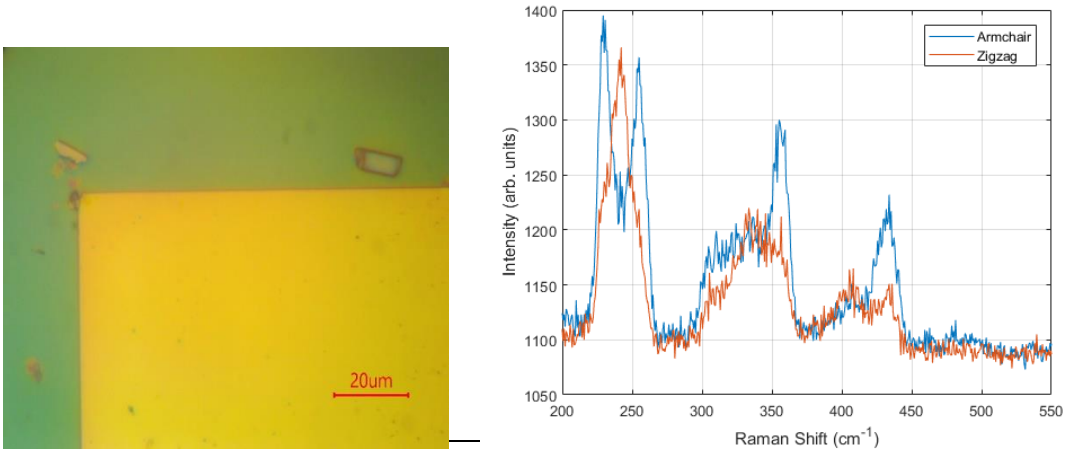

(a) (b)

Figure 3.6 a) Optical image of exfoliated $B_{0.5}As_{0.5}P$ b) AC vs ZZ Raman Spectra (Flake-1).

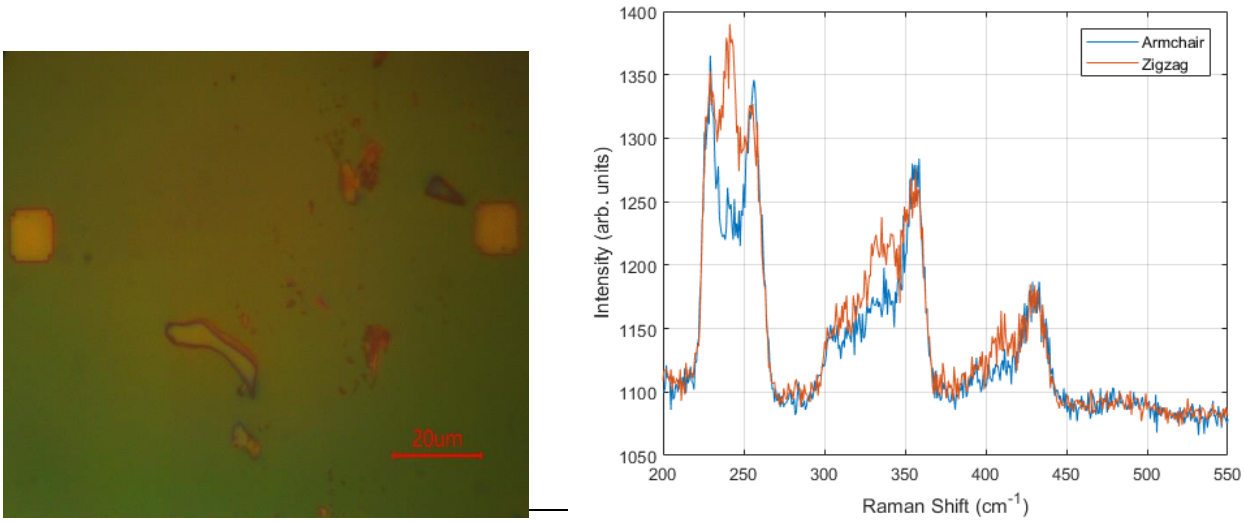

Figure 3.7 a) Optical image of exfoliated $B_{0.5}As_{0.5}P$ b) AC vs ZZ Raman Spectra (Flake-2).

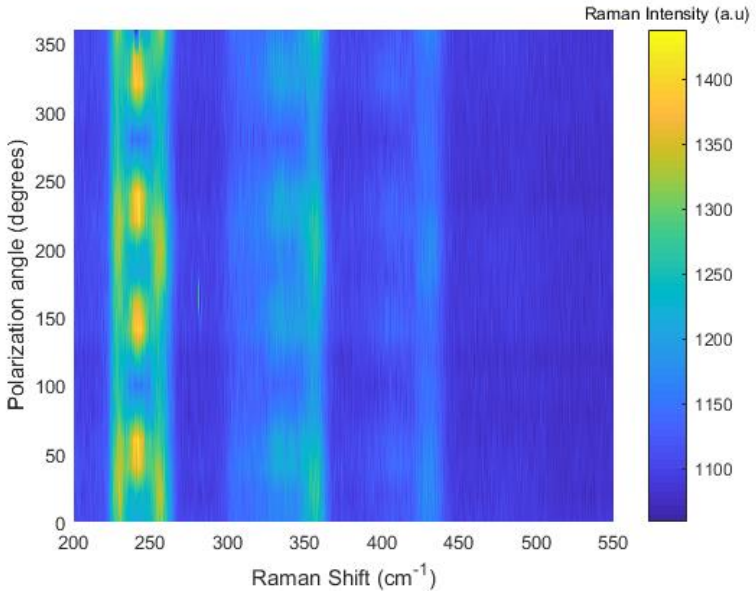

Figure 3.8 Polarized Raman spectrum for $B_{0.5}As_{0.5}P$ (Flake-1).

The optical images of all the BP devices studied are shown in Figure 3.9. The objective of studying different BP FETs and phototransistors is to understand the carrier conduction, current modulation, source-drain voltage, gate voltage and incident power dependence for both electrolyte top gate and Si bottom gate configurations.

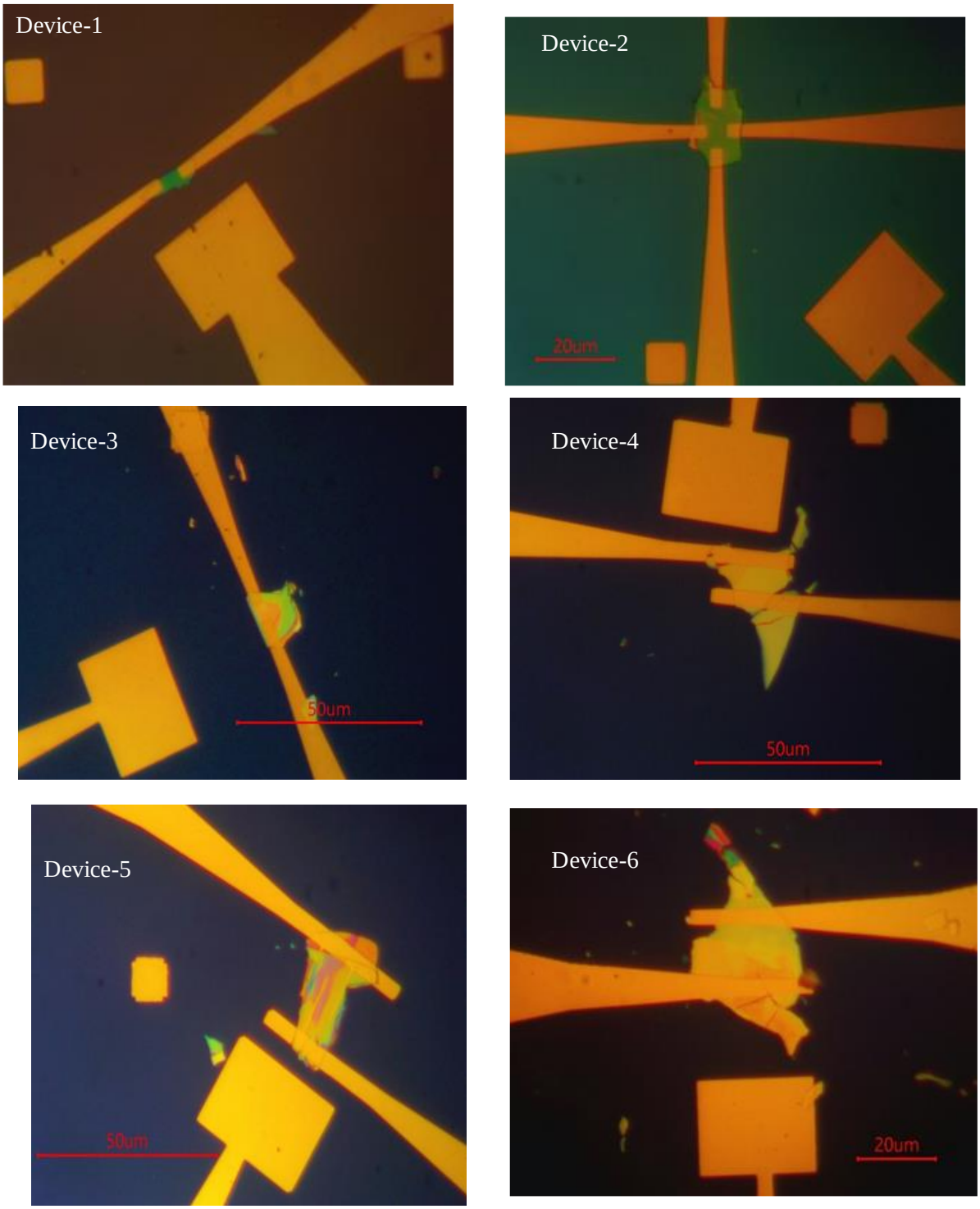

Figure 3.9 Optical Images of fabricated BP FET and Photodetectors (Device-1: Dual-Gate Polymer Electrolyte gated BP FET, thickness ~40 to 50 nm, channel length ~5 µm and channel width ~2 µm; Device-2: Polymer Electrolyte gated BP FET with orthogonal source-drain contacts, thickness

~50 nm, channel length ~10 µm and channel width ~5 µm; Device-3: Polymer Electrolyte gated BP Photodetector, thickness ~50 to 60 nm, channel length ~4 µm and channel width ~2 µm; Device-4: Dual-Gate Polymer Electrolyte gated BP Photodetector, thickness ~30 to 40 nm, channel length ~10 µm and channel width ~20 µm; Device-5: Dual-Gate Polymer Electrolyte gated BP Photodetector with interdigitated electrodes, thickness ~59nm, channel length ~25 µm and channel width ~12 µm; Device-6: Dual gate BP Photodetector to characterize full spectral response, thickness ~62 nm, channel length ~20 µm and channel width ~30 µm.

3.4.1 BP FET Characterization

The output and transfer characteristics of polymer electrolyte based dual-gate BP FET (device-1) is shown in Figure 3.10 to Figure 3.14. The approximate thickness of this device from the optical contrast is found to be ~ 40 to 50 nm. The output curve shown in Figure 3.10 shows a quasi linear relationship between the source-drain current (I_{DS}) vs source-drain voltage (V_{DS}) and thus indicates the type of conduction is an ohmic contact with BP but with some asymmetry in the drain current due to the different contact area of flake on both sides . Also as the gate voltage (V_{BG} or V_{TG}) is increased the transistor changes its state from ON to OFF as shown in Figure 3.11 and Figure 3.12. This indicates the intrinsic p-type nature of BP and the current modulation in the BP channel by bottom and top gates. But the interesting point is to observe the range of applied top gate bias which can achieve high current modulation as compared to the Si bottom gate bias. This can be attributed to the high capacitance at the BP-electrolyte interface.

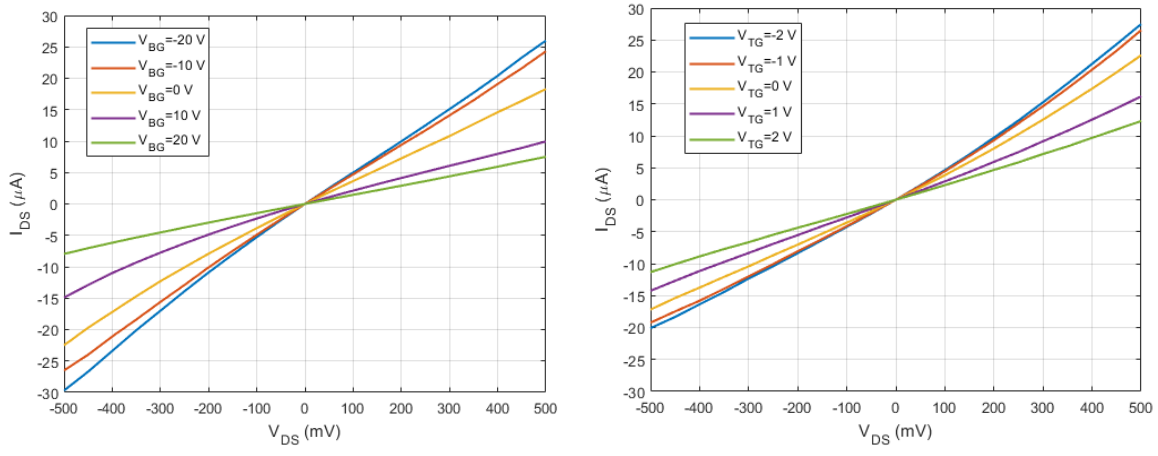

Figure 3.10 Output curves with bottom gate and top gate in glovebox (Device-1).

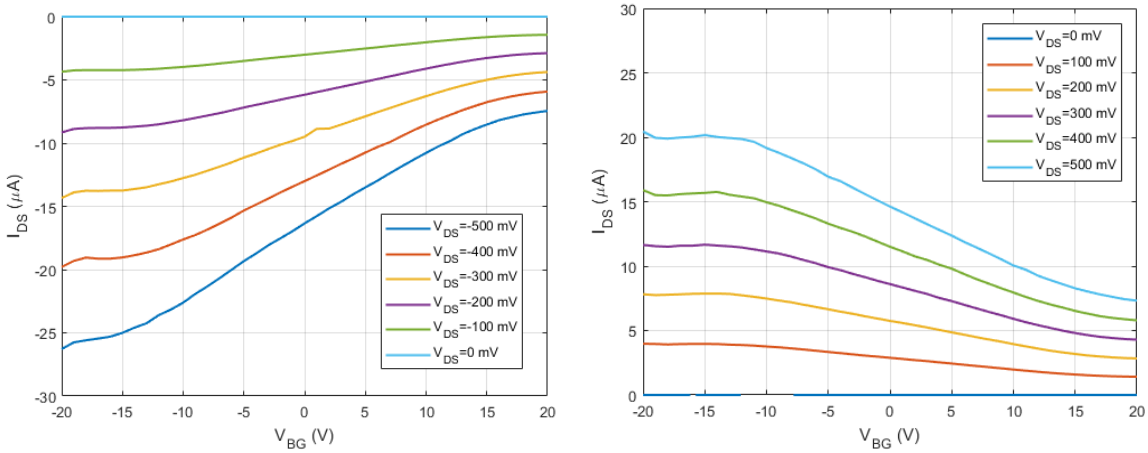

Figure 3.11 Transfer curves at different source-drain voltage V_{DS} with bottom gate in glovebox (Device-1).

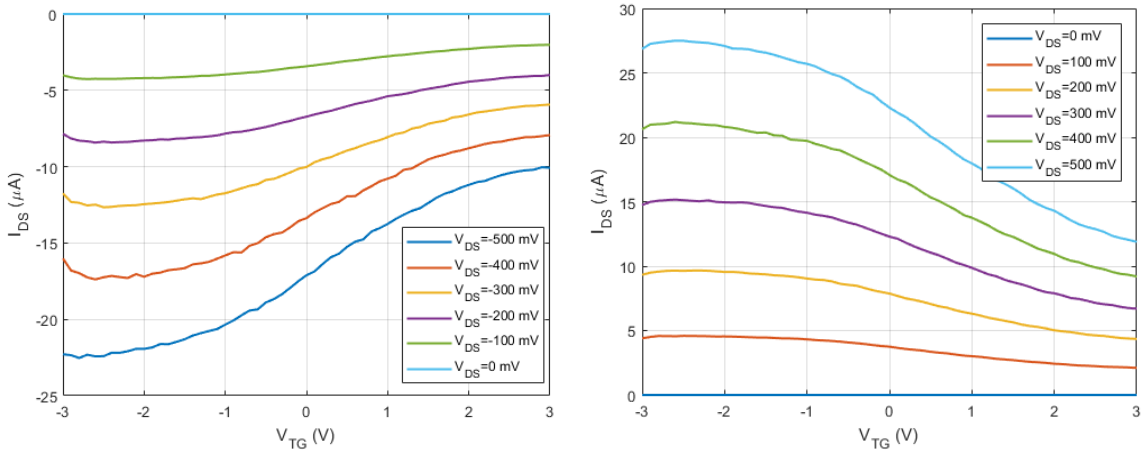

Figure 3.12 Transfer curves at different source-drain voltage V_{DS} with top gate in glovebox (Device-1).

The output and transfer characteristics are measured in glovebox and in ambient conditions for comparison. The output curves still show linear ohmic relation between current and source-drain voltage. However, the transfer curve in ambient conditions show significant distortion in the p-type behaviour of BP FET that arises from the modified BP surface oxidation effects since the flake was not protected with any encapsulation layer and it directly covered with the polymer film. Thus, to prevent BP degradation during the device measurements, we deposit a thin 3 nm Al layer after forming the contacts, and it forms a natural oxide layer.

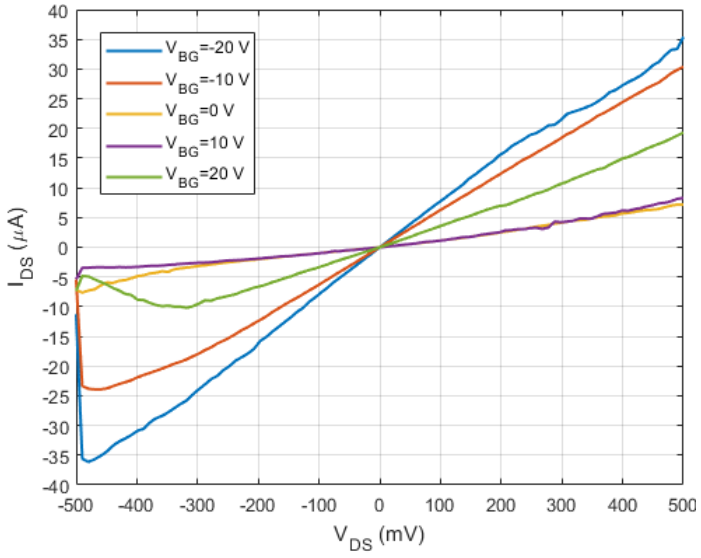

Figure 3.13 Output curve with bottom gate in ambient conditions (Device-1).

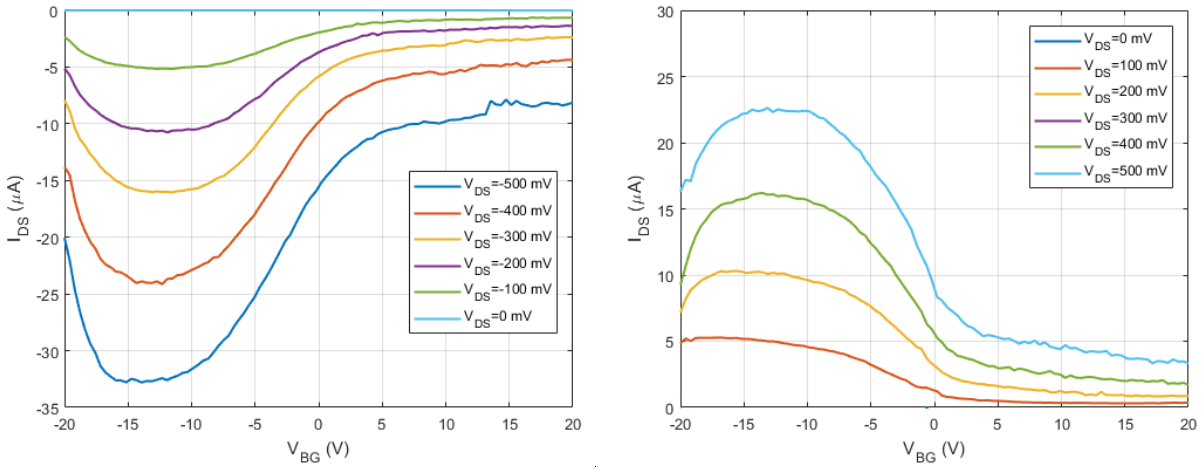

Figure 3.14 Transfer curves at different source-drain voltage V_{DS} with bottom gate in ambient conditions (Device-1).

Another configuration of BP FET is shown in Figure 3.9 (Device-2) is studied with orthogonal set of source-drain contacts which is approx. 50 nm thick. The electrical characteristics of this device are studied to demonstrate the anisotropic electrical properties of BP when used in FET configuration. This can be seen from the output curve shown in Figure 3.15 that indicates higher source-drain currents along the x-axis (AC) as compared to the ones oriented in y-axis (ZZ).

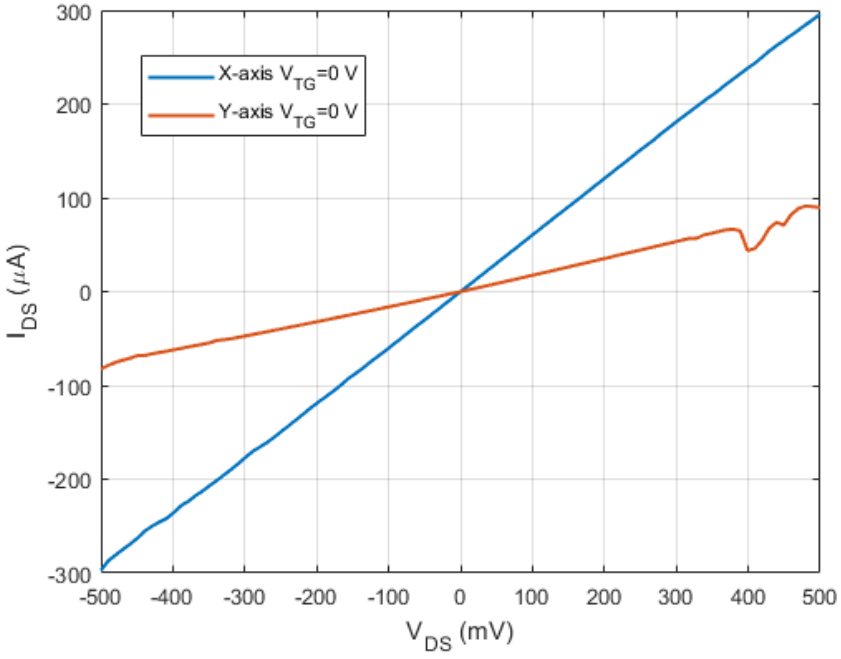

Figure 3.15 Output curve measured with x and y axis source-drain contacts (Device-2).

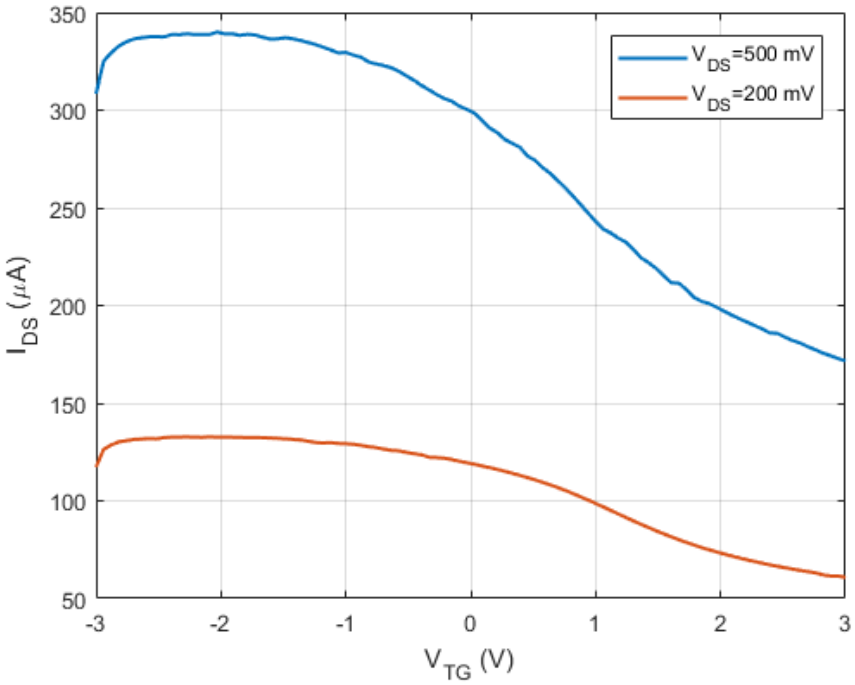

Figure 3.16 Transfer curve measured with x -axis source-drain contacts (Device-2).

3.4.2 Polymer top gate characterization

The polymer electrolyte PEO and $CsClO_4$ gated BP photodetector shown in Figure 3.9 (Device-3) with approximate thickness between 50-60 nm. The device is encapsulated with 3 nm thick Al_2O_3 layer. It is studied to characterize photocurrent and responsivities as a function of source-drain voltage, bottom gate, top gate and incident powers from 500 µW to 5 mW at excitation wavelength of 808 nm with a spot size of approx. 10 µm diameter. The output curve at different top gate voltages (V_{TG}) shown in Figure 3.17 indicates small increase in the source-drain current at negative top gate voltage resulting from high carrier densities in the channel.

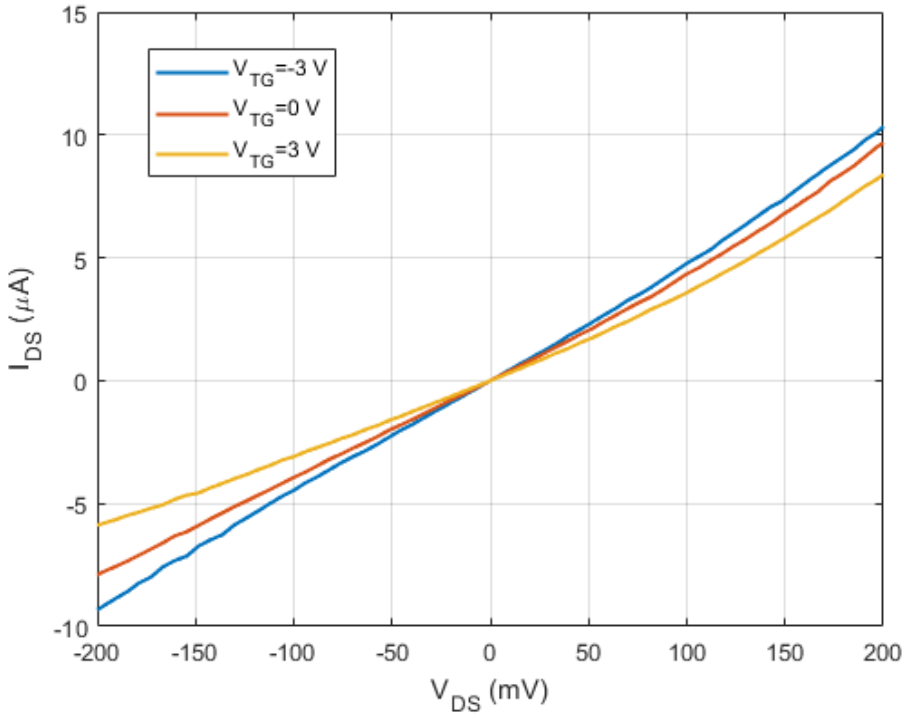

Figure 3.17 Output curve at different electrolyte top gate voltages V_{TG} (Device-3).

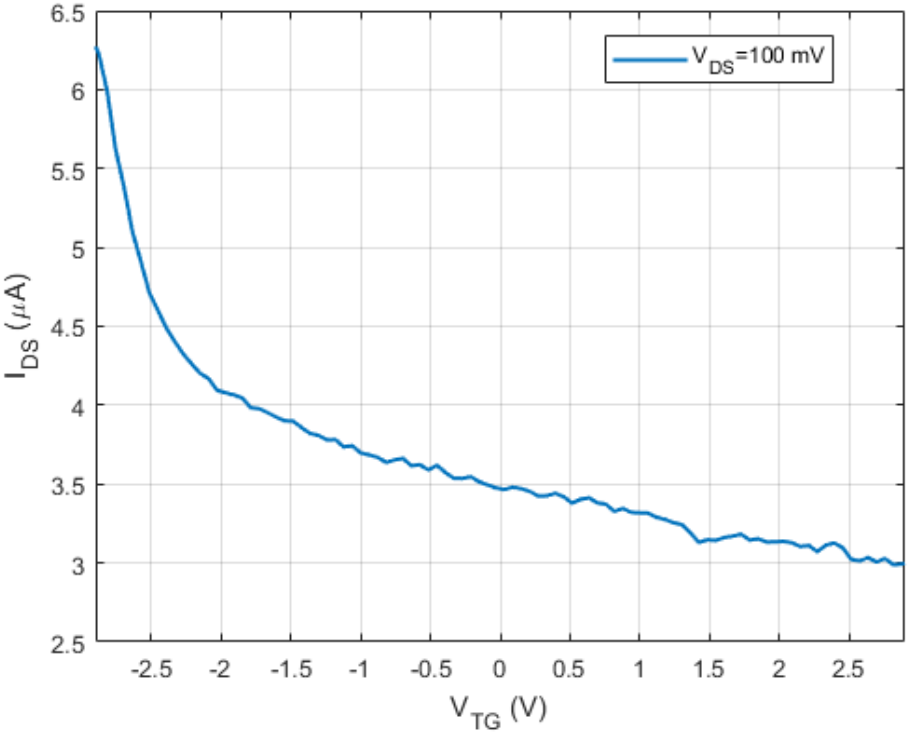

Figure 3.18 Transfer curve at V_{DS} =100 mV (Device-3).

3.4.3 Photocurrent measurements

The photocurrent which is measured as difference in the source-drain currents in light and in dark (I_p=I_{DS}(light)-I_{DS}(dark)) is shown at different V_{DS} and power levels for device-3. It is encapsulated with 3 nm thick Al_2O_3 layer. The photocurrent increases with V_{DS} and the incident powers resulting from the high densities of photogenerated electrons and holes in addition to the gradual filling of the trap states in the BP channel.

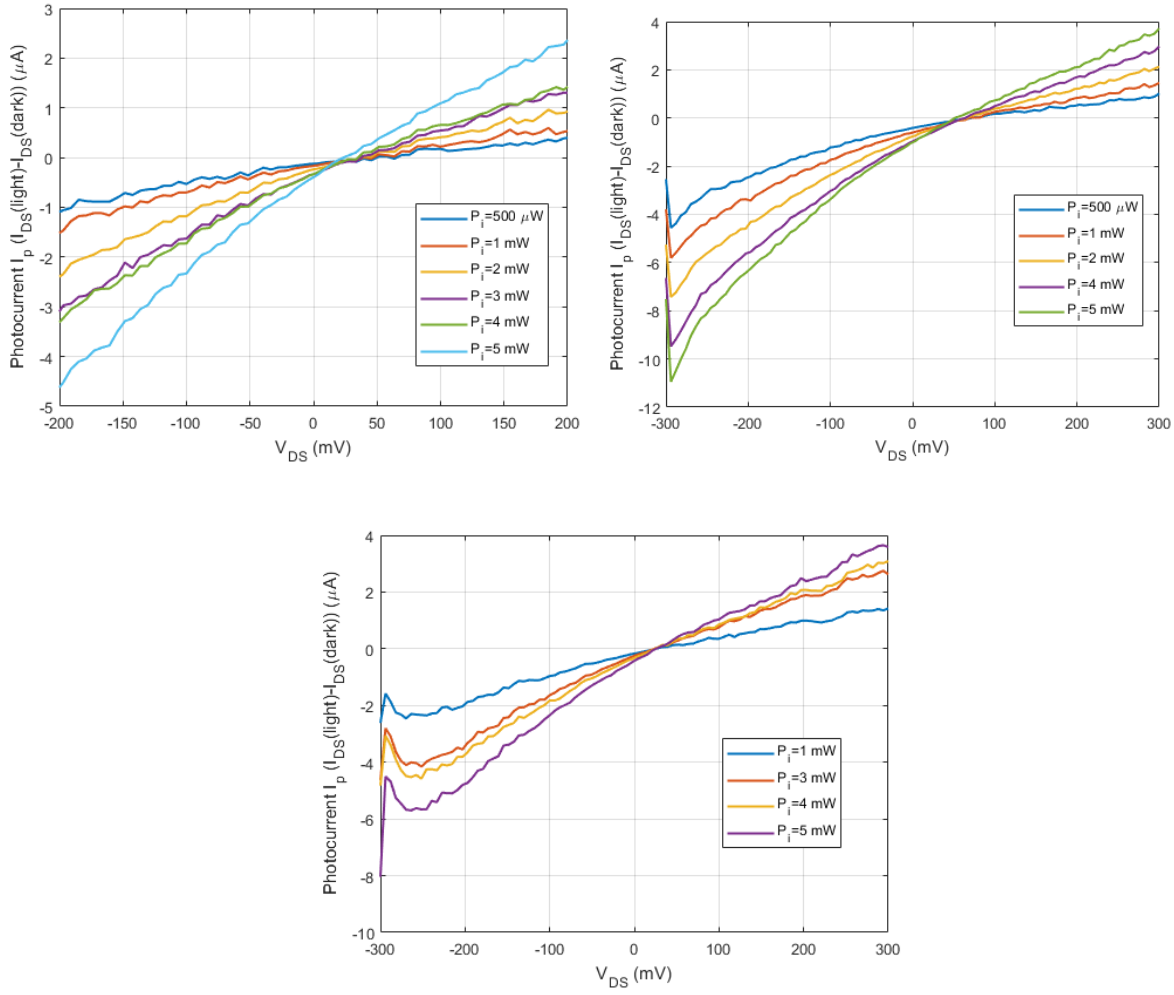

Figure 3.19 Photocurrent vs V_{DS} vs Incident Powers P_i a) V_{TG}=0 V, b) V_{TG}=3 V and c)V_{TG}=-3 V (λ=808 nm) (Device-3)

The responsivity curves at different excitation powers are summarized for increasing V_{DS} and V_{TG} values as shown in Figure 3.20 to Figure 3.22. Photocurrent modulation by a factor of four by incident powers as they are varied from 500 µW to 5 mW and factor of two by top-gate voltage as it is varied from 3V to -3V are obtained with the polymer electrolyte gated BP photodetector at 808 nm excitation wavelength.

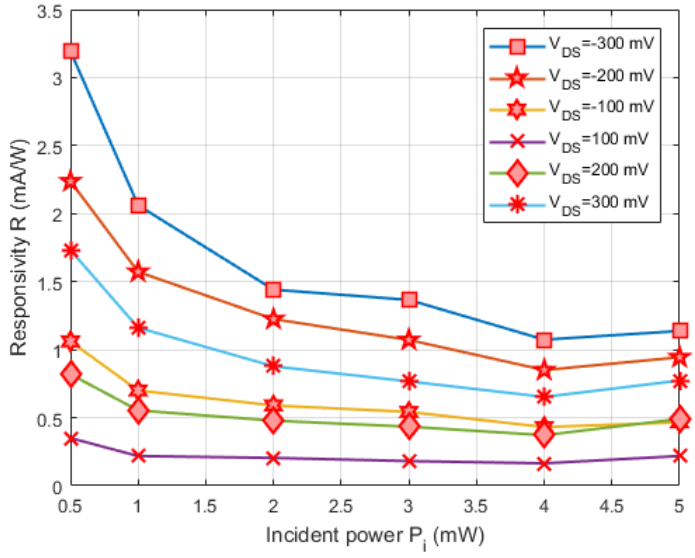

Figure 3.20 Responsivity vs P_i for V_{TG}=0 V for λ=808 nm (Device-3).

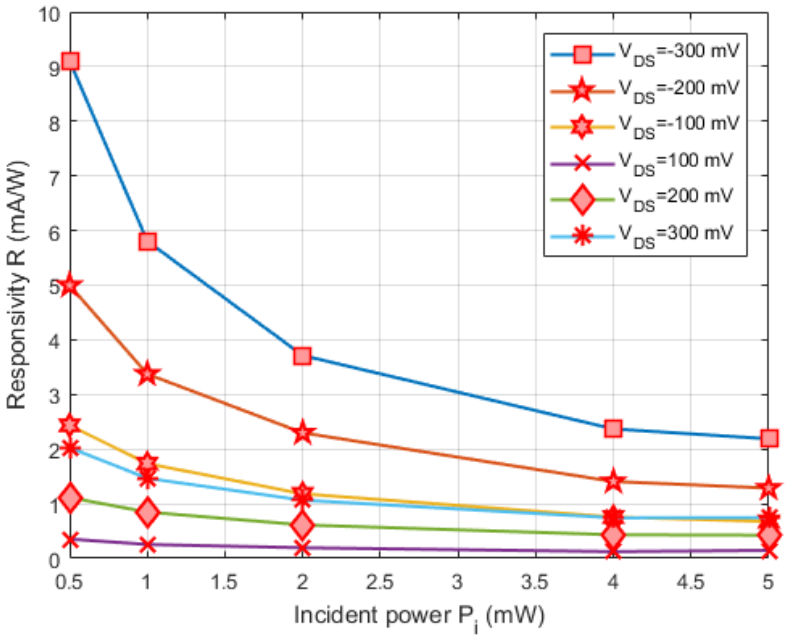

Figure 3.21 Responsivity vs P_i for V_{TG}=3 V for λ=808 nm (Device-3).

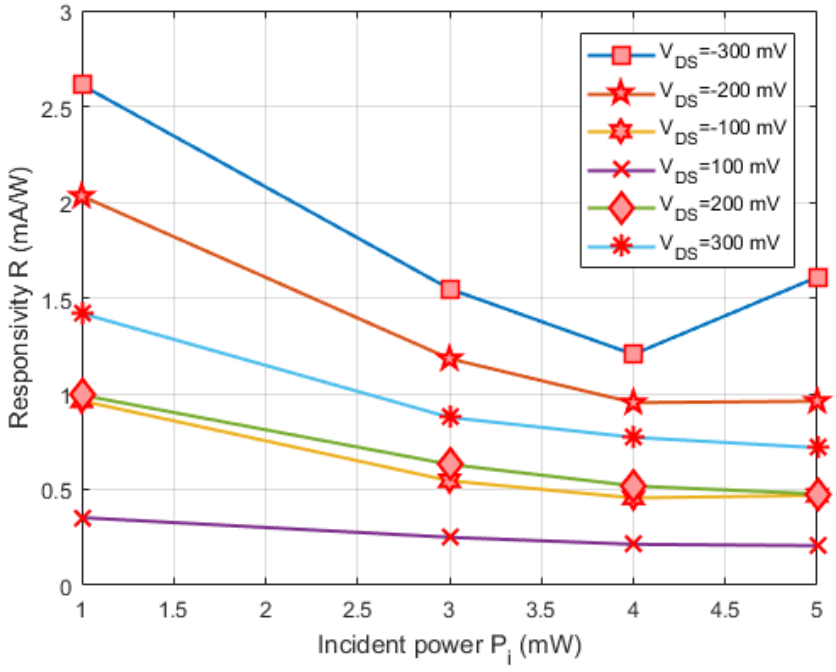

Figure 3.22 Responsivity vs P_i for V_{TG}=-3 V (λ=808 nm).

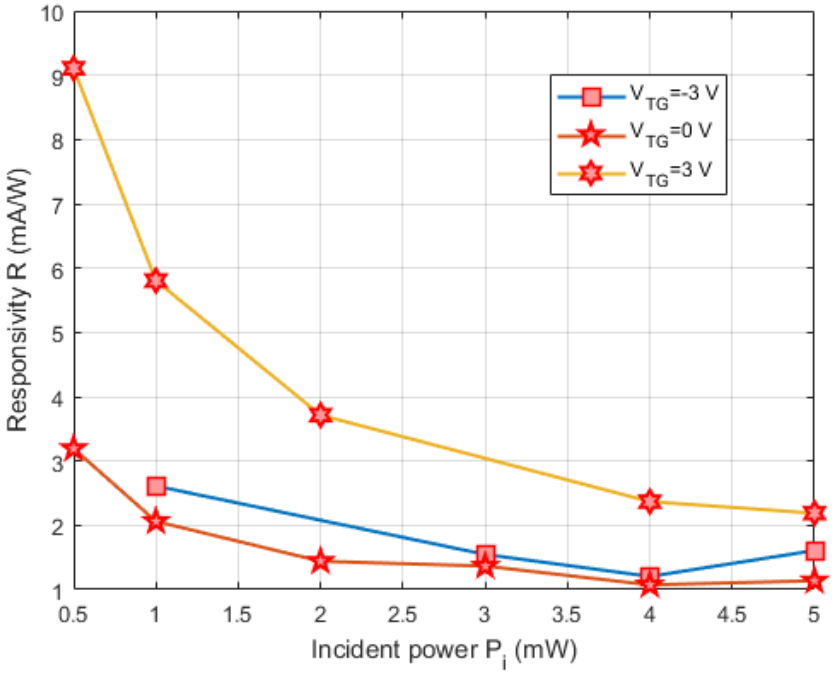

Figure 3.23 Responsivity vs P_i at different top gate voltages V_{TG} (λ=808 nm).

Thus, it can be summarized that the responsivities increase at low incident powers due to high photoconductive gain, however it becomes flat at higher powers where there is no gain. This behaviour is observed for both positive and negative top gate voltages.

3.4.4 Dual gate polymer electrolyte BP photodetector characterization

The comparison of the photodetector response with both top and bottom gates is then explained from the dual-gate polymer electrolyte BP photodetector (device-4) shown in Figure 3.9. This device is encapsulated with 3 nm Al_2O_3 layer. First, the output curves are compared with bottom and top gate voltages as shown in Figure 3.24. It can be seen from this figure that there are high number of charge carriers that result in high values of IDS with the electrolyte top gate bias V_{TG} as compared to the Si bottom gate voltage V_{BG}. It can also be elucidated from the transfer curve measured at V_{DS}=100 mV for both gates. The top gate provides a high ON/OFF ratio at low operating voltage range as compared to the bottom gate device. This high ON/OFF ration results from the 50-folds enhancement in the drain currents that as compared to the conventional silicon bottom gating.

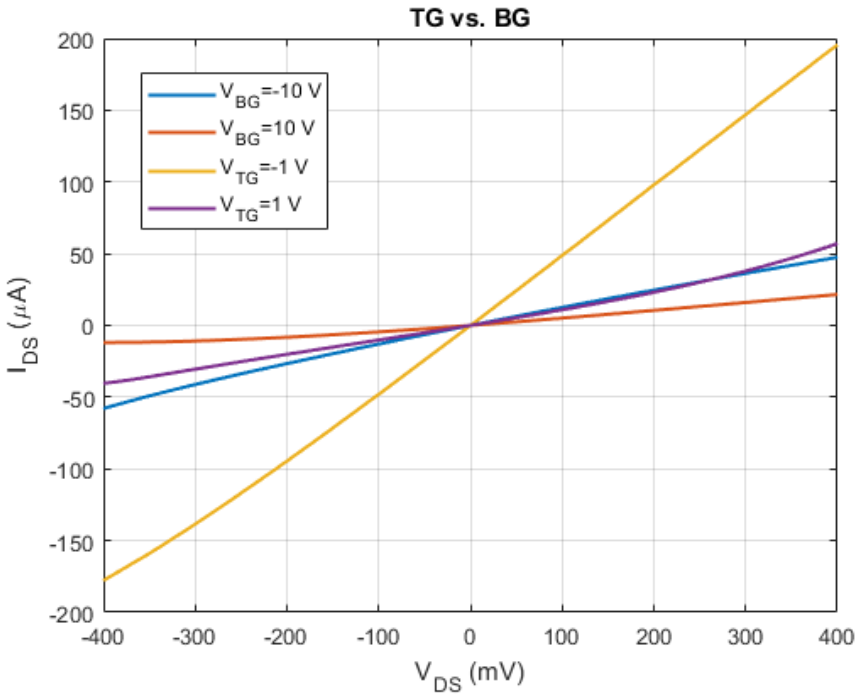

Figure 3.24 Output curve with electrolyte top gate vs silicon bottom gate (Device-4).

.

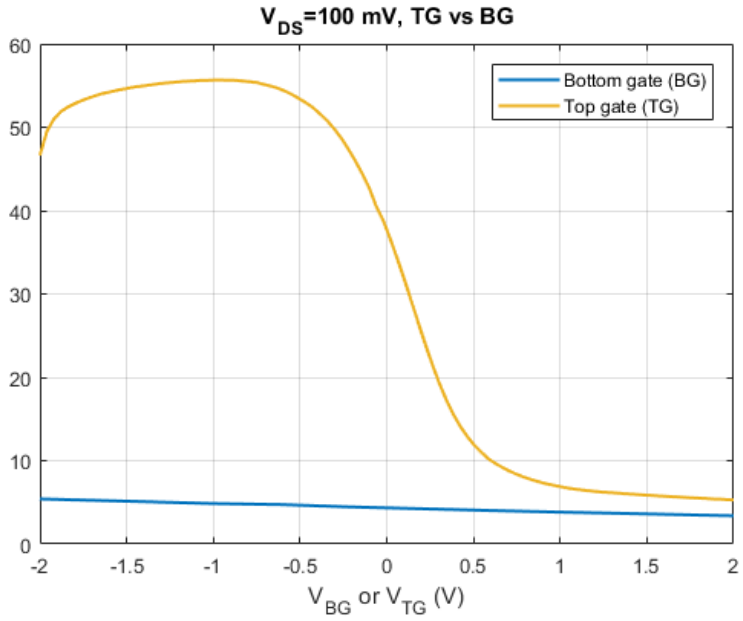

Figure 3.25 Transfer curve with electrolyte top gate vs Si bottom gate (Device-4).

The optical response of this device with both gates is also studied by measuring the photocurrents at different excitation wavelengths, source-drain voltage V_{DS} and gate voltages V_{BG} and V_{TG}. As discussed for the previous device, the photocurrent in this device follows a linear relation with the source-drain voltage V_{DS} and has high values of I_{DS} at negative gate bias for both gates as shown in Figure 3.26 and Figure 3.28. This behaviour of photocurrent is observed at both visible and near-infrared wavelengths. The dependence of photocurrent on gate bias for these wavelengths is also depicted in Figure 3.27 that indicates higher photocurrent in ON state of the device and it decreases as it reaches the OFF state.

The dual-gate polymer electrolyte based BP photodetector shows higher photocurrent enhancement ≈16 times with the electrolyte gate voltage tuned from -2 V to 2 V as compared to the bottom gate device which is ≈2.5 times with the gate voltage varied from -10 V to 10 V at the NIR wavelengths as shown in Figure 3.26 and Figure 3.28.

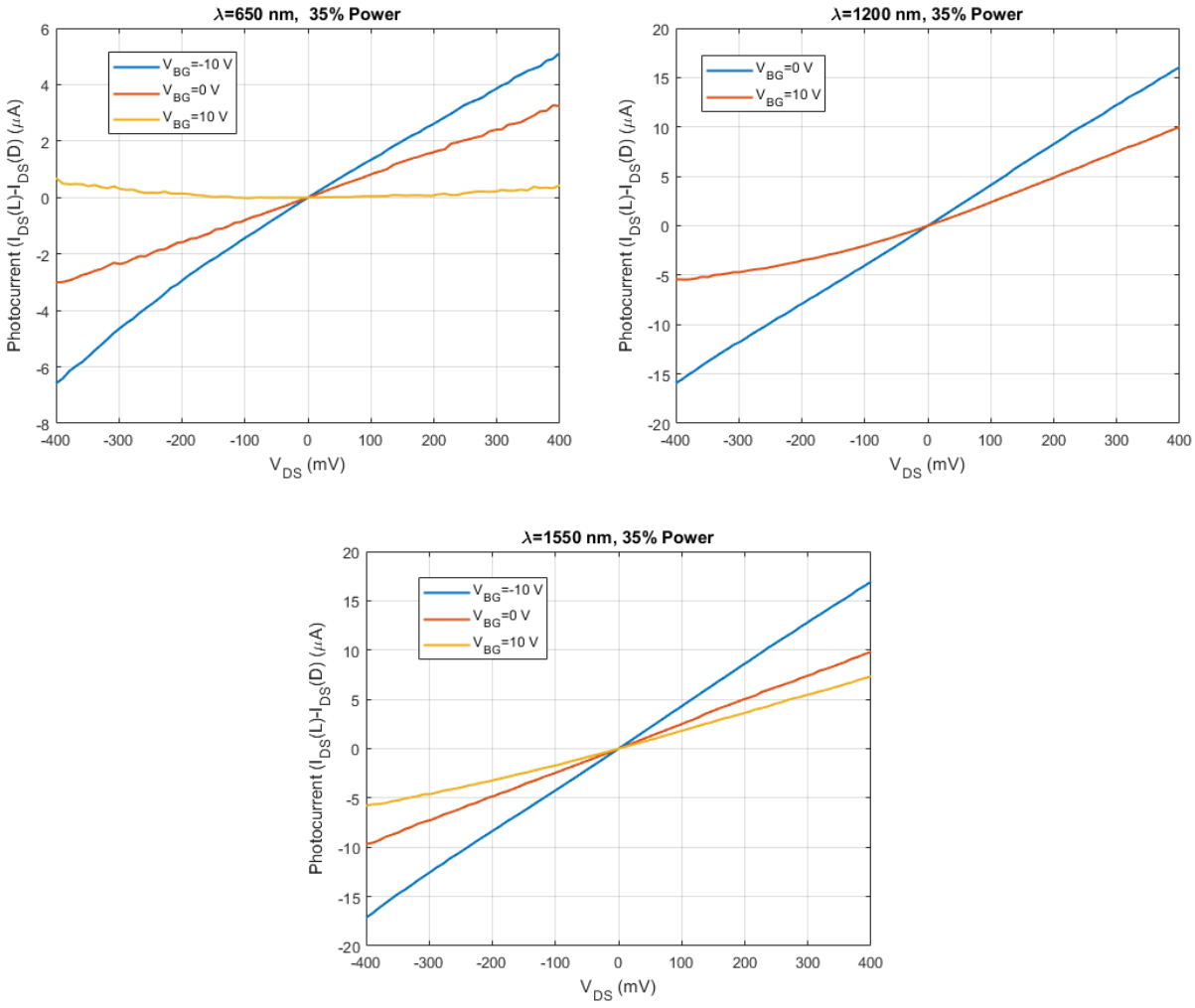

Figure 3.26 Photocurrent vs V_{DS} at different V_{BG} voltages a) λ=650 nm (P_i=0.4 μW) b) λ=1200 nm (P_i= 92 μW) and c) λ=1550 nm (P_i= 9.8 μW) (Device-4).

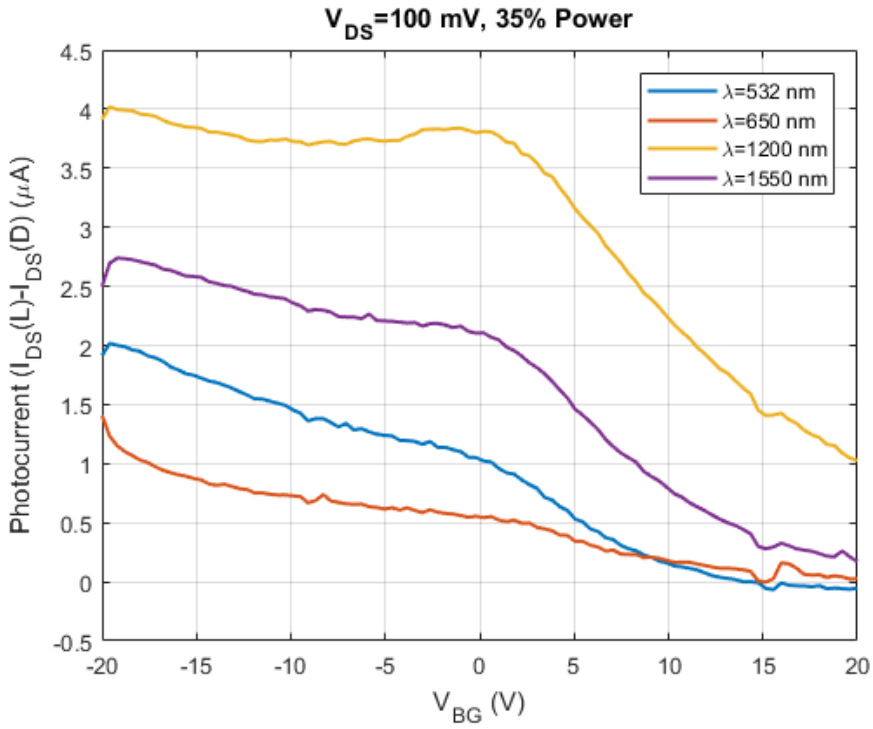

Figure 3.27 Photocurrent vs V_{BG} at visible and NIR wavelengths, V_{DS}=100 mV, (Device-4).

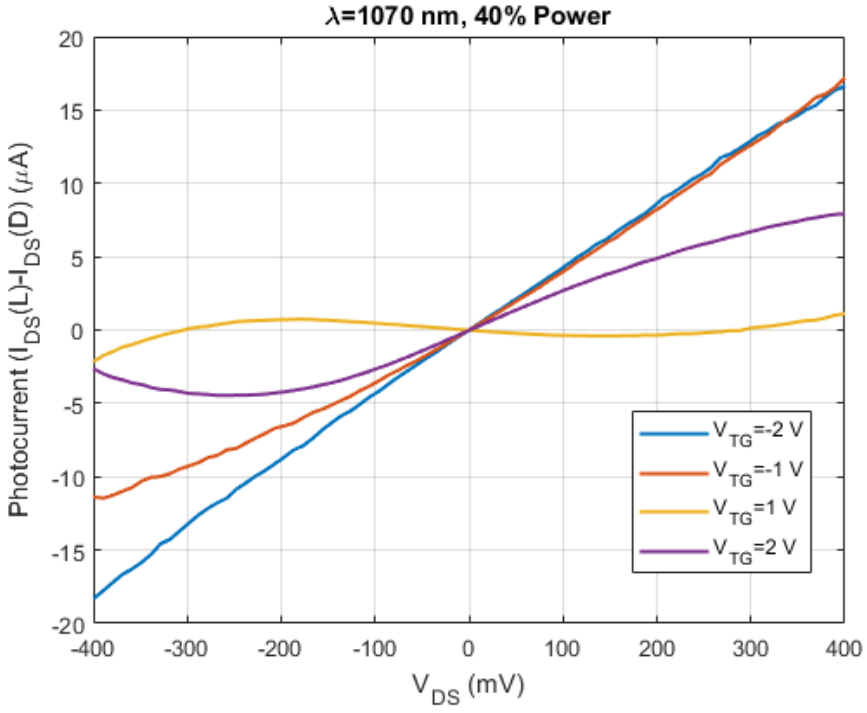

Figure 3.28 Photocurrent vs V_{DS} at different V_{TG} at λ=1070 nm (Device-4).

To sum up device-4 results, it can be summarized that the polymer electrolyte gating provides stronger photocurrent modulation than the Si bottom gating at NIR wavelengths. This is due to larger number of carriers the BP channel resulting from the high dielectric capacitance of the electrolyte film that also increases the number of photogenerated carriers. The photocurrent also decreases with gate voltage since both electron and hole traps are available for both photocarriers.

3.4.5 Spectral responsivity measurements

The full spectral response in the visible and NIR wavelengths is studied for the BP photodetector shown in Figure 3.9 (Device-5). The device is also encapsulated with 3 nm Al_2O_3 layer and it is fabricated to maximise photocurrent collection through interdigitated electrodes in the NIR region using a larger area BP flake. The AFM images of this device are shown in APPENDIX B and thickness was found to be ~59 nm.

The electrical characteristics of this device are measured for both gates and are shown in Figure 3.29 and Figure 3.30. The ON/OFF ratio for this device is found to be ~5 from the transfer curve in Figure 3.30. The tuning of charge carriers in the BP channel with the bottom gate and top gate can be seen through the output and transfer curves shown. It is obvious from previous measurements that the top gate provides higher modulation of charge carriers in the device as compared to the bottom gate device and this can be seen from the transfer curves shown in Figure 3.29 and Figure 3.30.

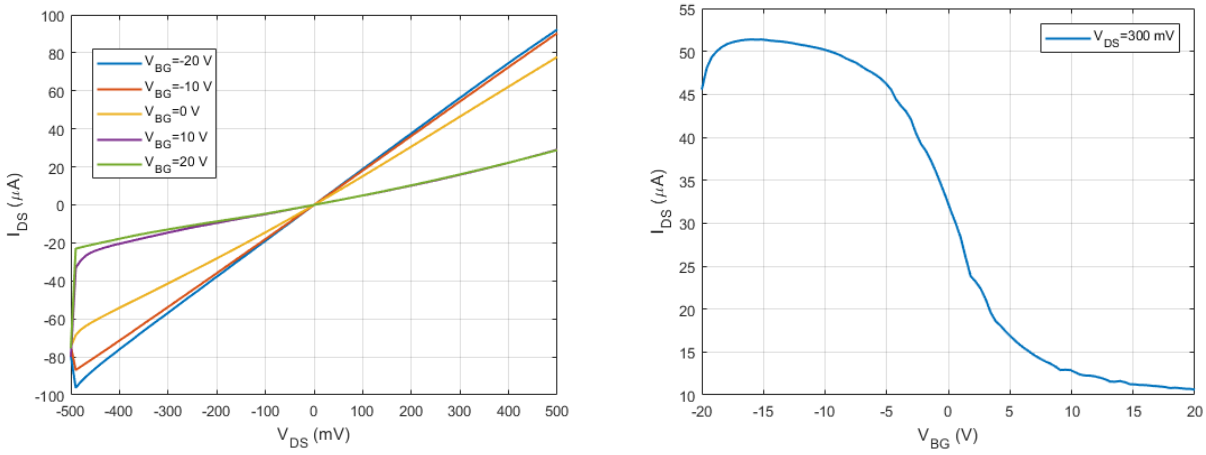

Figure 3.29 Output and transfer curves vs bottom gate (Device-5).

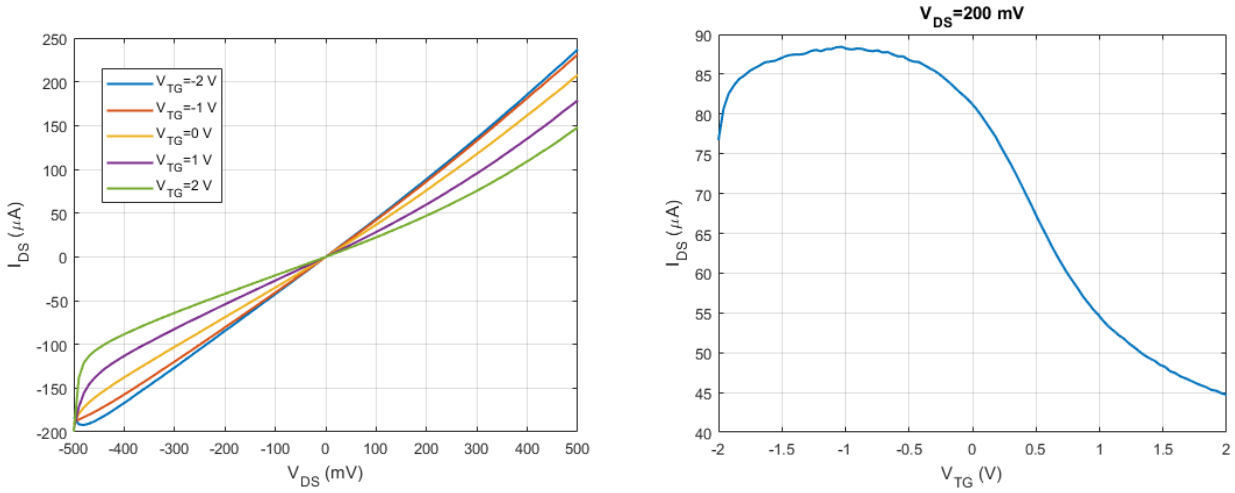

Figure 3.30 Output and transfer curves vs top gate (Device-5).

Next, the visible and NIR photoresponse of this device is studied. First, the visible photocurrent spectrum is measured using monochromatic excitation from supercontinuum laser which is swept from 350 nm to 1100 nm with the lock-in detection that lowers the noise signal when measuring the photoresponse over a broad range of wavelengths. The power dependent photocurrent spectra measured with this setup is shown in Figure 3.31. High photocurrent and responsivities can be observed with increasing power levels and it is maximum around 800 nm which has the maximum power as measured from the power spectrum (shown in the inset of Figure 3.31). The power spectrum of the source is measured with the Si photodiode and this is used to compute the responsivity of the devices.

Similarly, the NIR response of this device is measured at V_{DS}=300mV and V_{TG}=-2 V at various incident power levels as shown in Figure 3.33 and Figure 3.34 . The photocurrent is maximum at the peak power of the source and increases with the power levels. The NIR power spectrum of the source is measured using an InGaAs photodetector with lock-in detection. The NIR responsivities are then calculated by dividing the photocurrent and the incident power spectra. The responsivity tuning in the NIR spectra can also be observed from Figure 3.35.

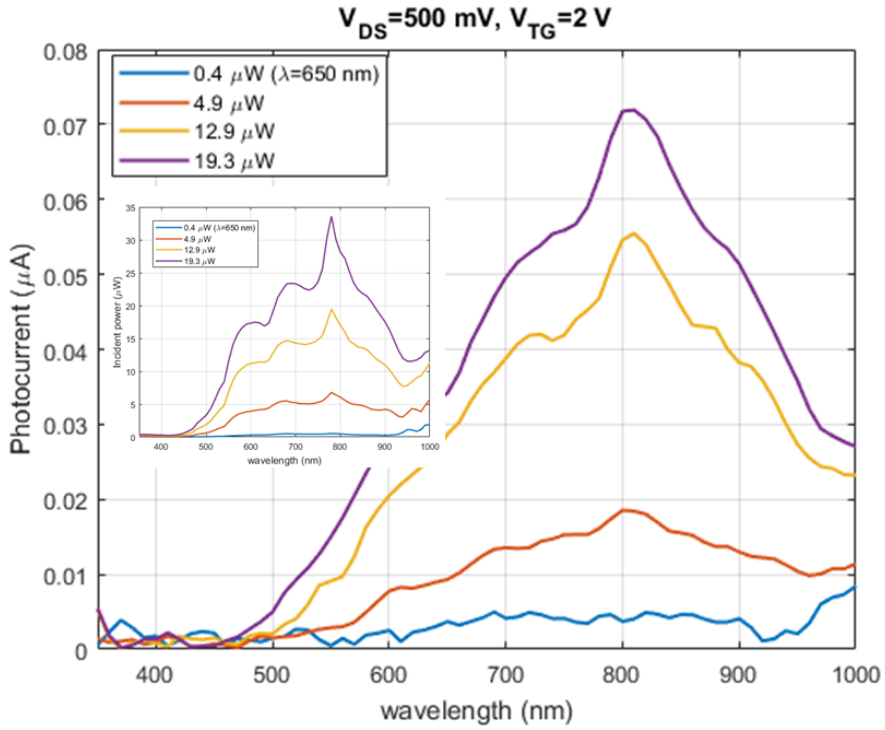

Figure 3.31 Visible Photocurrent spectra vs Incident Powers at V_{DS}=500 mV, V_{TG}=2 V;Inset shows Incident power spectra (Device-5)

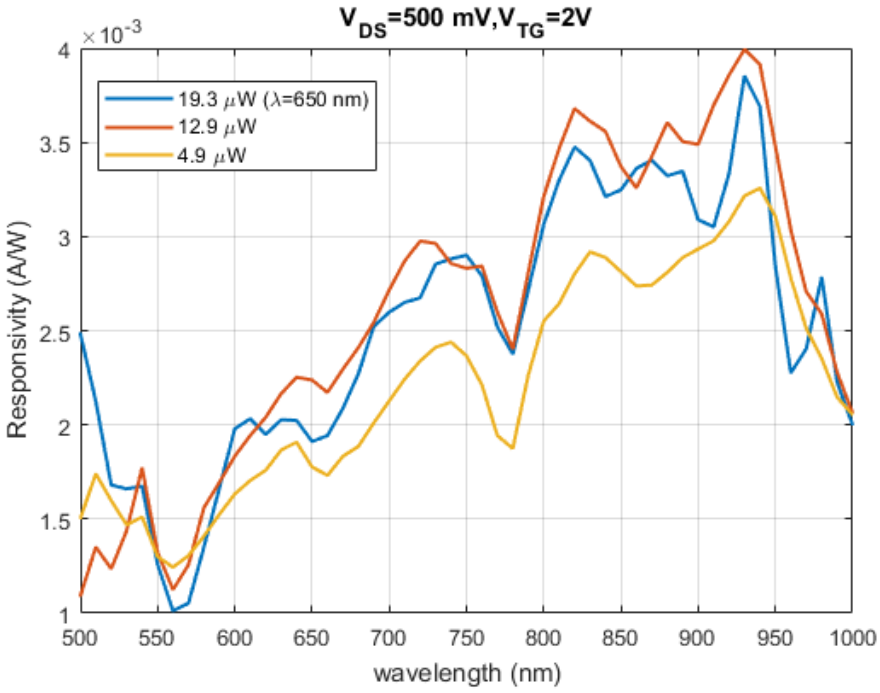

Figure 3.32 Visible Responsivity Spectra vs P_i at V_{DS}=500 mV, V_{TG}=2 V (Device-5).

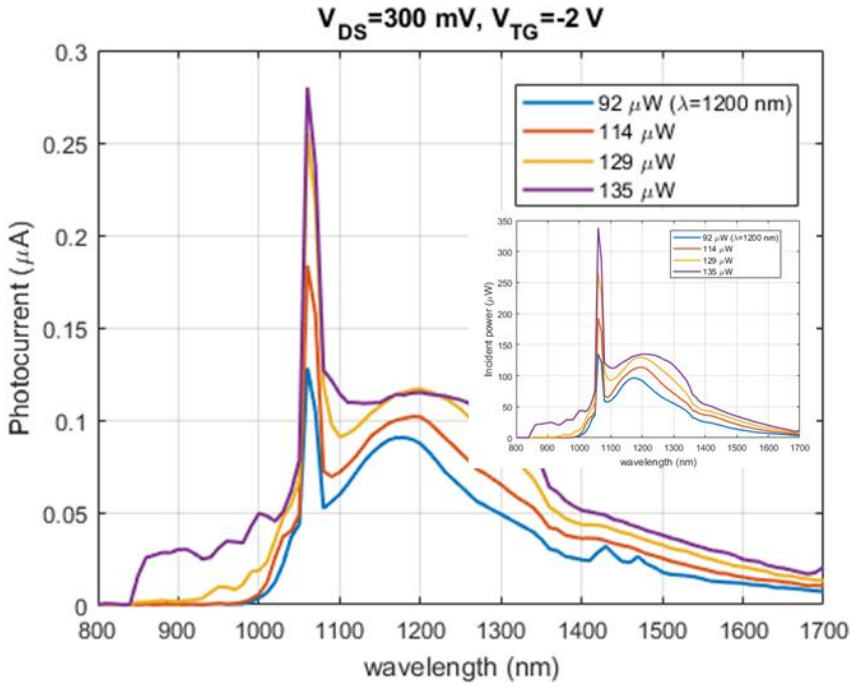

Figure 3.33 Near-Infrared Photocurrent spectra vs P_i at VDS=300 mV, VTG=2 V; Inset shows Incident NIR power spectra (Device-5).

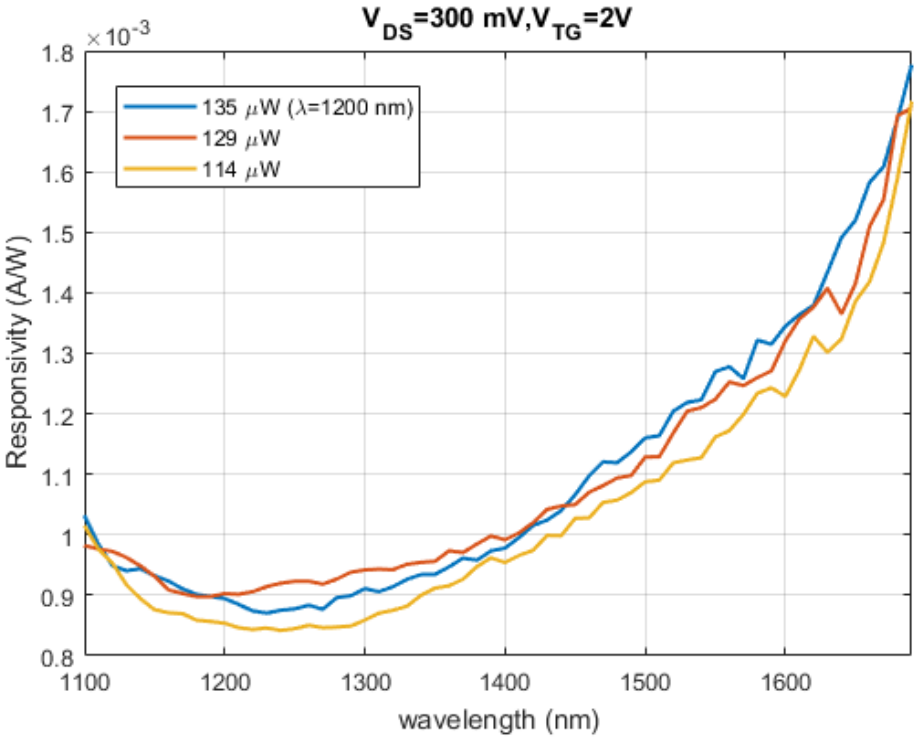

Figure 3.34 NIR Responsivity Spectra vs P_i at V_{DS}=300 mV, V_{TG}=2 V (Device-5).

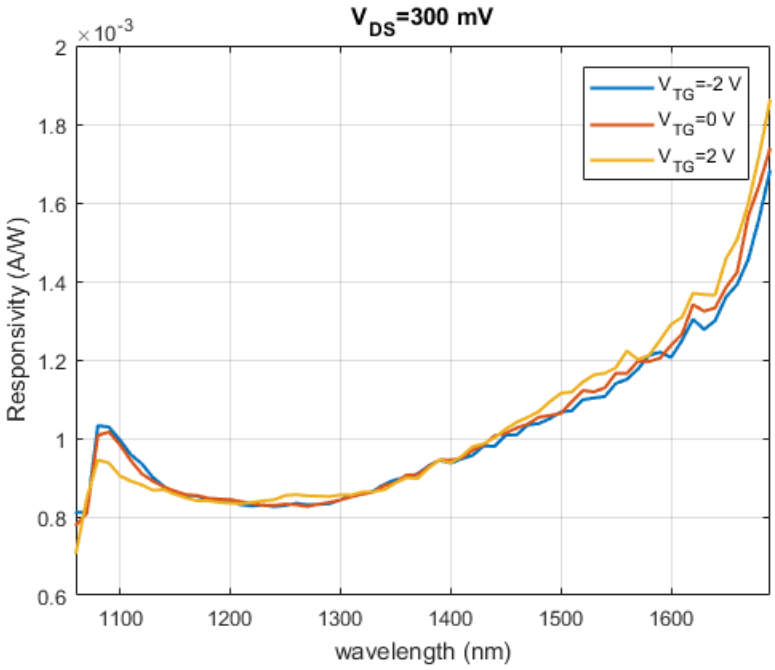

Figure 3.35 NIR Responsivity Spectra vs V_{TG} at V_{DS}=300 mV (Device-5).

In conclusion, device-5 shows carrier modulation with both gates as seen from the output and transfer curves. It also shows only a small change in the responsivity spectra with incident powers and gate voltage. This can be due to the presence of larger traps for both carriers coming from the thicker region of the BP flake.

The final BP device studied to characterize the full responsivity spectrum (visible and NIR upto BP bandgap i.e. 4 um) with supercontinuum and FTIR setup is shown in Figure 3.9 (Device-6). A larger BP flake of approx. 300 um^2 surface area is used to fabricate this device and it is also encapsulated with a 3 nm Al_2O_3 layer.

The AFM images of flake near the left edge of the device is shown in APPENDIX B. The thickness of this flake was found to be ~62 nm from this measurement. The output and transfer curves for this device are shown in to Figure 3.36 to Figure 3.39 with both top and bottom gates. High ON/OFF ratio of ~20 is obtained for this device as compared to previous devices due to the improved metal-BP contact and uniform flake density. The gate dependent carrier transport can be observed for both gates from the I_{DS} measured across the BP channel. It is evident from the transfer curve as more negative gate voltages are applied, accumulation occurs as the negative charge on gate attracts holes from the p-type substrate to the SiO_2-BP interface. As the gate voltage increases,

the device turns OFF as it moves to inversion mode where the large number of negative charges build up at the SiO_2-BP interface resulting from the minority carriers.

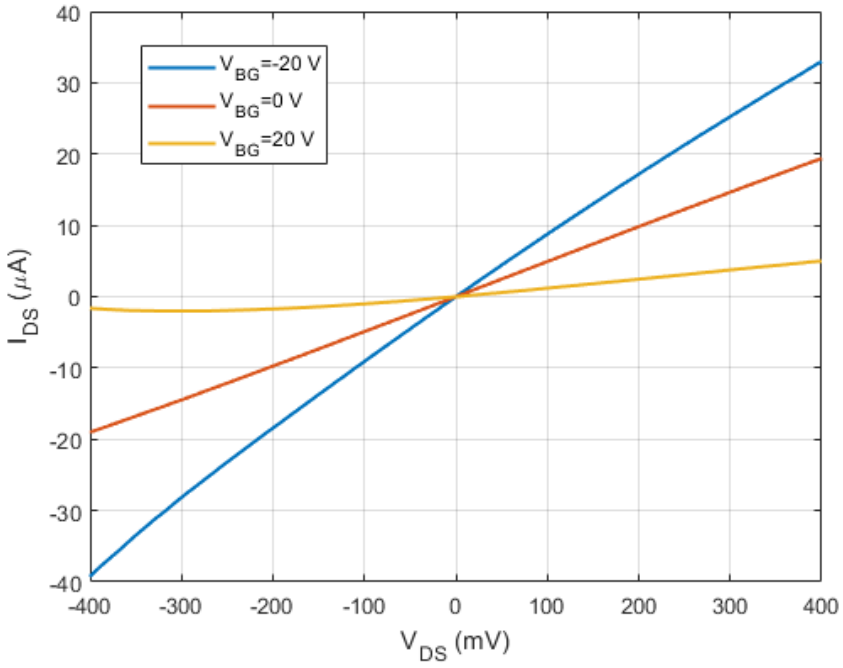

Figure 3.36 Output curve vs V_{BG} (Device-6).

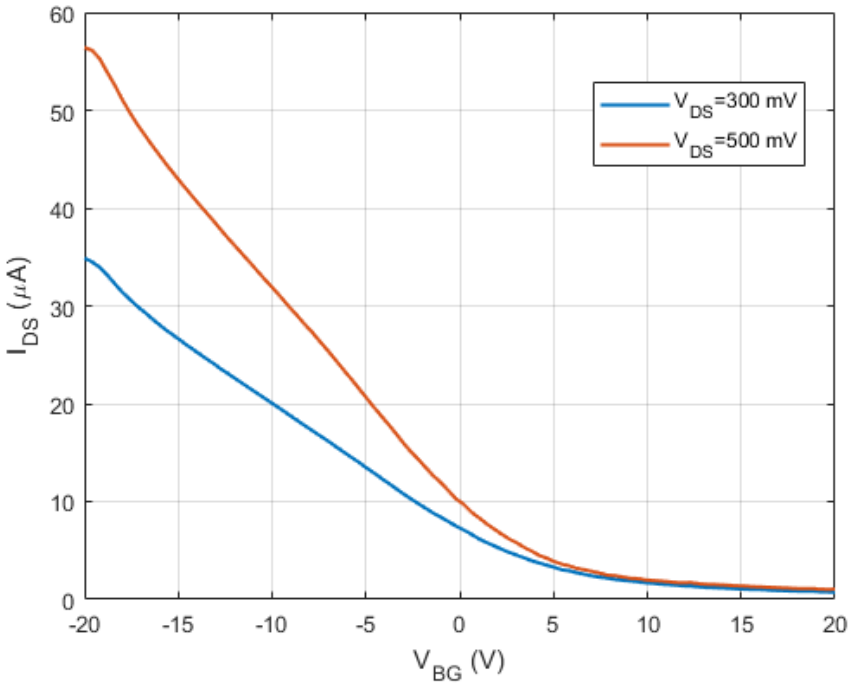

Figure 3.37 Transfer curve vs V_{DS} (Device-6).

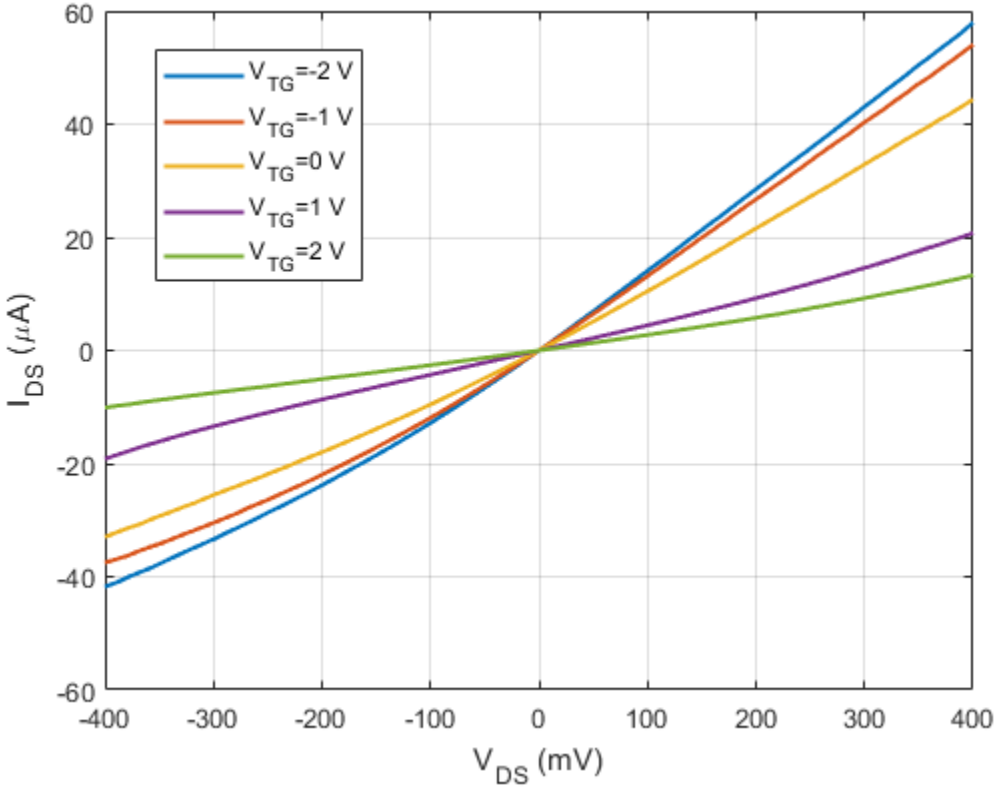

Figure 3.38 Output curves of Device-6 at different V_{TG}.

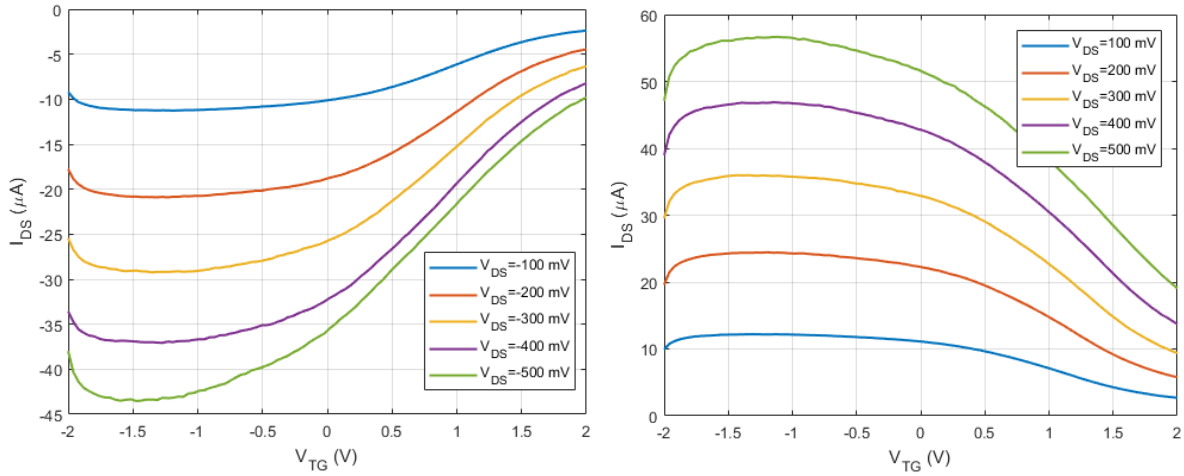

(a) (b)

Figure 3.39 Transfer curves of Device-6 with top gate for (a) Negative V_{DS} (b) Positive V_{DS} .

The visible and NIR photocurrent and responsivity spectra are then measured to study the gate dependence on the photoresponse of this device. The full photoresponse spectra upto 1.7 um are measured with the Fianium supercontinuum-monochromator setup whereas the extended NIR spectra above 1.7 um are measured with the NIR source of FTIR setup. All the measurements are performed with lock-in detection at a chopping frequency of 500 Hz.

The gate voltage dependent visible photocurrent and responsivity spectra for this device is shown in Figure 3.40 and Figure 3.41. At negative gate voltage, higher photocurrents are observed for the entire wavelength range that results from the large number of photogenerated carriers available for photocurrent generation at negative bias. However, as the gate voltage increases, the BP channel is depleted of charge carriers and therefore this leads to reduction in the photocurrent. The power dependent photocurrent and responsivity are also measured as shown in Figure 3.42 and Figure 3.43. It is obvious that the photocurrent increases with increasing incident powers over the entire wavelength range that is attributed to gradual filling of trap states that leads to large number of photogenerated carriers available for photocurrent. Also, photoconductive gain can be observed at low incident powers for the visible region since the responsivity increases as seen in Figure 3.43.

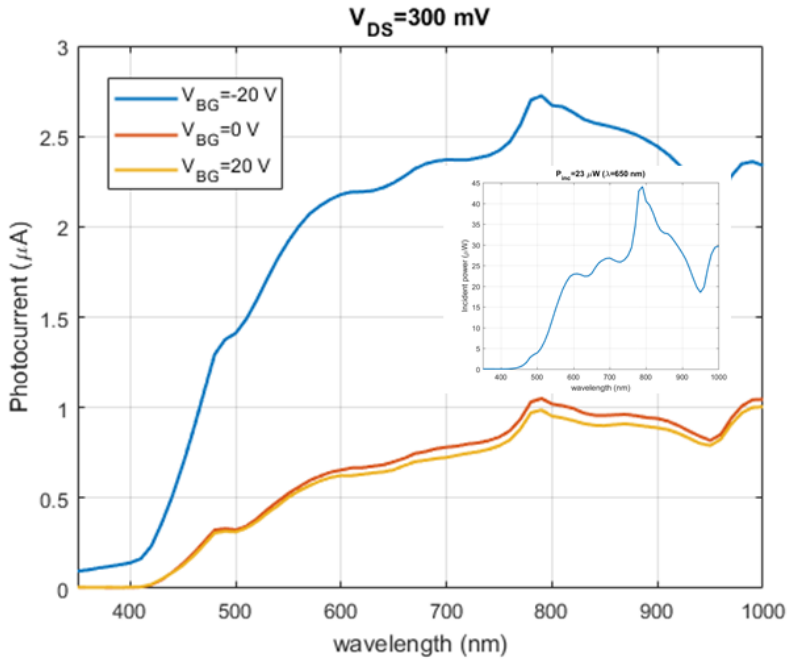

Figure 3.40 Visible Photocurrent spectra at different V_{BG} at V_{DS}=300 mV; Inset shows Incident power spectra (Device-6).

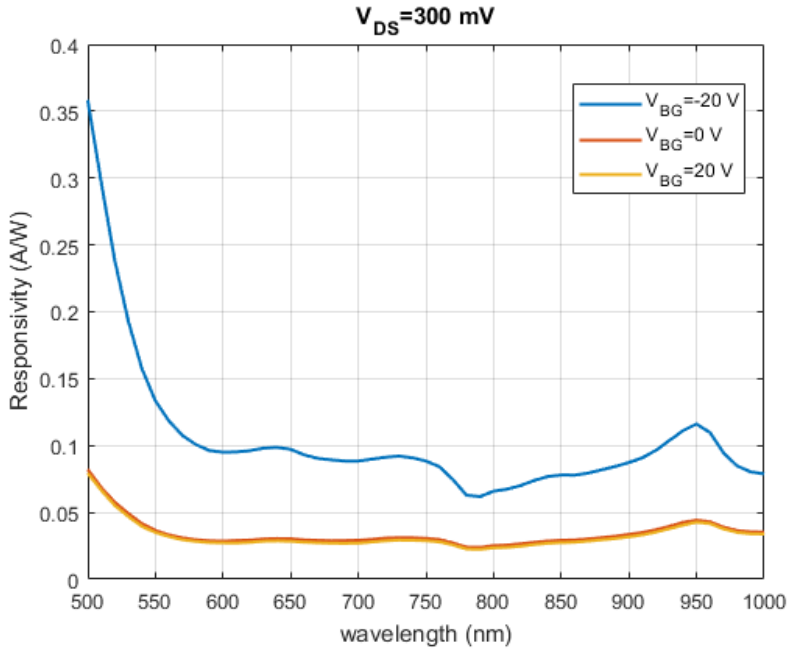

Figure 3.41 Visible Responsivity Spectra at different V_{BG} at V_{DS}=300 mV (Device-6).

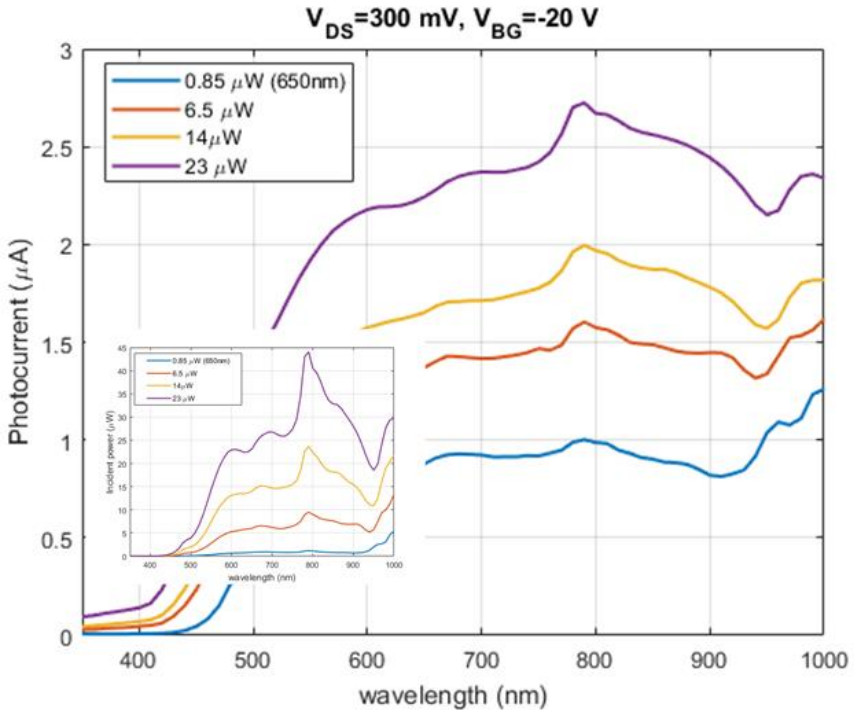

Figure 3.42 Visible Photocurrent spectra at different incident powers at V_{DS}=300 mV, V_{BG}=-20 V; Inset shows Incident power spectra (Device-6).

Similarly, the gate-dependent and power-dependent NIR photocurrent and responsivity spectra with supercontinuum source monochromatic excitation is shown in Figure 3.44 to Figure 3.47. In consistent with the visible photocurrent spectra, the NIR measurements also show similar behaviour with the applied gate bias. It can also be seen that the photocurrent and responsivities are also modulated by the incident powers, they both increase with the incident powers.

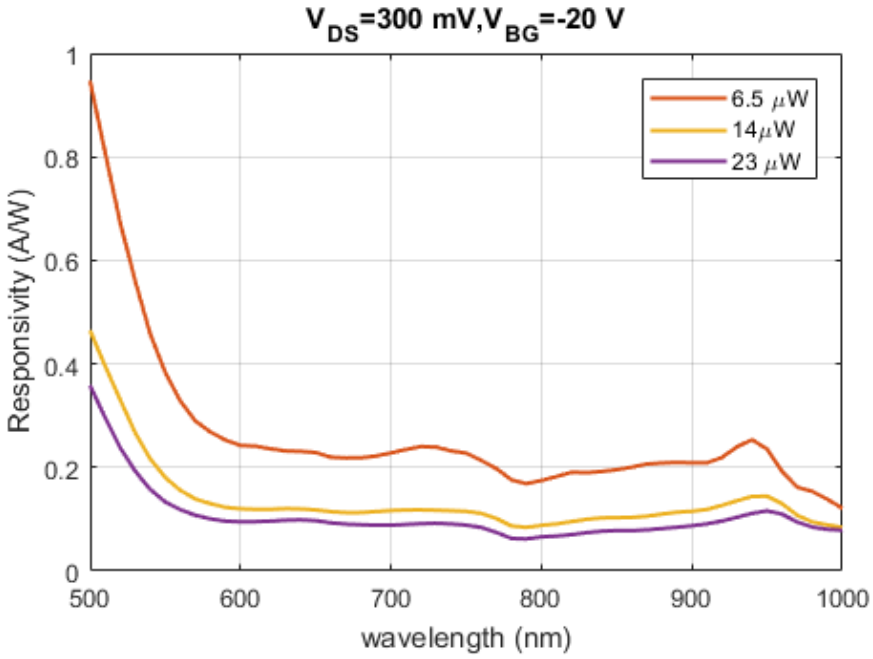

Figure 3.43 Visible Responsivity Spectra at different incident powers at V_{DS}=300 mV, V_{BG}=-20 V (Device-6).

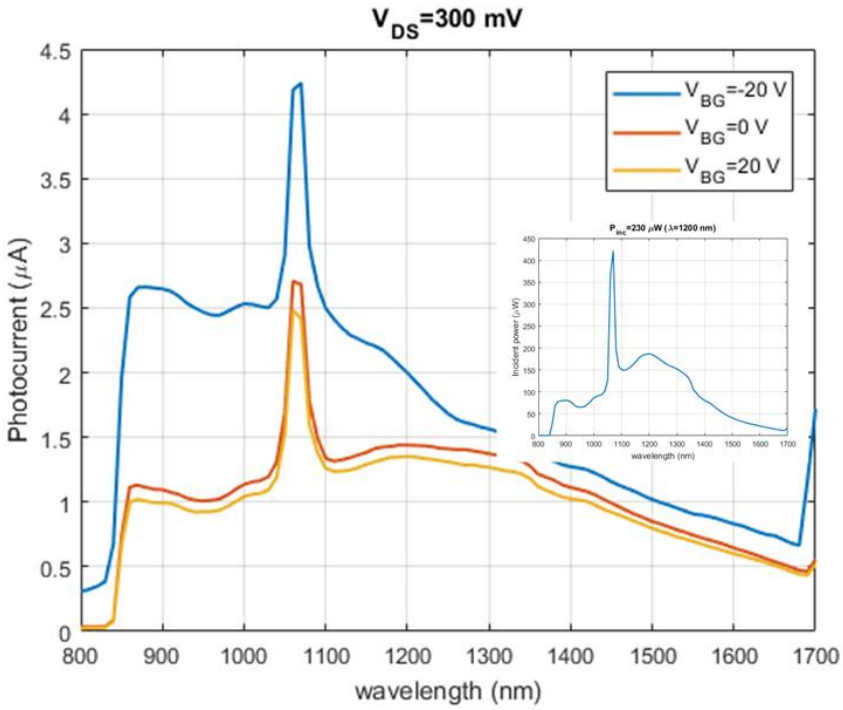

Figure 3.44 NIR Photocurrent spectra at different V_{BG} at V_{DS}=300 mV; Inset shows Incident NIR power spectra (Device-6).

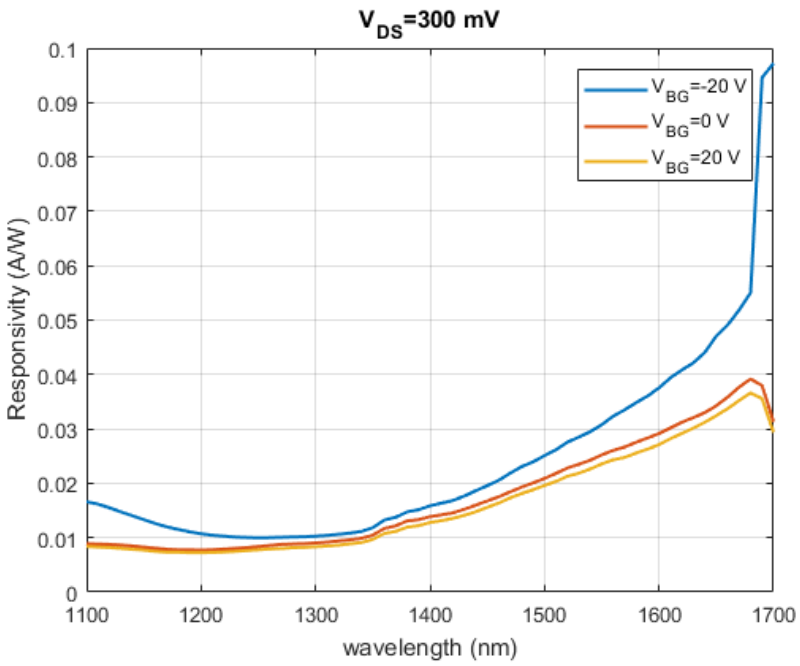

Figure 3.45 NIR Responsivity Spectra at different V_{BG} at V_{DS}=300 mV (Device-6).

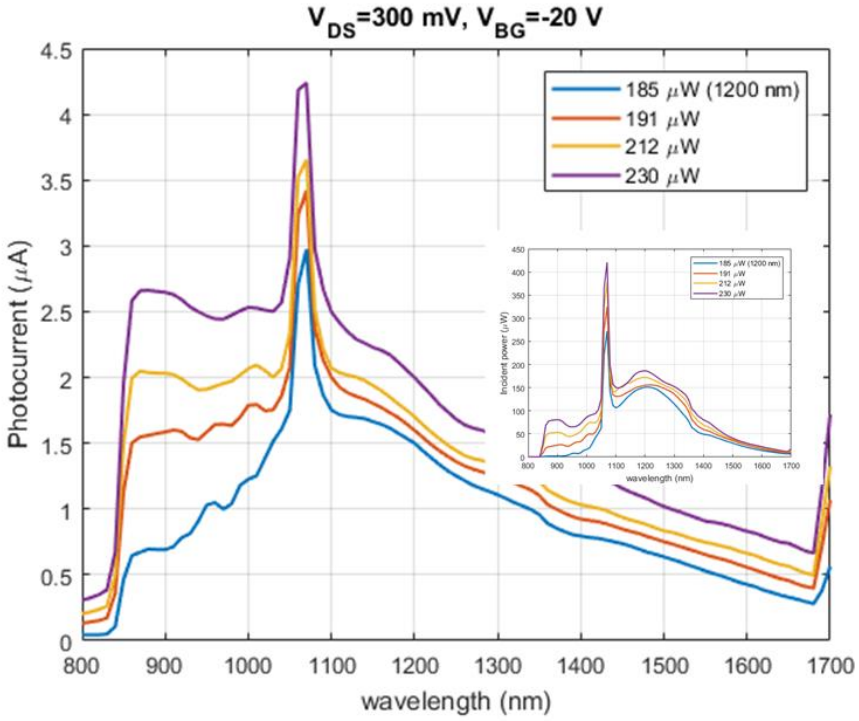

Figure 3.46 NIR photocurrent spectra at different incident powers for V_{DS}=300 mV, V_{BG}=-20 V; Inset shows incident NIR power spectra(Device-6).

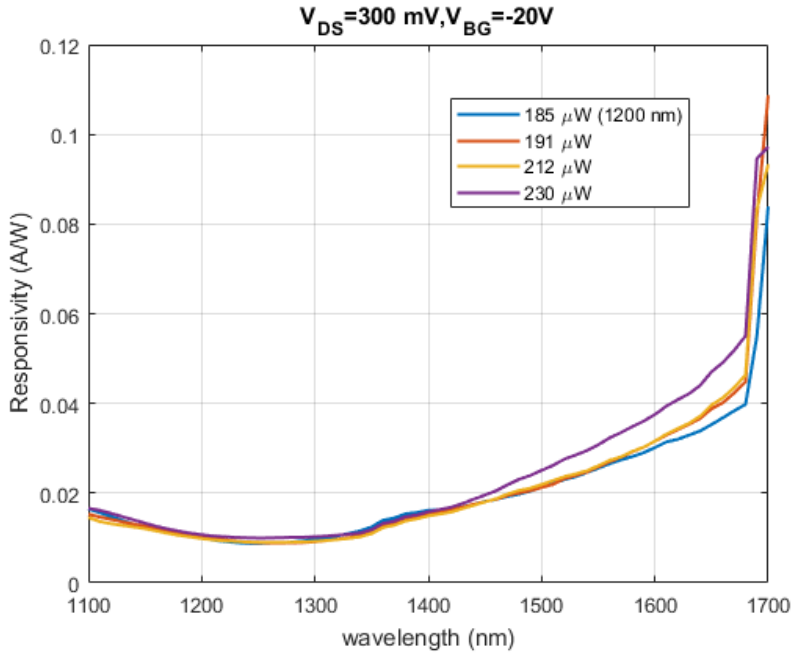

Figure 3.47 NIR Responsivity Spectra at different incident powers for V_{DS}=300 mV, V_{BG}=-20 V; Inset shows incident NIR power spectra(Device-6).

Next, the infrared measurements are performed with the internal NIR broadband tungsten source of FTIR with lock-in detection. First, the power profiles of the incident light sources is measured using a continuous step scan measurement mode with the OPUS software of FTIR (APPENDIX F). The variation of incident power spectral intensities to study the power dependent photoresponse in these wavelength ranges can be studied using different internal aperture sizes of the FTIR setup. This can be seen from the power profiles of the internal NIR (1-10 μm) and MIR (1-30 μm) that gives higher power intensities at larger apertures.

The photoresponse of the detectors using this setup is therefore measured using a step-scan measurement program with lock-in detection and it is first verified by measuring the response of the calibrated InGaAs detector at different apertures, (FGA01, Thorlabs) that has peak detection wavelength around 1550 nm as shown in APPENDIX G.

Finally, the infrared responsivity measurements of the BP device-6 are measured at different excitation intensities and gate voltages as depicted in Figure 3.48 and Figure 3.49. The relative responsivities are computed by dividing the FTIR photoresponse of the device with the power profiles measured using DLaTGS detector. Figure 3.48 shows that the relative responsivities increase with incident powers for the higher infrared wavelengths and the detection cut-off peak is around 4 μm that is close to the bulk BP bandgap. Similarly, the gate-dependent responsivities shown in Figure 3.49 demonstrate increase in the infrared responsivities with negative gate voltages that corresponds to the accumulation mode of the device which increases the number of electrons and holes inside the BP channel required to produce photocurrent.

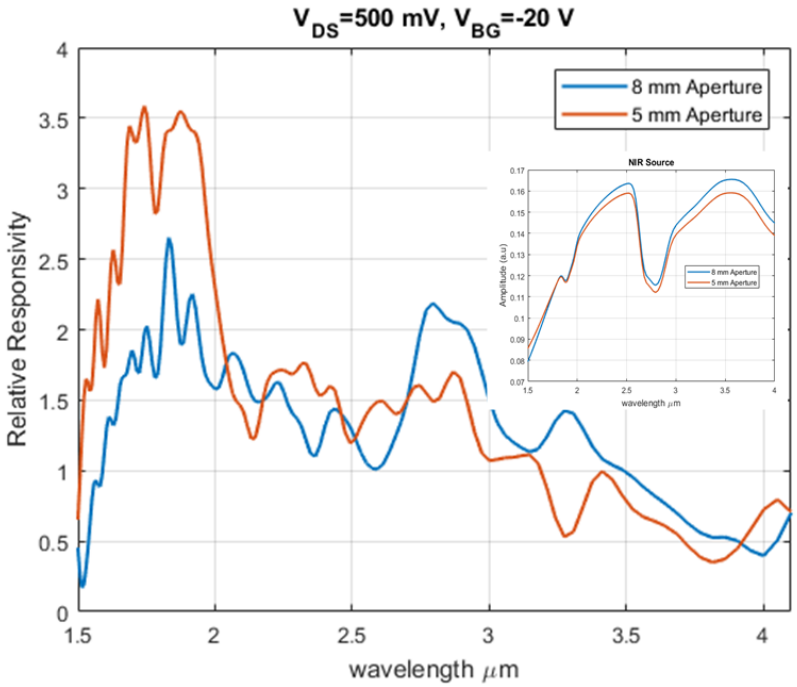

Figure 3.48 Relative Responsivity at different incident power levels measured with FTIR NIR source; Inset: Power profile of NIR source at different aperutres (Device-6).

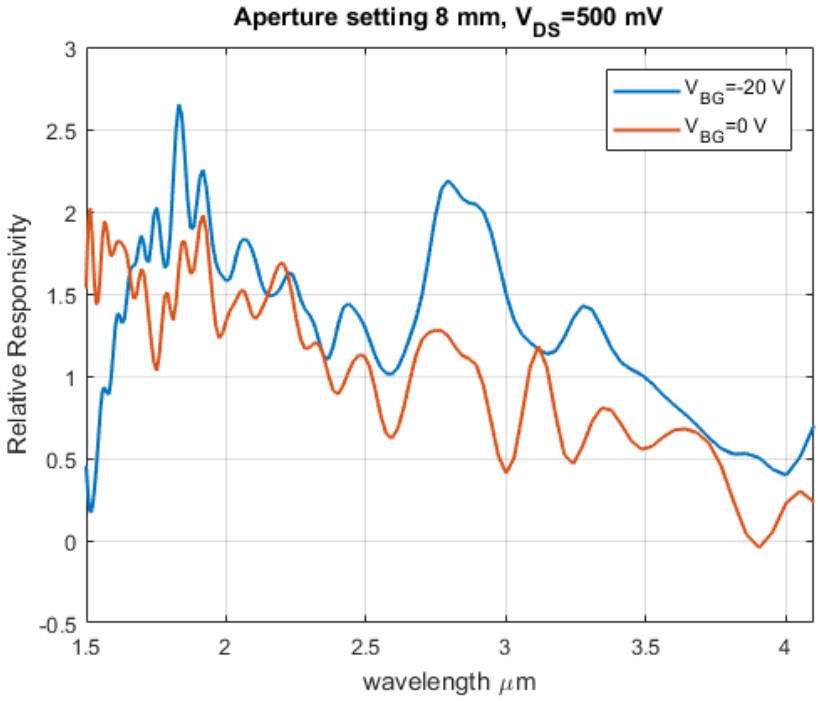

Figure 3.49 Relative Responsivity at different bottom gate voltages measured with FTIR NIR source (Device-6).

In conclusion, for this device we have observed and compared the output and transfer characteristics with the polymer electrolyte top gate and Si bottom gate. It showed high ON/OFF ratio due to the improved metal contact coming from longer annealing step after metallization. In addition to this, the uniform thickness of BP flake reduces the dislocation density or traps for the photogenerated carriers. High photoconductive gain is observed at low powers in the visible region because of higher responsivity values coming from large number of available carriers for photocurrent. However, there is small variation in the NIR responsivities with incident powers that indicate low gain in this region.

CHAPTER 4 CONCLUSIONS AND FUTURE WORK

4.1 Summary and thesis contributions

Dual-gate polymer electrolyte-based BP photodetectors that can be leveraged for integrated photonics and optoelectronics applications are presented. Towards this goal, a series of steps are implemented to accomplish the concept of dual gated BP devices with electrolyte gating approach. The following is the summary and contributions of this thesis:

- The two configurations of BP FET and photodetector structures were realized: the traditional Si bottom gate BP devices and the dual-gate polymer electrolyte-based BP devices. The complete experimental work on these devices is presented. This includes the microfabrication of alignment markers on Si wafers by photolithography, substrate treatments and exfoliation method to obtain high quality flakes, the metal contact fabrication process and finally the preparation and deposition of polymer electrolyte solution onto BP devices.
- BP flakes are characterized for flake distribution, quality, location, sizes, surface morphology and the microscopic analysis by optical microscopy, Atomic force microscopy and Polarization resolved Raman spectroscopy methods. The devices are then characterized electrically and optically to understand and explain the effect of bottom and top gating on photogenerated carriers and the responsivity of photodetectors.
- Broadband photodetection in BP with PEO:$CsClO_4$ solid polymer electrolyte as the top gate was demonstrated for the first time that is promising for integration with photonic circuits to achieve low operation voltages.

4.2 Conclusions

The theoretical understanding and the experimental results of single and dual-gate BP FET and photodetector devices based on polymer electrolyte gating can be deduced by following points:

- The dual-gate polymer electrolyte-based BP FET devices show the p-type conduction and current modulation in the BP channel with both Si bottom gate and electrolyte top gate. It also demonstrates the concept of EDLTs configuration by showing high carrier densities or

drain currents at low electrolyte gate voltages. The high drain currents in the semiconductor are attributed to the high capacitance formed at the gate-electrolyte and electrolyte-BP interfaces. The polymer electrolyte gated BP FET devices fabricated with orthogonal source-drain contacts also elucidate the anisotropic electrical transport in BP devices.

- We have also measured the source-drain voltage, gate-voltage and power dependent photocurrent and responsivities at NIR wavelengths. The photocurrent increases linearly with the source-drain voltage resulting from the high densities of photogenerated electrons and holes in addition to the gradual filling of the trap states in the BP channel. Higher photocurrents are observed at negative top/bottom gate voltages are that represents the ON state of the device and it decreases as it reaches the OFF state. Thus, electrolyte top gate and Si top gate modulation of carrier densities in the BP channel is observed in these devices in addition to the high ON/OFF ratio for top gate as compared to bottom gate.
- The effect of polymer electrolyte gating is also demonstrated over the entire visible and NIR regions by fabricating the dual-gate polymer electrolyte-based BP photodetectors (devices 5 and 6) that show significant gate voltage and power dependent photoresponse of these devices. The infrared photoresponse of the BP device is also studied for wavelengths above 1.7 μm using the NIR tungsten broadband internal source of FTIR. The tuning of relative responsivity amplitudes with the incident NIR powers and the gate voltages is also demonstrated. The increase in the infrared responsivities with negative gate voltages is shown to be attributed to the accumulation mode of the device which increases the number of electrons and holes inside the BP channel required to produce photocurrent.

4.3 Future Work

Exceptional research efforts are underway with the need to achieve high performance infrared photodetectors. BP based photodetectors allow for broadband photodetection in the infrared wavelengths owing all their outstanding properties discussed in the literature section. The polymer electrolyte based visible and NIR dual-gate BP photodetector developed in this thesis addressed some of the problems presented in the introduction by combining several ideas and methods. However, there is always a possibility of advancement and therefore few specific suggestions are made for extending this research work:

- Metal-contact engineering to increase the photo-generated carrier collection efficiencies in dual-gate BP phototransistors: An improvement in the BP photodetector design can involve studying combination of different work function metals in the dual gate phototransistor mode with polymer electrolyte or any high dielectric top gate insulator [67]. As explained in the theory, the low work function metals that have high SB heights are suitable for high current operation whereas high work function metals that provide low SB heights provide efficient photocarrier collection.
- Two dimensional colloidal nanocrystals integrated BP Phototransistors: Colloidal nanocrystals are the fascinating class of optical materials that have discrete optical energy spectra and are tunable over a wide range of infrared wavelengths [68]. Therefore, by combining strong absorbance properties and wavelength tunability properties of such nanostructures BP phototransistors with enhanced responsivity, detectivity and response time can be realized.
- Surface engineering for high performance BP phototransistors: The electronic/atomic structures and device performance of atomically thin layered BP semiconductors are modified with various surfaces [69]. The BP surface and metal-contact interface engineering can extremely alter the energy level alignment, orbital interactions and surface dipoles etc [70]–[72]. For example, the electronic properties can be effectively tuned by atom substitution, covalent and non-covalent functionalization. A voluminous understanding of the surface engineering of BP 2D layered semiconductors can tackle immense problems including the major problem of surface oxidation effects of thin BP flakes under ambient conditions [73].

REFERENCES

[1] J. Caniou, “Infrared detection,” in *Passive Infrared Detection*, Boston, MA: Springer US, 1999, pp. 1–26.

[2] A. Rogalski, *Infrared Detectors*. CRC Press, 2010.

[3] Y. Niu, B. Wang, J. Chen, and D. Wu, “Ultra-broadband and highly responsive photodetectors based on a novel EuBiTe 3 flake material at room temperaature,” *J. Mater. Chem. C*, vol. 6, no. 4, pp. 713–716, 2018.

[4] H. J. Song, M. H. Seo, K. W. Choi, M. S. Jo, J. Y. Yoo, and J. B. Yoon, “High-Performance Copper Oxide Visible-Light Photodetector via Grain-Structure Model,” *Sci. Rep.*, vol. 9, no. 1, Dec. 2019.

[5] M. A. Kinch, “Fundamental physics of infrared detector materials,” *J. Electron. Mater.*, vol. 29, no. 6, pp. 809–817, 2000.

[6] C. H. Liu, Y. C. Chang, T. B. Norris, and Z. Zhong, “Graphene photodetectors with ultra-broadband and high responsivity at room temperature,” *Nat. Nanotechnol.*, vol. 9, no. 4, pp. 273–278, 2014.

[7] T. J. Echtermeyer *et al.*, “Strong plasmonic enhancement of photovoltage in graphene,” *Nat. Commun.*, vol. 2, no. 1, 2011.

[8] O. Lopez-Sanchez, D. Lembke, M. Kayci, A. Radenovic, and A. Kis, “Ultrasensitive photodetectors based on monolayer MoS 2,” *Nat. Nanotechnol.*, vol. 8, no. 7, pp. 497–501, 2013.

[9] M. Long, P. Wang, H. Fang, and W. Hu, “Progress, Challenges, and Opportunities for 2D Material Based Photodetectors,” *Adv. Funct. Mater.*, vol. 29, no. 19, p. 1803807, May 2019.

[10] X. Chen *et al.*, “Widely tunable black phosphorus mid-infrared photodetector,” *Nat. Commun.*, vol. 8, no. 1, Dec. 2017.

[11] F. Wang *et al.*, “2D library beyond graphene and transition metal dichalcogenides: A focus on photodetection,” *Chemical Society Reviews*, vol. 47, no. 16. Royal Society of Chemistry, pp. 6296–6341, 21-Aug-2018.

[12] L. Li *et al.*, “Black phosphorus field-effect transistors,” *Nat. Nanotechnol.*, vol. 9, no. 5, pp. 372–377, 2014.

[13] B. Deng *et al.*, “Efficient electrical control of thin-film black phosphorus bandgap,” *Nat. Commun.*, vol. 8, Apr. 2017.

[14] J. Quereda *et al.*, “Strong Modulation of Optical Properties in Black Phosphorus through Strain-Engineered Rippling,” *Nano Lett.*, vol. 16, no. 5, pp. 2931–2937, May 2016.

[15] Z. J. Xiang *et al.*, “Pressure-Induced Electronic Transition in Black Phosphorus,” *Phys. Rev. Lett.*, vol. 115, no. 18, Oct. 2015.

[16] J. Yang *et al.*, “Optical tuning of exciton and trion emissions in monolayer phosphorene,” *Light Sci. Appl.*, vol. 4, no. 7, Jul. 2015.

[17] J. Kim *et al.*, “Observation of tunable band gap and anisotropic Dirac semimetal state in black phosphorus,” *Science (80-.).*, vol. 349, no. 6249, pp. 723–726, Aug. 2015.

[18] Y. Cai, G. Zhang, and Y. W. Zhang, “Layer-dependent band alignment and work function of few-layer phosphorene,” *Sci. Rep.*, vol. 4, Oct. 2014.

[19] R. Fei, A. Faghaninia, R. Soklaski, J.-A. Yan, C. Lo, and L. Yang, “Enhanced Thermoelectric Efficiency via Orthogonal Electrical and Thermal Conductances in Phosphorene,” *Nano Lett.*, vol. 14, no. 11, pp. 6393–6399, Nov. 2014.

[20] V. Tran, R. Soklaski, Y. Liang, and L. Yang, “Layer-controlled band gap and anisotropic excitons in few-layer black phosphorus,” *Phys. Rev. B*, vol. 89, no. 23, p. 235319, Jun. 2014.

[21] Z. Luo *et al.*, “Anisotropic in-plane thermal conductivity observed in few-layer black phosphorus,” *Nat. Commun.*, vol. 6, no. 1, p. 8572, Dec. 2015.

[22] H. Jang, J. D. Wood, C. R. Ryder, M. C. Hersam, and D. G. Cahill, “Anisotropic Thermal Conductivity of Exfoliated Black Phosphorus,” *Adv. Mater.*, vol. 27, no. 48, pp. 8017–8022, Dec. 2015.

[23] J.-W. Jiang and H. S. Park, “Negative poisson’s ratio in single-layer black phosphorus,” *Nat. Commun.*, vol. 5, no. 1, p. 4727, Dec. 2014.

[24] T. Hu, Y. Han, and J. Dong, “Mechanical and electronic properties of monolayer and bilayer phosphorene under uniaxial and isotropic strains,” *Nanotechnology*, vol. 25, no. 45, p.

455703, Nov. 2014.

[25] X. Yang, G. Liu, Y. Shi, W. Huang, J. Shao, and X. Dong, “Nano-black phosphorus for combined cancer phototherapy: recent advances and prospects,” *Nanotechnology*, vol. 29, no. 22, p. 222001, Jun. 2018.

[26] J. D. Wood *et al.*, “Effective passivation of exfoliated black phosphorus transistors against ambient degradation,” *Nano Lett.*, vol. 14, no. 12, pp. 6964–6970, Dec. 2014.

[27] J. Pei *et al.*, “Producing air-stable monolayers of phosphorene and their defect engineering,” *Nat. Commun.*, vol. 7, Jan. 2016.

[28] C. R. Ryder *et al.*, “Covalent functionalization and passivation of exfoliated black phosphorus via aryl diazonium chemistry,” *Nat. Chem.*, vol. 8, no. 6, pp. 597–602, Jun. 2016.

[29] K. F. Mak, M. Y. Sfeir, Y. Wu, C. H. Lui, J. A. Misewich, and T. F. Heinz, “Measurement of the opptical conductivity of graphene,” *Phys. Rev. Lett.*, vol. 101, no. 19, Nov. 2008.

[30] D. Kozawa *et al.*, “Photodetection in p-n junctions formed by electrolyte-gated transistors of two-dimensional crystals,” *Appl. Phys. Lett.*, vol. 109, no. 20, Nov. 2016.

[31] Y. Saito and Y. Iwasa, “Ambipolar Insulator-to-Metal Transition in Black Phosphorus by Ionic-Liquid Gating,” 2015.

[32] H. Xu, S. Fathipour, E. W. Kinder, A. C. Seabaugh, and S. K. Fullerton-Shirey, “Reconfigurable ion gating of 2H-MoTe<inf>2</inf> field-effect transistors using poly(ethylene oxide)-CsClO<inf>4</inf> solid polymer electrolyte,” *ACS Nano*, vol. 9, no. 5, pp. 4900–4910, May 2015.

[33] F. Bonaccorso, Z. Sun, T. Hasan, and A. C. Ferrari, “Graphene photonics and optoelectronics,” *Nat. Photonics*, vol. 4, no. 9, pp. 611–622, Sep. 2010.

[34] T. T. Tran, K. Bray, M. J. Ford, M. Toth, and I. Aharonovich, “Quantum emission from hexagonal boron nitride monolayers,” *Nat. Nanotechnol.*, vol. 11, no. 1, pp. 37–41, Jan. 2016.

[35] Y. M. Lin *et al.*, “100-GHz transistors from wafer-scale epitaxial graphene,” *Science*, vol. 327, no. 5966. p. 662, 05-Feb-2010.

[36] R. Murali, “Graphene transistors,” in *Graphene Nanoelectronics: From Materials to Circuits*, vol. 9781461405481, Springer US, 2012, pp. 51–91.

[37] T. T. Tran, K. Bray, M. J. Ford, M. Toth, and I. Aharonovich, “Quantum emission from hexagonal boron nitride monolayers,” *Nat. Nanotechnol.*, vol. 11, no. 1, pp. 37–41, Jan. 2016.

[38] C. R. Dean *et al.*, “Boron nitride substrates for high-quality graphene electronics,” *Nat. Nanotechnol.*, vol. 5, no. 10, pp. 722–726, Oct. 2010.

[39] N. Alem, R. Erni, C. Kisielowski, M. D. Rossell, W. Gannett, and A. Zettl, “Atomically thin hexagonal boron nitride probed by ultrahigh-resolution transmission electron microscopy,” *Phys. Rev. B*, vol. 80, no. 15, p. 155425, Oct. 2009.

[40] B. Radisavljevic, A. Radenovic, J. Brivio, V. Giacometti, and A. Kis, “Single-layer MoS2 transistors,” *Nat. Nanotechnol.*, vol. 6, no. 3, pp. 147–150, Mar. 2011.

[41] K. F. Mak, C. Lee, J. Hone, J. Shan, and T. F. Heinz, “Atomically Thin MoS_2 : A New Direct-Gap Semiconductor,” *Phys. Rev. Lett.*, vol. 105, no. 13, p. 136805, Sep. 2010.

[42] H. Fang, S. Chuang, T. C. Chang, K. Takei, T. Takahashi, and A. Javey, “High-Performance Single Layered WSe_2 p-FETs with Chemically Doped Contacts,” *Nano Lett.*, vol. 12, no. 7, pp. 3788–3792, Jul. 2012.

[43] M. Chhowalla, H. S. Shin, G. Eda, L.-J. Li, K. P. Loh, and H. Zhang, “The chemistry of two-dimensional layered transition metal dichalcogenide nanosheets,” *Nat. Chem.*, vol. 5, no. 4, pp. 263–275, Apr. 2013.

[44] C. Schneider, M. M. Glazov, T. Korn, S. Höfling, and B. Urbaszek, “Two-dimensional semiconductors in the regime of strong light-matter coupling,” *Nat. Commun.*, vol. 9, no. 1, p. 2695, Dec. 2018.

[45] A. Splendiani *et al.*, “Emerging Photoluminescence in Monolayer MoS_2,” *Nano Lett.*, vol. 10, no. 4, pp. 1271–1275, Apr. 2010.

[46] F. Xia, H. Wang, and Y. Jia, “Rediscovering black phosphorus as an anisotropic layered material for optoelectronics and electronics,” *Nat. Commun.*, vol. 5, p. 4458, Jul. 2014.

[47] G. Konstantatos, “Current status and technological prospect of photodetectors based on two-

dimensional materials," *Nature Communications*, vol. 9, no. 1. Nature Publishing Group, 01-Dec-2018.

[48] L. Britnell *et al.*, "Strong Light-Matter Interactions in Heterostructures of Atomically Thin Films," *Science (80-.).*, vol. 340, no. 6138, pp. 1311–1314, Jun. 2013.

[49] K. Roy *et al.*, "Graphene–MoS2 hybrid structures for multifunctional photoresponsive memory devices," *Nat. Nanotechnol.*, vol. 8, no. 11, pp. 826–830, Nov. 2013.

[50] M. Long *et al.*, "Broadband Photovoltaic Detectors Based on an Atomically Thin Heterostructure," *Nano Lett.*, vol. 16, no. 4, pp. 2254–2259, Apr. 2016.

[51] Q. Guo *et al.*, "Black Phosphorus Mid-Infrared Photodetectors with High Gain," *Nano Lett.*, vol. 16, no. 7, pp. 4648–4655, Jul. 2016.

[52] X. Chen *et al.*, "Widely tunable black phosphorus mid-infrared photodetector," *Nat. Commun.*, vol. 8, no. 1, p. 1672, Dec. 2017.

[53] M. Long *et al.*, "Room temperature high-detectivity mid-infrared photodetectors based on black arsenic phosphorus," *Sci. Adv.*, vol. 3, no. 6, p. e1700589, Jun. 2017.

[54] W. C. Tan *et al.*, "A Black Phosphorus Carbide Infrared Phototransistor," *Adv. Mater.*, vol. 30, no. 6, p. 1705039, Feb. 2018.

[55] M. Amani, E. Regan, J. Bullock, G. H. Ahn, and A. Javey, "Mid-Wave Infrared Photoconductors Based on Black Phosphorus-Arsenic Alloys," *ACS Nano*, vol. 11, no. 11, pp. 11724–11731, Nov. 2017.

[56] M. Buscema, D. J. Groenendijk, S. I. Blanter, G. A. Steele, H. S. J. van der Zant, and A. Castellanos-Gomez, "Fast and Broadband Photoresponse of Few-Layer Black Phosphorus Field-Effect Transistors," *Nano Lett.*, vol. 14, no. 6, pp. 3347–3352, Jun. 2014.

[57] J. Wu *et al.*, "Colossal Ultraviolet Photoresponsivity of Few-Layer Black Phosphorus," *ACS Nano*, vol. 9, no. 8, pp. 8070–8077, Aug. 2015.

[58] T. Hong, B. Chamlagain, T. Wang, H.-J. Chuang, Z. Zhou, and Y.-Q. Xu, "Anisotropic photocurrent response at black phosphorus–MoS_2 p–n heterojunctions," *Nanoscale*, vol. 7, no. 44, pp. 18537–18541, Nov. 2015.

[59] N. Youngblood, C. Chen, S. J. Koester, and M. Li, "Waveguide-integrated black phosphorus

photodetector with high responsivity and low dark current," *Nat. Photonics*, vol. 9, no. 4, pp. 247–252, Apr. 2015.

[60] Q. Guo *et al.*, "Black Phosphorus Mid-Infrared Photodetectors with High Gain," *Nano Lett.*, vol. 16, no. 7, pp. 4648–4655, Jul. 2016.

[61] S. H. Kim *et al.*, "Electrolyte-gated transistors for organic and printed electronics," *Advanced Materials*, vol. 25, no. 13. pp. 1822–1846, 04-Apr-2013.

[62] C. Liu *et al.*, "Top-gated black phosphorus phototransistor for sensitive broadband detection," *Nanoscale*, vol. 10, no. 13, pp. 5852–5858, Apr. 2018.

[63] M. W. Lin *et al.*, "Mobility enhancement and highly efficient gating of monolayer MoS 2 transistors with polymer electrolyte," *J. Phys. D. Appl. Phys.*, vol. 45, no. 34, Aug. 2012.

[64] P. C. Y. Chow, N. Matsuhisa, P. Zalar, M. Koizumi, T. Yokota, and T. Someya, "Dual-gate organic phototransistor with high-gain and linear photoresponse," *Nat. Commun.*, vol. 9, no. 1, Dec. 2018.

[65] X. Liu *et al.*, "Modulation of Quantum Tunneling via a Vertical Two-Dimensional Black Phosphorus and Molybdenum Disulfide p-n Junction," *ACS Nano*, vol. 11, no. 9, pp. 9143–9150, Sep. 2017.

[66] Y. Deng, N. J. Conrad, Z. Luo, H. Liu, X. Xu, and P. D. Ye, "Towards high-performance two-dimensional black phosphorus optoelectronic devices: The role of metal contacts," in *Technical Digest - International Electron Devices Meeting, IEDM*, 2015, vol. 2015-February, no. February, pp. 5.2.1-5.2.4.

[67] Y. Wang *et al.*, "Van der Waals contacts between three-dimensional metals and two-dimensional semiconductors," *Nature*, vol. 568, no. 7750. Nature Publishing Group, pp. 70–74, 04-Apr-2019.

[68] Z. Liu and R. Beaulac, "Nature of the Infrared Transition of Colloidal Indium Nitride Nanocrystals: Nonparabolicity Effects on the Plasmonic Behavior of Doped Semiconductor Nanomaterials," *Chem. Mater.*, vol. 29, no. 17, pp. 7507–7514, Sep. 2017.

[69] T. Niu, J. Zhang, and W. Chen, "Surface Engineering of Two-Dimensional Materials," *ChemNanoMat*, vol. 5, no. 1, pp. 6–23, Jan. 2019.

[70] M. L. Perrin *et al.*, “Large tunable image-charge effects in single-molecule junctions,” *Nat. Nanotechnol.*, vol. 8, no. 4, pp. 282–287, 2013.

[71] G. Heimel *et al.*, “Charged and metallic molecular monolayers through surface-induced aromatic stabilization,” *Nat. Chem.*, vol. 5, no. 3, pp. 187–194, Mar. 2013.

[72] H. Y. Mao *et al.*, “Mechanism of the Fermi level pinning at organic donor-acceptor heterojunction interfaces,” *Org. Electron. physics, Mater. Appl.*, vol. 12, no. 3, pp. 534–540, Mar. 2011.

[73] J. O. Island, G. A. Steele, H. S. J. Van Der Zant, and A. Castellanos-Gomez, “Environmental instability of few-layer black phosphorus,” *2D Mater.*, vol. 2, no. 1, Jan. 2015.

APPENDIX A EXPERIMENTAL SETUP FOR RESPONSIVITY MEASUREMENTS[1]

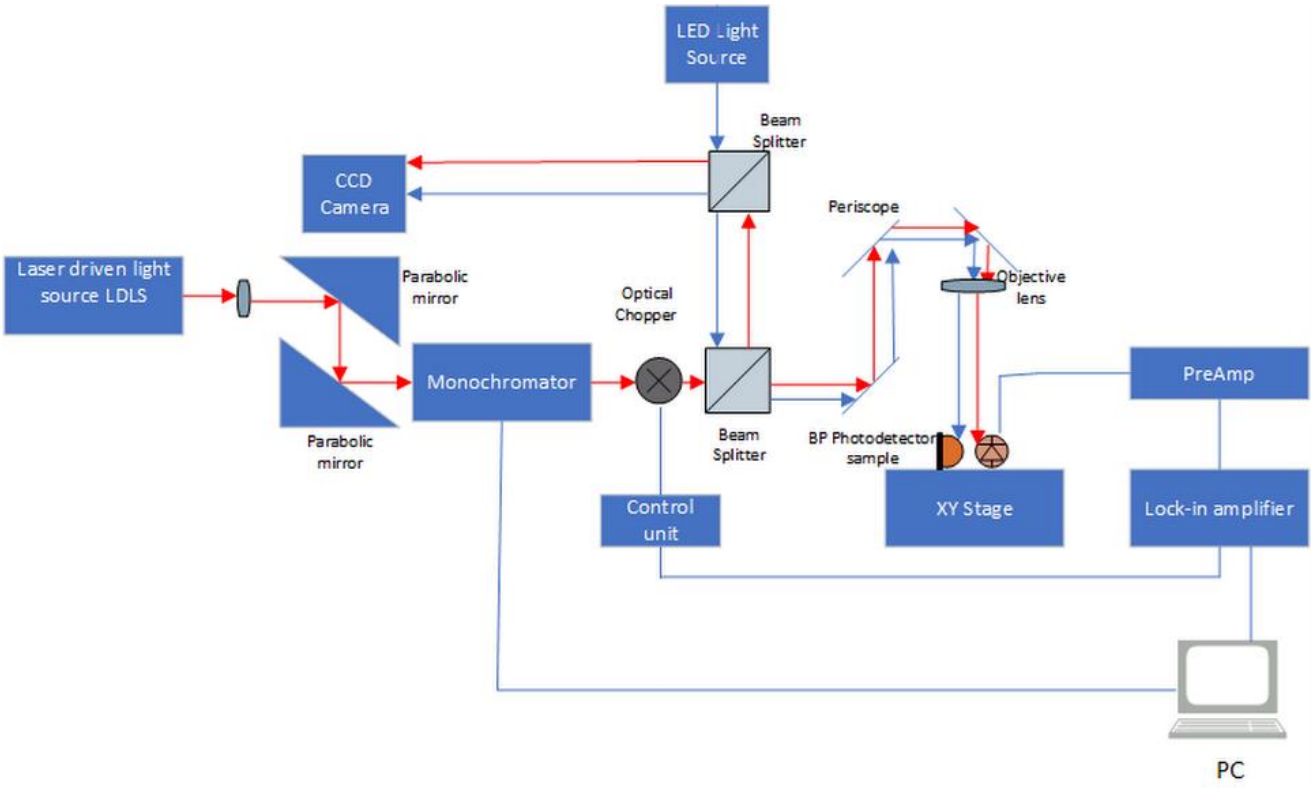

[1] The setup with Fianium Supercontinuum source is without parabolic mirrors.

APPENDIX B AFM MEASUREMENTS[2]

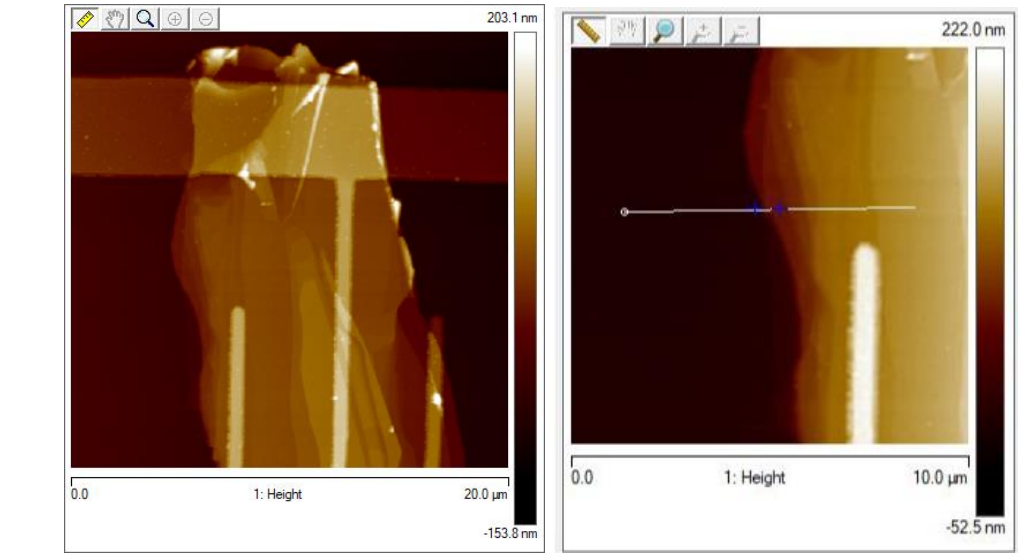

(a)

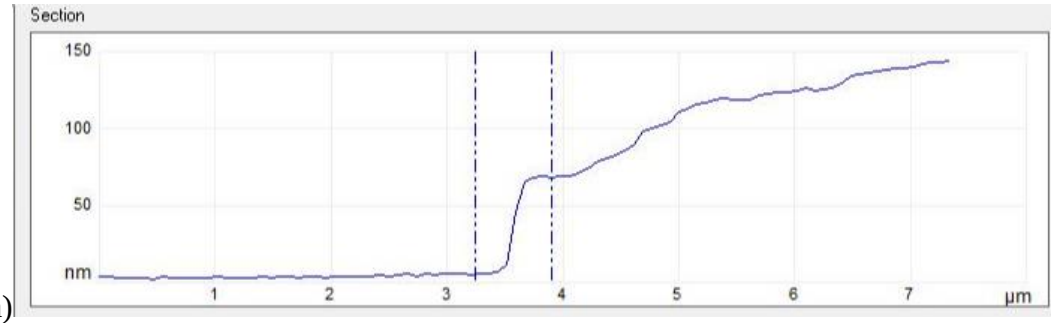

(b)

Figure: (a) AFM images of Device 5 (b) Section showing the thickness measurement (Device-5)

[2] AFM D3100 Nanoscope.

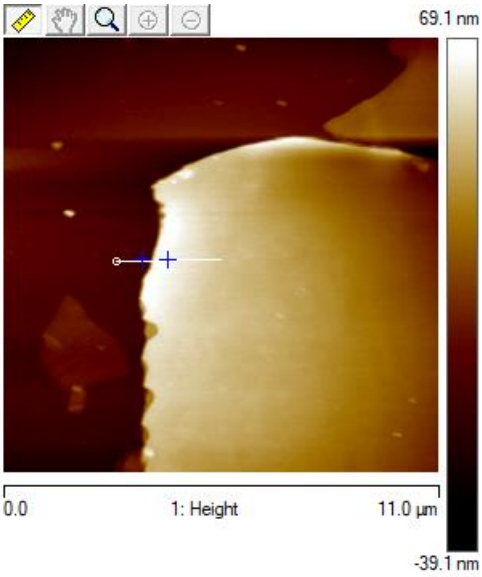

(a)

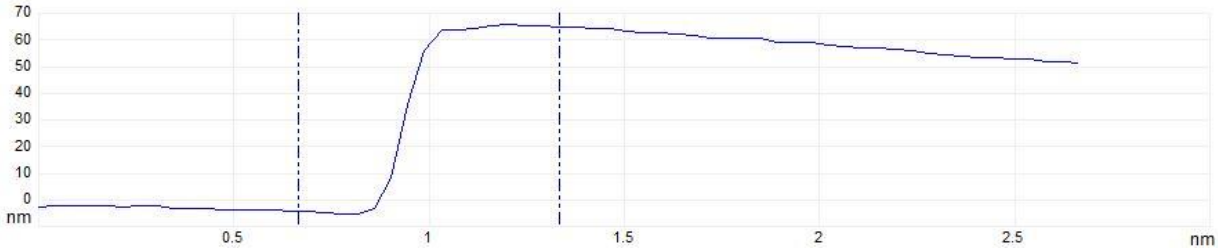

(b)

Figure: (a) AFM images of Device 6, (b) Section showing the thickness measurement.

APPENDIX C SI PHOTODIODE RESPONSIVITY DATA

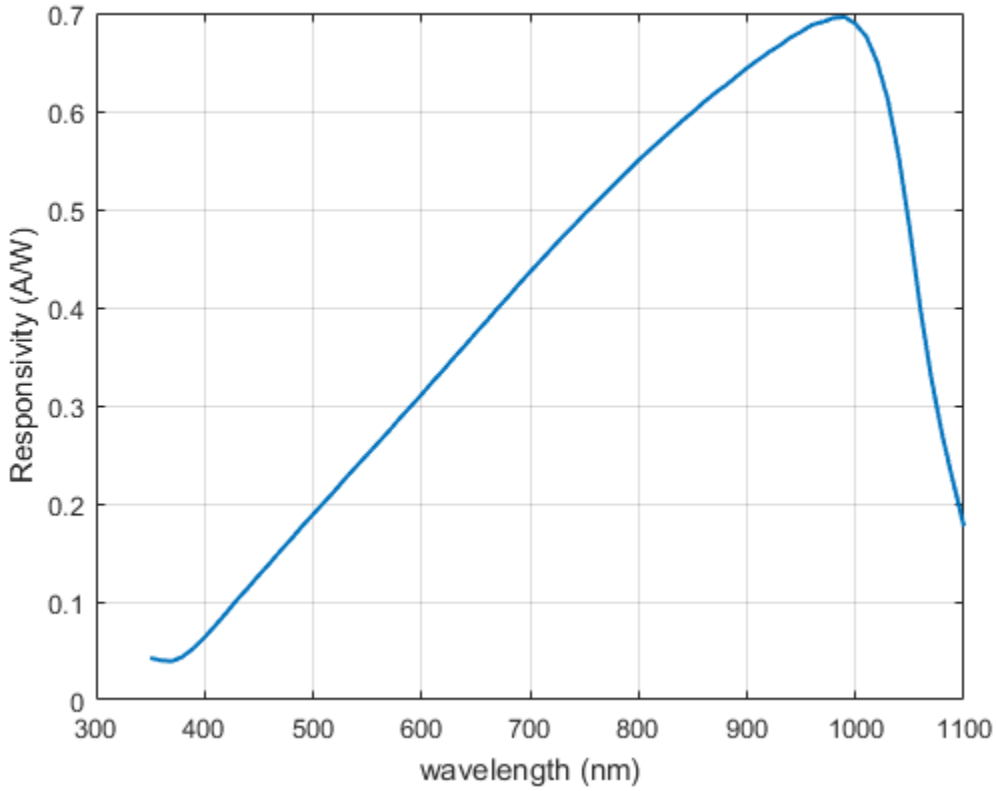

Responsivity data of Si Photodiode[3].

Wavelength (nm)	Responsivity (A/W)
350	0.03
360	0.028
370	0.028
380	0.034
390	0.043
400	0.052
410	0.066
420	0.079
430	0.092
440	0.106
450	0.12

[3] Model: FDS1010, Company: Thorlabs.

460	0.132
470	0.145
480	0.159
490	0.173
500	0.186
510	0.2
520	0.214
530	0.229
540	0.243
550	0.256
560	0.269
570	0.282
580	0.295
590	0.309
600	0.323
610	0.336
620	0.35
630	0.367
640	0.381
650	0.393
660	0.406
670	0.42
680	0.433
690	0.446
700	0.459
710	0.473
720	0.488
730	0.5
740	0.511
750	0.522
760	0.533
770	0.545
780	0.557
790	0.568
800	0.579

APPENDIX D INGAAS PHOTODIODE RESPONSIVITY DATA

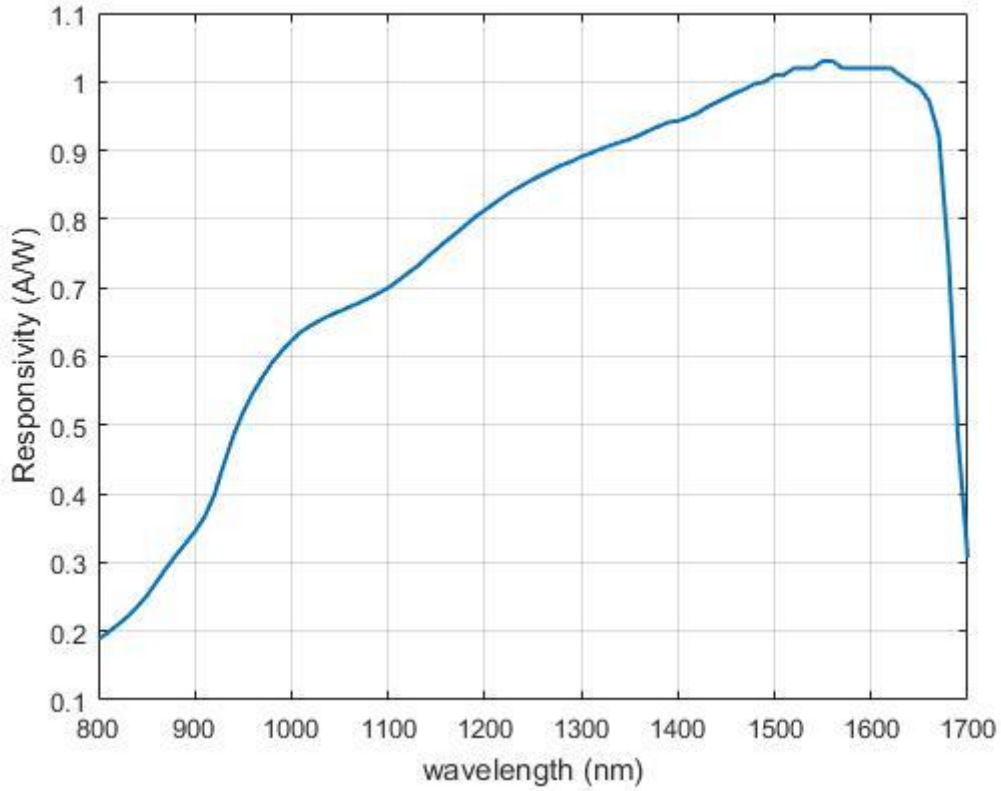

Responsivity data of InGaAs Photodiode[4].

Wavelength (nm)	Responsivity (A/W)
800	0.1727
810	0.18137
820	0.18972
830	0.19853
840	0.20768
850	0.21981
860	0.23884
870	0.25847
880	0.27322
890	0.29149
900	0.30945

[4] Model: FGA21, Company: Thorlabs.

910	0.32721
920	0.3535
930	0.39916
940	0.43724
950	0.45151
960	0.45663
970	0.46784
980	0.47834
990	0.50146
1000	0.49725
1010	0.52327
1020	0.53522
1030	0.54625
1040	0.55642
1050	0.57017
1060	0.58709
1070	0.61555
1080	0.62418
1090	0.63832
1100	0.65226
1110	0.66846
1120	0.6842
1130	0.70083
1140	0.70711
1150	0.70609
1160	0.72417
1170	0.72529
1180	0.74299
1190	0.75209
1200	0.76023
1210	0.76731
1220	0.77651
1230	0.7833
1240	0.78959
1250	0.79862
1260	0.80424
1270	0.81308
1280	0.82207
1290	0.83071
1300	0.84047
1310	0.85035
1320	0.86084
1330	0.87075
1340	0.88025
1350	0.88061

1360	0.86495
1370	0.89845
1380	0.8886
1390	0.91994
1400	0.93
1410	0.96205
1420	0.96668
1430	0.97485
1440	0.9824
1450	0.98423
1460	0.97483
1470	0.99722
1480	1.00621
1490	1.01353
1500	1.01834
1510	1.02433
1520	1.02708
1530	1.02921
1540	1.03119
1550	1.03425
1560	1.03622
1570	1.03768
1580	1.03869
1590	1.03923
1600	1.0364
1610	1.02832
1620	1.01909
1630	1.01325
1640	0.99506
1650	0.97854
1660	0.94656
1670	0.85302
1680	0.63355
1690	0.40393
1700	0.25739
1710	0.1754
1720	0.1315
1730	0.08848
1740	0.0642
1750	0.047
1760	0.03584
1770	0.02848
1780	0.02381
1790	0.02135
1800	0.02083

APPENDIX E FTIR COMPONENTS AND BEAM PATH[5]

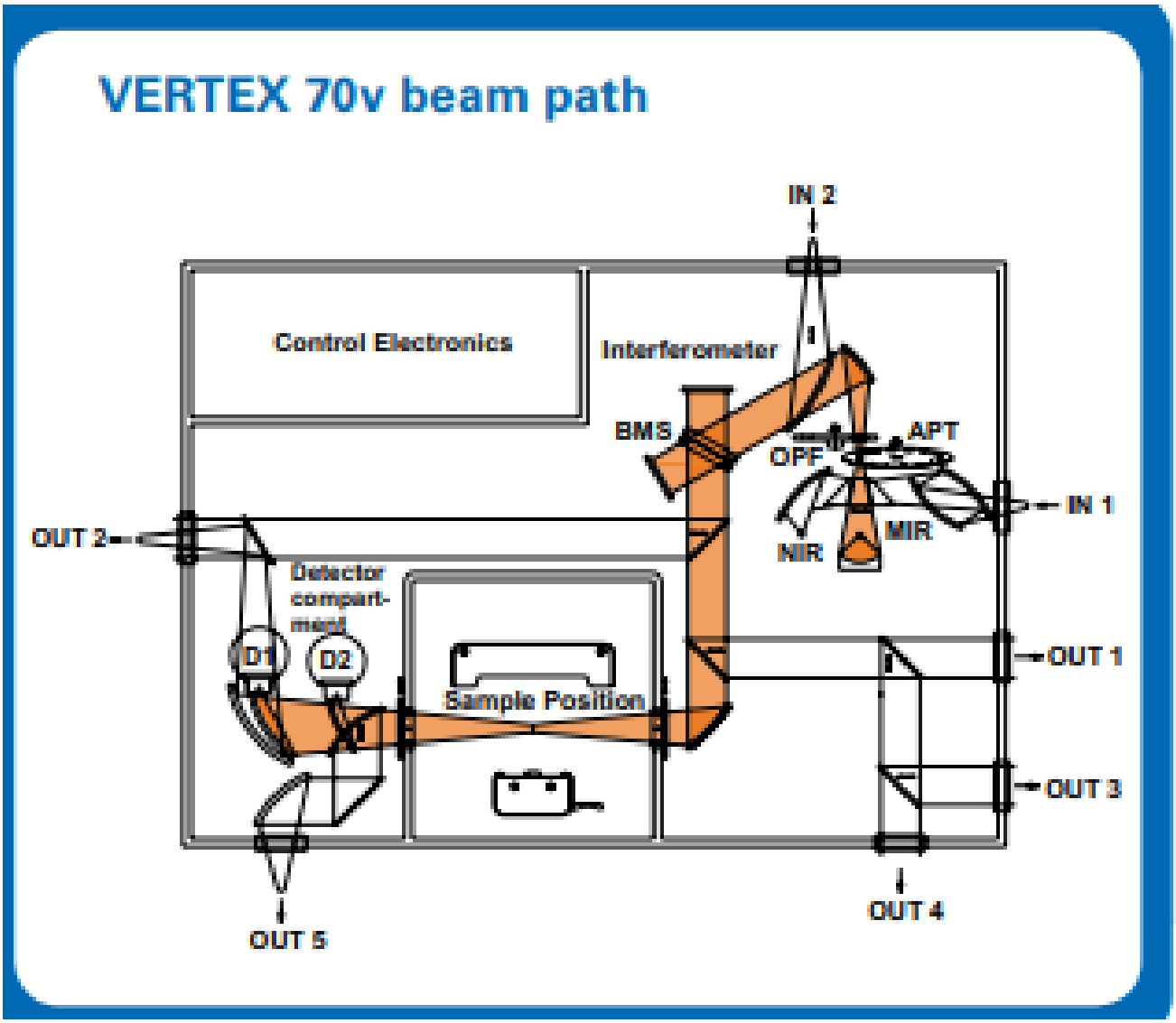

[5] Model: VERTEX 70V FTIR Spectrometer, Company: Bruker.

APPENDIX F POWER PROFILE OF FTIR NIR AND MIR LIGHT SOURCES MEASURED WITH DLATGS DETECTOR AT DIFFERENT APERTURE SETTINGS.[6]

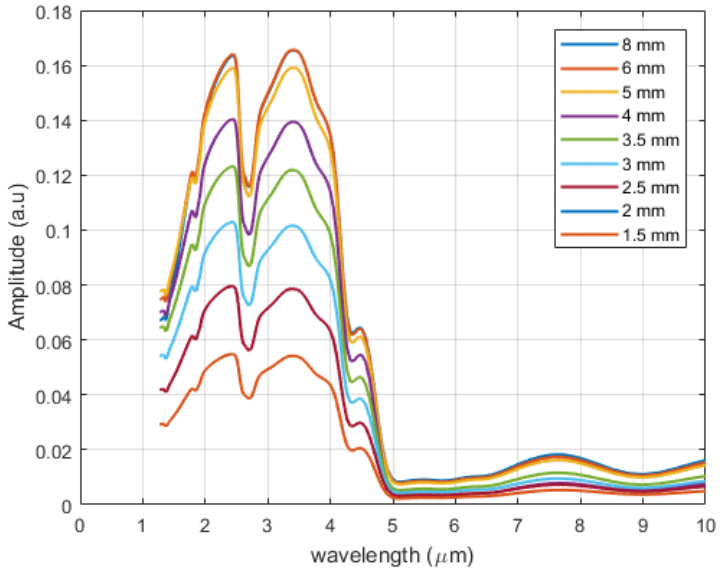

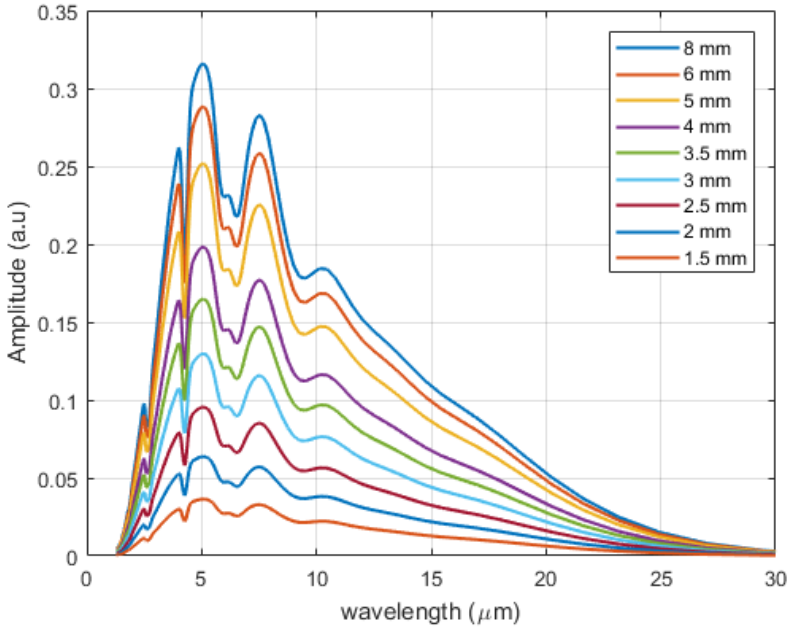

[6] Model: VERTEX 70V FTIR Spectrometer, Company: Bruker.

APPENDIX G PHOTORESPONSE OF INGAAS DETECTOR USING FTIR WITH NIR LIGHT SOURCE AT DIFFERENT APERTURES/POWER LEVELS.[7]

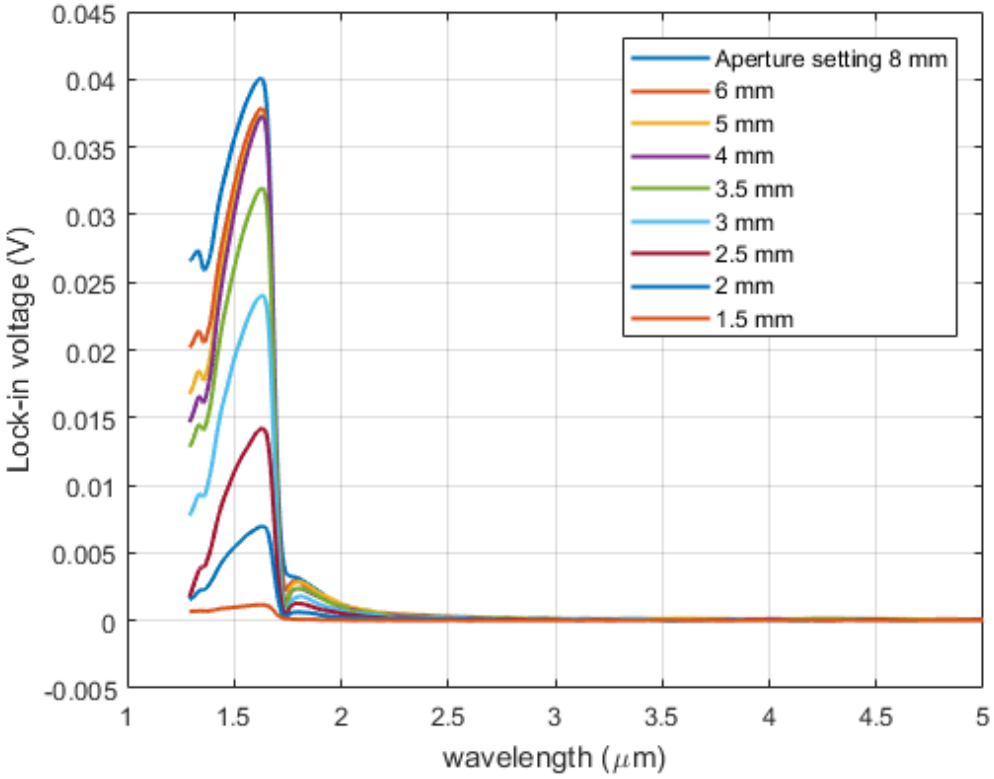

[7] Model: FGA21, Company: Thorlabs.